Modeling of Cutting Forces for 5-axis Ball-end Milling of Free-form Surfaces

by

Yaman Boz

A Thesis Submitted to the
Graduate School of Engineering
in Partial Fulfillment of the Requirements for
the Degree of

Master of Science

in

Mechanical Engineering

Koc University

September 2010

Koc University

Graduate School of Sciences and Engineering

This is to certify that I have examined this copy of a master's thesis by

Yaman Boz

and have found that it is complete and satisfactory in all respects,
and that any and all revisions required by the final
examining committee have been made.

Committee Members:

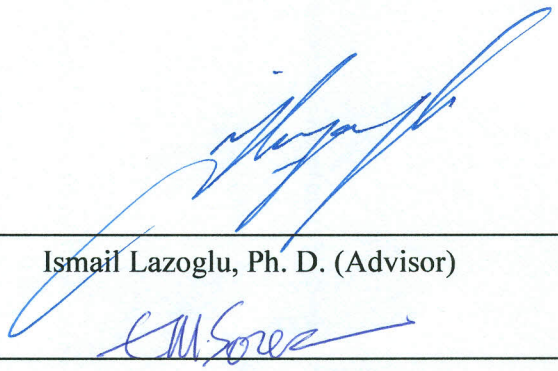

Ismail Lazoglu, Ph. D. (Advisor)

Murat Sözer, Ph.D.

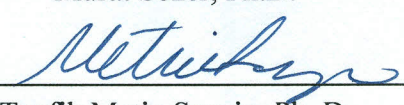

Tevfik Metin Sezgin, Ph. D.

Date: 23.9.2010

ABSTRACT

5-axis milling processes are used widely in various industries such as aerospace, die-mold and biomedical industries where surface quality and integrity is important and the production tolerances are very tight. Therefore, improving surface quality and integrity without sacrificing productivity is crucial in these industries. Improvements in CAD/CAM, cutting tool and the machine tool technologies allow the production of high precision parts with less cycle times. In order to obtain desired quality and productivity, process parameters such as feedrate, spindle speed, axial and radial depth of cut have to be selected appropriately. In general, these parameters are selected conservatively, most of the time arbitrarily, in order to prevent workpiece, cutter or the machine to be damaged. Consequently, this selection criterion is based on engineering expertise or trial and error methods. Therefore virtual machining simulation for milling processes is an increasing demand before the production of the free-form surfaces.

In this thesis, virtual machining simulation model for the simulation of cutting forces in 5-axis ball-end milling of free-form surfaces is presented.

5-axis milling kinematics differs from the 3-axis milling. For this reason, modeling of 5-axis machine tool kinematics is introduced and a generic post-processor with variable feedrate is developed. A virtual machine simulation model, which is capable of simulating machine tool movements from the NC code, is also presented.

Cutting forces in machining is determined by extracting the Cutter-Workpiece Engagement (CWE) from the in-process workpiece. A discrete method (Three-Orthogonal Dexelfield) of obtaining CWE maps for 5-axis ball-end milling is developed. The results of the Three-Orthogonal Dexelfield method is compared with the solid-modeler based CWE calculation method.

A cutting force prediction model for 5-axis ball-end milling is developed. Cutting force modeling is performed in the fixed coordinate frame (for table type dynamometer) and in

the rotating coordinate frame (rotating coordinate dynamometer). A modular approach is developed where different cutter and workpiece geometries and tool motions can be incorporated into the model without additional analysis. Several validation tests are presented in the study and these validation tests demonstrate that presented cutter-workpiece engagement model is accurate and force predictions are in good agreement with the measured data.

ÖZET

5-eksen frezeleme süreçleri, yüzey kalitesinin ve bütünlüğünün önemli olduğu ve üretim toleranslarının çok dar olduğu uçak-uzay, kalıp ve biyomedikal endüstrilerinde yaygın olarak kullanılmaktadır. Bu endüstrilerde üretkenliği düşürmeden yüzey kalitesi ve bütünlüğünün iyileştirilmesi büyük önem arz etmektedir.

CAD (bilgisayar destekli tasarım)/CAM (bilgisayar destekli imalat), kesici takım ve takım tezgahı teknolojilerindeki gelişmeler yüksek hassasiyete sahip parçaların daha kısa sürede üretilmesine olanak sağlamıştır. İstenilen kalitenin ve üretkenliğin sağlanabilmesi için ilerleme hızı, iş mili devri, eksenel ve radyal dalma derinlikleri doğru bir şekilde seçilmelidir. Bu parametreler iş parçasının, takımın ya da takım tezgahının zarar görmesini engellemek amacıyla çoğu zaman rastgele ya da konservatif olarak seçilmektedir. Sonuç olarak, bu seçim kriteri mühendislik tecrübesine ya da deneme-yanılmaya dayanmaktadır. Bu bakımdan, parça üretilmeden önce frezeleme süreçlerinin sanal talaşlı imalat simülasyonu giderek artan bir talep halini almıştır.

Bu tezde, serbest yüzey geometrilerine sahip parçaların 5-eksen küresel frezeleme süreçleri için sanal talaşlı imalat simülasyon modeli sunulmuştur.

5-eksen frezeleme kinematiği 3-eksen frezeleme kinematiğinden farklılıklar göstermektedir. Bundan dolayı, 5-eksen takım tezgahlarının kinematik modellenmesi yapılmış ve değişken ilerleme hızlarını destekleyen genelgeçer bir son-işlemci (post-processor) geliştirilmiştir. Ayrıca, NC (nümerik kontrol) kodlarından takım tezgahının hareketlerini simüle edebilen bir sanal makine simülasyonu modeli sunulmuştur.

Talaşlı imalatta kesme kuvvetleri tahmini iş parçası ile takımın temas bölgesini belirleyerek yapılmaktadır. Bu bilgi, işlenmiş parçadan takım ekseni boyunca ayrık diskler için giriş ve çıkış açıları şeklinde ifade edilmektedir. 5-eksen küresel frezeleme için takım-iş parçası temasını bulabilmek için ayrık modellemeye dayalı bir takım-iş parçası temas

modeli (Three-Orthogonal Dexelfield) geliştirlmiştir. Bu modelin sonuçları katı model tabanlı takım-iş parçası teması modeli ile karşılaştırılmıştır.

5-eksen küresel frezeleme süreçlerinde kuvvet tahmini yapabilen bir model ortaya konulmuştur. Kesme kuvveti modellemesi sabit eksen takımı (tabla tipi dinamometre) ve döner eksen takımı (döner eksenli dinamometre) için yapılmıştır. Ortaya konulan bu model modüler olup farklı iş parçası geometrileri, takım hareketleri ekstra bir analize gerek kalmadan bu modele dahil edilebilmektedir. Bu çalışmada bir çok gerçekleme testi sunulmuş olup, gerçekleme testleri göstermiştir ki ortaya konulan model hesaplama açısından verimlidir ve kuvvet tahminleri deneysel verilerle iyi bir uyum sergilemektedir.

ACKNOWLEDGEMENTS

I would like to express my gratitude to my advisor, Dr. Ismail Lazoglu for his guidance and I also would like to thank Dr. Murat Sözer and Dr. Tevfik Metin Sezgin for reading this thesis and involving in my thesis committee.

Behalf of Manufacturing and Automation Research Center (MARC) I would like to acknowledge the Machine Tool Technologies Research Foundation (MTTRF), the Mori Seiki Co., and the DP Technology Corp for the Mori Seiki NMV 5000DCG CNC Machining Center and Esprit CAM software for supports. I acknowledge Sandvik Coromant Company for providing cutting tools for this research.

I acknowledge ModuleWorks GmbH and Yavuz Murtezaoğlu for providing us the NC verification kernel from ModuleWorks and I also acknowledge Jan Manuel Theegarten for his support on the implementation of the provided verification kernel

I deeply appreciate Huseyin Erdim not only for his previous studies on 3-axis Ball-end milling that provided me fundamental knowledge on ball-end milling mechanics but also for his effort and sacrifice for the development of the Solid-modeler based Cutter-Workpiece Engagement model for 5-axis Ball-end milling. I also would like to thank him for his valuable discussions on the subject of my thesis and 5-axis machining.

I want to thank to my family; my father Selçuk Boz, my mother Gül Boz and my brother Yiğit Boz from the bottom of my heart for their everlasting belief and support for my success throughout my entire education. And I am also grateful to my parents who taught me how to deal with a life with difficulties at all costs.

Finally, I would like thank my girlfriend Başak Bağcıoğlu for being the joy of my life during my Master's study with her never ending love, support and understanding.

TABLE OF CONTENTS

LIST OF TABLES

LIST OF FIGURES

NOMENCLATURE

$X_T - Y_T - Z_T$	tooltip coordinate frame
$X_R - Y_R - Z_R$	rotary zero coordinate frame
$X_W - Y_W - Z_W$	workpiece coordinate frame
θ_z	rotation angle of C axis
θ_y	rotation angle of B axis
B	rotation angle of B axis
C	rotation angle of C axis
P_x, P_y, P_z	x, y, z position of the tooltip in the CL file
T_x, T_y, T_z	tool axis orientation in i, j, k direction in the CL file
$\vec{W}$	offset distance from the workpiece coordinate frame to the rotary zero coordinate frame
$\vec{D}$	translation in workpiece coordiante frame
X, Y, Z	tooltip coordinates in the NC file
$\overrightarrow{CV}$	cut vector in the tooltip origin
$\overrightarrow{CP}$	cut point in workpiece coordinate frame
$\vec{P_i}$	coordinates of the ith CL point in the toolpath
$\vec{m}$	tool movement vector
$\vec{k_i}$	rotation axis of the tool for the ith CL point
$\Delta\varphi$	rotation angle of the tool for the ith CL point
$\vec{X}_f, \vec{Y}_f, \vec{Z}_f$	x, y, z axis of the feed coordinate frame
$\vec{n}$	tool surface normal
$\overrightarrow{TCP}$	tool center point
R	tool radius
$\overrightarrow{CV_p}$	projection of cut vector on tool axis
$\overrightarrow{CV_{xy}}$	projection of cut vector on the $X_f - Y_f$ plane

$\overrightarrow{CV_x}$	projection of cut vector on the feed vector
$\overrightarrow{CV_y}$	projection of cut vector on the cross-feed vector
θ_e	engagement angle
x, y, z	coordinates of cutting edge of ball-end mill
R_b	ball radius of the cutter
r	tool radius in x-y plane at a point defined by ψ
β	lag angle between the tangent line at the tip of the flute and axial location z
x_c, y_c, z_c	coordinates of cutting edge of ball-end mill according to rotating frame
θ_{st}	engagement start angle of each discrete disc
θ_{ex}	engagement exit angle of each discrete disc
α	feed inclination angle
t_c	instantaneous chip load
t_x	feed per tooth
θ	immersion angle of cutting point
ψ	cutting element position angle
$(t_c)_k$	instantaneous undeformed chip thickness for ball-end mill cutter
dA_c	differential chip load
F_r, F_ψ, F_t	cutting forces in tangential, radial and axial directions
dF_x, dF_y, dF_z	differential cutting forces in x, y, and z directions
$K_{rc}, K_{\psi c}, K_{tc}$	tangential, radial and axial cutting force coefficients in milling
$K_{re}, K_{\psi e}, K_{te}$	tangential, radial and axial edge force coefficients in milling
γ	feed direction angle
Ω	rotation angle of flute
N_f	number of flutes
n	flute number
β_k	lag angle between the k^{th} discrete point on cutting edge and the cutter tip
ω	spindle speed in revolution per minute
f	feedrate of the cutter in mm per minute

$d\theta$	Integration angle
dz	Integration height
$\Delta\theta$	discrete cutting element rotation angle
f_s	data sampling frequency
z_1	measured upper boundary distance from the tip of the sphere part
z_2	measured lower boundary distance from the tip of the sphere part
D	diameter of the cutter in mm
$X_D - Y_D - Z_D$	the rotating dynamometer coordinate frame
Ω_R	reference rotation angle
Ω_a	misalignment angle

Chapter 1

INTRODUCTION

5-axis machining has been used in aerospace applications for many years. Recently, automotive, die-mold, toolmaking and biomedical industries have shown similar interest. Parts manufactured with 5-axis machine tools constitute main components of the high-level systems which can be manufactured using today's technology.

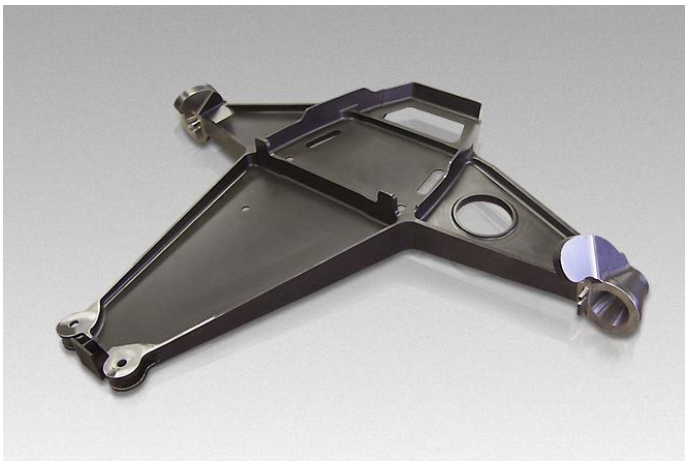

Figure 1.1: A typical aircraft part.[1]

Aircraft parts typically have walls that are not perpendicular to the floor of the part. Cutting these walls with 3-axis machining requires multiple-pass milling operations using cylindrical end mills or special form tools. 5-axis machining, eliminates the use of multiple setups since tool can tilt and lead yielding one pass cut using a standard end mill. A typical example of the aircraft part is given in Figure 1.1.

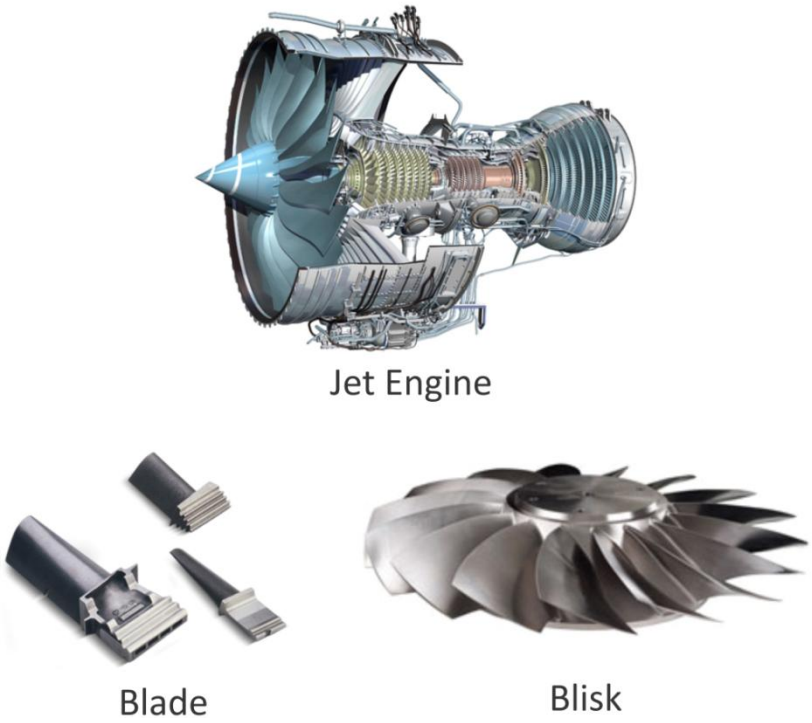

Figure 1.2: Jet engine [2], Blisk [3] and Blades [4]

Blisks and Integrally Bladed Rotors (IBR) are used in jet-powered aircraft engines and in high pressure compressors for military purposes (Figure 1.2). Blades can be produced with 3-axis machining however this requires multiple setups and the use of longer tools. Blisks and IBRs can also be manufactured on profilers by tracing templates to control the X and Y axis of the machine and following cams to control the Z axis. Furthermore, the fixtures have to be manually rotated prior to cutting of each blade. Hence, each blade differs in shape due to manual alignment of the fixtures.

Similarly, impellers (Figure 1.3) used in compressors and turbines have very complex shapes and demands the use of 5-axis machining for reducing machining times and improving part quality and uniformity.

Figure 1.3: Compressor Impeller [3]

More recently, biomedical industry have started using 5-axis machining technology for knee joint implants, dental implants, heart pumps and spine implants (Figure 1.4).

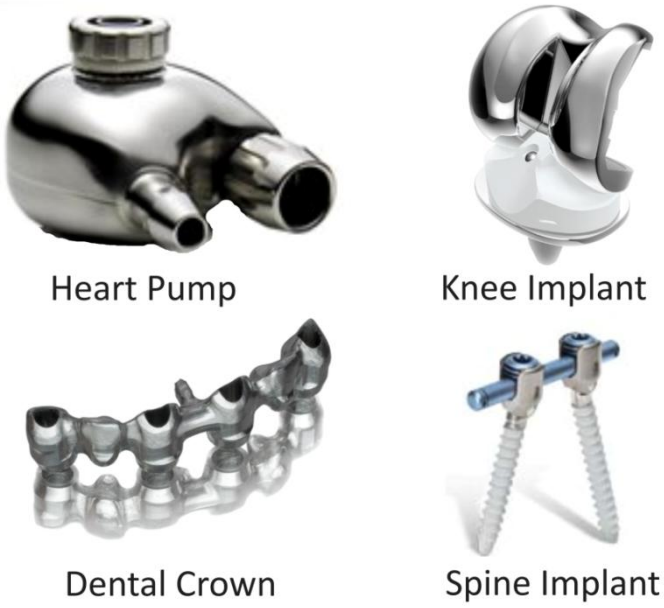

Figure 1.4: Medical implants [5-8]

Generally, medical implants have free-form surfaces with arbitrary shapes demanding 5-axis machining. Knee implants and dental crowns can be manufactured in multiple setups.

In these industries different workpiece materials are used in order to provide desired mechanical or other properties. Impellers, blades and blisks are commonly produced from Titanium alloys (e.g. $Ti6Al4V$) and Inconel. For the purpose of jet engine parts Titanium alloys and Inconel is preferred due to their strength at high temperatures and low thermal conductivity. Aluminum alloys (e.g. 7000 series) are preferred for moderate working environments such as transport applications, including marine, automotive and aviation applications, due to their high strength-to-density ratio. Biomedical applications require several properties which are high wear resistance, toughness, ductility and biocompatibility. For this reason, biocompatible Titanium alloys (e.g. $Ti6Al4Veli$) or Stainless Steels (e.g. $AISI\ 316LVM$) are used.

From machining perspective, these materials are hard to machine materials. In other words, machinability of these materials is very poor except Aluminum alloys. Machinability of Aluminum alloys is better than Stainless Steels and Titanium alloys however they still exhibit average machinability.

In roughing operations, typically axial depth of cuts and radial depth of cuts are high in order to maximize the material removal volume. Hence, cutting forces in roughing operations are usually high which may cause excessive tool deflection or even tool breakage. For finishing operations, low depth of cuts and high feedrates are selected. Cutting forces in finishing operations are relatively small on the other hand tool deflections induced by cutting forces may deteriorate the precision of the process.

With 5-axis machining, complex shapes can be machined in a single setup which reduces cycle times. Improved tool accessibility allows the use of shorter tools that provide more accurate machining. The main aims of using 5-axis machining in industry are stated

to reduce cycle times, dimensional and surface errors in its nature. However, this cannot be achieved satisfactorily without the physical modeling of the milling process. Furthermore, while machining free-form surfaces; local peak forces may occur due to spatially changing engagement between the cutter and the workpiece. Hence, cutting force modeling gains more importance in order to prevent excessive cutter deflection and surface errors in these processes. In response to demand in industry for cutting force modeling, this thesis presents a mechanistic cutting force model for the 5-axis ball-end milling of free-form surfaces. The process methodology presented in this thesis is given in Figure 1.5.

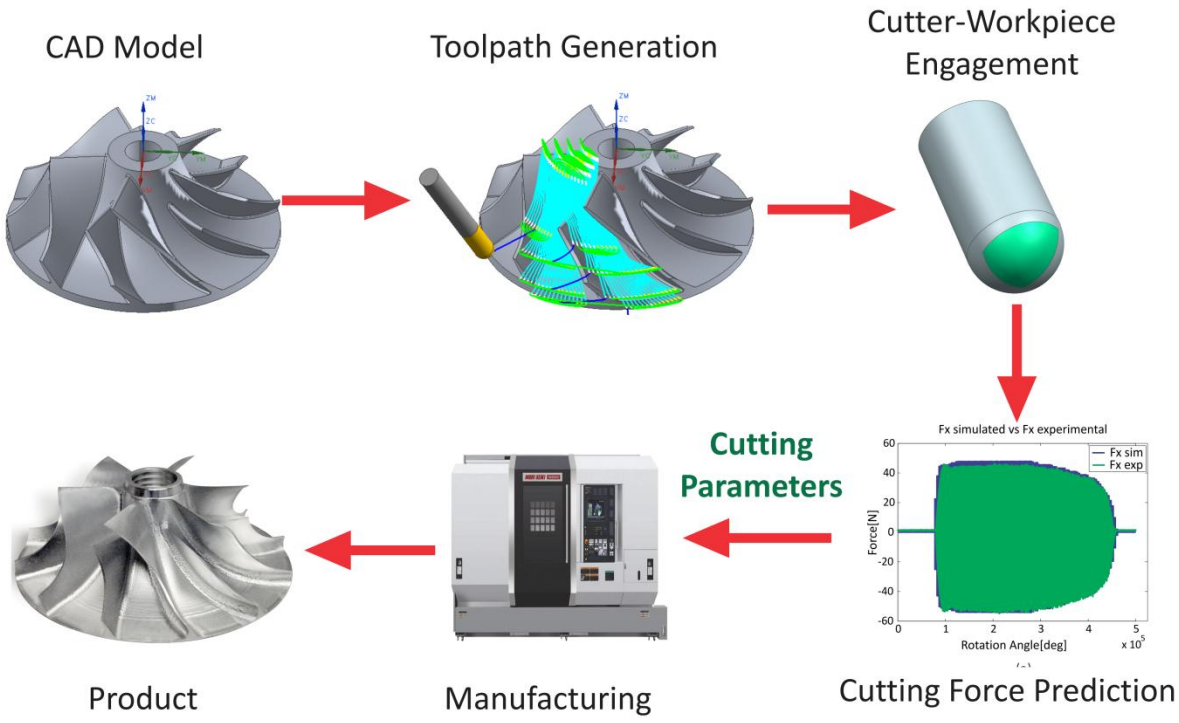

Figure 1.5: Process methodology

The thesis is organized as follows,

Chapter 2 presents the review of the literature on the cutting force prediction in 5-axis machining processes and the Cutter-Workpiece Engagement extraction schemes that are presented in the previous studies.

In Chapter 3, modeling of 5-axis machine tool kinematics is introduced and a generic post-processor with variable feedrate is developed. A virtual machine simulation model, which is capable of simulating machine tool movements from the NC code, is also presented.

Cutting forces in machining is determined by extracting the Cutter-Workpiece Engagement (CWE) from the in-process workpiece in the form of start and exit angles as a function of axial height along the tool axis. Chapter 4 describes a discrete method (Three-Orthogonal Dexelfield) of obtaining CWE maps for 5-axis ball-end milling is developed. It is compared with the solid-modeler based CWE calculation method. Solid-modeler Based cutter-workpiece engagement method is also given in Chapter 4 for convenience. Presented approach is developed by Huseyin Erdim, Ph.D. who is currently working at Mitsubishi Electric Research Laboratories (MERL) as a research engineer. The results of this CWE model are used in the validation tests.

In Chapter 5, mechanistic cutting coefficient calibration method given in [9] is implemented for different cutting speeds, feedrates and tool geometry on Al7039 and Al7075 workpiece materials. Besides, cutting force calibration methodology in rotating coordinate frame is developed.

A cutting force prediction model for 5-axis ball-end milling is developed in Chapter 6. Cutting force modeling is performed in the fixed coordinate frame (for table type dynamometer) and in the rotating coordinate frame (rotating coordinate dynamometer). The approach developed based on this model is modular. Therefore, different cutter and workpiece geometries and tool motions can be incorporated into the model without additional analysis.

Chapter 7 presents several validation tests and these validation tests demonstrate that presented cutter-workpiece engagement model is accurate and force predictions are in good agreement with the measured data.

Chapter 2

LITERATURE REVIEW

In this thesis, cutting force modeling in 5-axis ball-end milling is presented. Cutting force modeling in 5- axis machining comprises two main parts which are Cutter-Workpiece Engagement Calculation and Modeling of Cutting Forces. Previous research conducted on geometric modeling and physical modeling related to 5-axis machining is reviewed before introducing the performed study.

2.1 Cutter-Workpiece Engagement (CWE) Calculation

Cutter-workpiece engagement calculation is the extraction of the cut geometry from the intersection of the tool swept volume and the in-process workpiece in the form of start and exit angles as a function of axial height along the tool axis.

Accurate calculation of CWE (Cutter-Workpiece Engagement) is quite critical since in-cut region is determined based on the CWE map, and cutting forces are calculated using this information. Due to this fact, several CWE calculation methods were developed by different researchers. These methods can be given as, Solid-modeler based methods [10], [11], Discrete methods [12], [13], analytical methods [14], [15], faceted-methods [16] and Voxel-based methods [17].

2.1.1 Analytical methods

Analytical methods can be utilized for simple toolpaths in 2.5D end-milling [14], for monotonic surfaces in 3-axis ball-end milling [15], and as well as for 5-axis milling in slotting cases [18]. Analytical models provide the most efficient solution for simple cases;

however computation of the complex cases may not be feasible or applicable. For instance, 5-axis toolpaths with complex workpiece geometry, such as impeller stock workpiece, cannot be modeled unless closed-form equation of the hub and the shroud surfaces are known. Furthermore, surface-surface intersections are difficult to handle. Similarly, in 3-axis milling closed-form equation of the machined surface has to be given in order to obtain the CWE maps. Besides, blank workpiece is confined to rectangular workpiece geometry [15].

2.1.2 Solid-Modeler Based Methods

Solid-modeler based CWE calculation methods can overcome the limitations introduced by analytical methods since the cutter and the workpiece can be modeled using geometric primitives or complex geometric shapes. With this knowledge Voelcker and Hunt [10] were the first researchers investigated the NC verification from the solid modeling aspect applying Boolean subtraction operation for material removal simulation from the stock workpiece.

Later Wang [19] developed an NC verification system based on the concept of solid modeling. Developed system modeled the in-process workpiece by taking the Boolean difference of the tool swept volume from the blank geometry. In this method he used an analytical method for computing tool swept volumes and a ray casting algorithm for calculating Boolean operations. It has to be noted that, conceptually, Wang's approach is a solid modeling approach on the other hand; Boolean operations are performed using an image space (view based) method.

Spence and Altintas [20] used a solid-modeler based CWE extraction system for 2.5-axis end-milling employing the constructive solid geometry (CSG) representation for workpiece definition. Along the toolpath, for each toolpath segment cutting tool is intersected with all geometric primitives defining the workpiece. Then, cutter-workpiece

intersection information for each primitive is combined in order to form the complete engagement region. Updated workpiece (CSG tree) is also stored for further cutting passes.

Spence et al. [21] extended solid-modeler based CWE system for the simulation of ball-end milling and 5-axis milling by adopting the B-rep modeler of the ACIS solid modeling kernel.

Imani et al. [22] developed a geometric simulation module for simulating 2-axis and 3-axis ball-end milling operations using ACIS solid modeling kernel which can extract the chip geometry. Then, Imani et al. [23] enhanced their geometric simulation module [22] for 3-axis ball-end milling of free-form surfaces for semi-finishing and finishing operations. Material removal is simulated by subtracting the B-rep model of the tool swept volume from the in-process workpiece, in order to extract the feed-mark and scallop geometries.

More recently, Ferry and Yip-Hoi [24] proposed a semi-discrete solid modeling based method in order to obtain cutter-workpiece engagement data for five-axis flank milling with tapered ball-end mills. In this work, using the ACIS solid modeling kernel tool swept volume is subtracted from the workpiece at each toolpath segment and removal volume is obtained. Then, the removal volume is sliced into a number of parallel planes along the intermediate axis of the two consecutive cutter locations, and the intersection curves are determined. Finally, endpoints of the intersection curves are joined with lines for forming the engagement polygon where the engagement domain is calculated from this polygon.

2.1.3 Discrete Methods

The fundamental problem related to the solid modeling based methods is the computational cost. Voelcker and Hunt [10] reports that the computation time using CSG is proportional to the fourth power of the number of the tool movements. Until now, much research has been devoted to discrete simulation of NC machining processes [25], [26],

[27], [28]. Commonly, these methods use the Z-buffering technique which is primarily used for rendering in computer graphics.

Chappel [25] presented a method of using vectors to simulate the material removed by NC milling and developed a method for calculating vector intersections with a cylinder representing a milling cutter. This method was applicable up to 5-axis milling and also allowed the detection of the gouging.

Drysdale and Jerard [27] developed an approach for simulation of 3-axis NC machining of sculptured surfaces. In this method, blank workpiece is represented as a series of Z-vectors on an X-Y grid. Material removal is simulated by reducing the length of the Z-vector if an intersection occurs with the tool while it is moving.

Contrary to conventional Z-buffer approach Van Hook [26] used an extended Z-buffer for NC machining simulation where multiple heights can be stored in a single Z direction vector in a linked list data structure. The use of extended Z-buffer is pretty important for 3-axis milling with undercuts (i.e. T-slot machining) and 5-axis milling.

Fussell et al. utilized extended Z-buffer scheme for CWE calculation in 3-axis machining [29] and 5-axis machining [13]. Model validation in 5-axis machining is performed on roughing and semi-finishing toolpaths of centrifugal impeller geometry. In 5-axis machining simulation, tool movement is simplified to 3-axis moves where each toolpath segment is subdivided into smaller segments in order to limit the error introduced by this approximation. For improving computational efficiency intersection calculations are reduced to simple line primitive intersection calculations by modeling the tool swept volume as a combination of geometric primitives. Additionally, Z-buffer model was expanded to allow for the use of non-prismatic stock models such as parts with rotational symmetry and castings.

Roth et al. developed an adaptive and local depth buffer to calculate cutter-workpiece engagements for 3-axis machining [30], [31] and 5-axis machining [32]. This approach

aligned the depth buffer to the tool axis orientation and sized the depth buffer to the tool rather than the workpiece. Use of the adaptive and local depth buffer offers less memory storage, less computational load and increased simulation accuracy.

2.2 Modeling of Cutting Forces

One of the first studies on cutting force prediction was made by Wang [11] where he used Z-buffer technique in order to relate the cutting force with material removal rate; however the direction of the cutting force cannot be predicted with this approach. Since, the direction of the cutting force is important for determining cutter deflections Takata et al. [33] combined this approach with a mechanistic model [34] in order to predict cutting forces and tool deflections for 3-axis machining.

Following these studies, Spence and Altintas [20] and also Bailey et al. [35] developed solid modeler based cutter-workpiece engagement systems for cutting force prediction and feedrate scheduling by using this solid modeler and the mechanistic force model.

Yucesan and Altintas [36] developed a discrete mechanistic cutting force model for ball-end milling which was able to predict cutting forces accurately for known tool geometry.

Most of the research on five axis machining focused on the geometric aspects of this process such as toolpath generation, toolpath optimization and geometric verification of the toolpath. With the improvement in the CAM technology geometric constraints and errors can be eliminated, on the other hand, the physics of the process is not considered. Consequently, efficiency of the process and errors due to physical constraints cannot be predicted before the production of the part.

In the modeling of 5-axis machining processes noteworthy research was conducted by Zhu et al. [37] where Z-map technique is utilized for cutter-workpiece engagement for cutting force prediction and feedrate selection based on the instantaneous chip load. A

process fault detection and fault diagnosis methodology is developed[38]. Cutter runout and flute chipping/breakage are identified by examining the power spectrum magnitudes at low spindle frequency harmonics.

Similarly, Fussell et al. [13] developed a 5-axis virtual machining environment for discrete simulation of sculptured surface machining which aims automatic feedrate selection along the toolpath via mechanistic modeling of cutting forces. Feedrate selection is based on the concept of limiting the cutting force at a given value.

Bailey et al. [39] proposed a generic mechanistic cutting force model for simulating multi axis machining of complex sculptured surfaces using a cutting edge representation defined by a NURBS curve. A process optimization tool [40] is presented by employing a feed scheduling method using the maximum chip load and cutting force as constraints.

Becze et al. [41] introduced an analytical chip load model for 5-axis high-speed milling of hardened tool steel. The effect of tilt angle on cutting forces, tool wear mechanisms and also surface integrity is investigated in this study.

Some of the most recent studies on modeling of five axis milling was done by Ozturk and Budak [18], Tunc and Budak [42]. Analytical modeling of cut geometry of 5-axis machining is performed and obtained data is used for cutting force prediction and process optimization.

Ferry and Altintas [43] developed a virtual machining simulation system for 5-axis flank milling of jet engine impellers extending the force model developed by Yucesan and Altintas [36]. Off-line multi-constraint-based feedrate optimization of the process is introduced [44]. The constraints are determined to be the tool shank bending stress, tool deflection, maximum chip thickness and the torque limit of the machine.

Chapter 3

5-AXIS MACHINE TOOL KINEMATICS

3.1 Introduction

5-axis machine tool kinematics is an important concept for 5-axis machining processes since accurate conversion of the CAM output to NC data is crucial. Therefore, in this thesis a postprocessor for a Mori Seiki NMV5000 DCG machine tool is developed. Postprocessors are important tools for converting CAM output into the machine tool language in the form of G-codes. In general, a postprocessor is an inverse kinematics solver which determines the kinematic configuration of the machine at a specific cutter location. Improvements in the machine tool and the machining process technologies increased the need for generic postprocessors in order to exploit the capabilities of the machine tools. Next generation machining technologies such as force based feedrate scheduling and toolpath optimization requires the implementation of the variable feedrate during toolpath which also constitutes the aim of this thesis. Therefore, a generic postprocessor for table-tilting type five-axis machine tool with variable feedrate and a practical method for avoiding kinematic singularities are introduced.

Validation of an inverse kinematics solver for a machine tool can performed in two ways. One of them is running test cuts on the machine, and the other one is the virtual machine simulation. Running machining tests (dry runs) on the machine is both time-consuming and costly for this reason a virtual machine simulation module is developed for the validation of the presented postprocessor. Via virtual machine simulation same scenario on the machine tool is simulated considering postprocessing and machine tool controller specific conditions.

3.2 Configuration and Kinematic Modeling of Five-Axis Machine Tool

Solid model of the NMV 5000DCG five-axis milling machine is shown in

Figure 3.1. The machine has three orthogonal translational axes and two orthogonal rotary axes. The rotary axes B and C are on the table of the machine, therefore it is called table/tilting-rotating type five-axis machine. Positive directions of the machine axes are shown in Figure 3.1. The working range of B axis is $[-180°, 160°]$ and the working range of C axis is$[-9999°, 9999°]$.

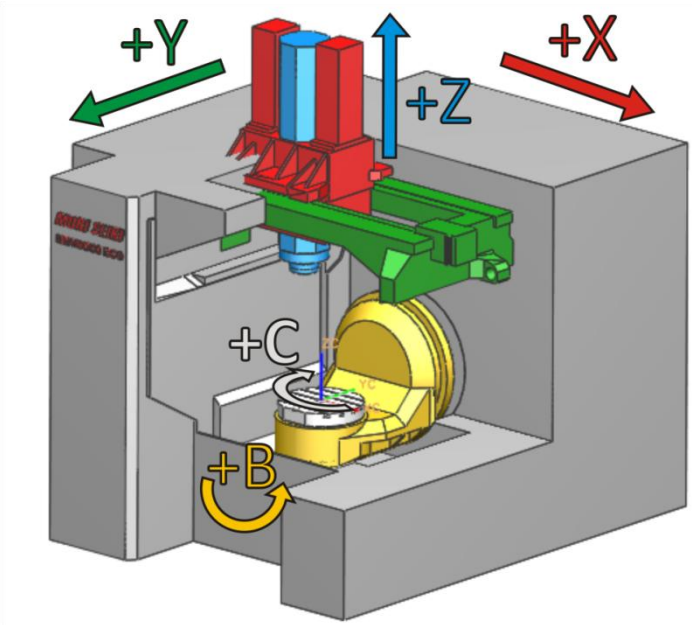

Figure 3.1: Solid Model of five-axis milling machine.

A five-axis machine tool can be considered as a kinematic chain with serially linked rigid bodies comprising of three translational and two revolute joints. Therefore, the forward and inverse kinematics of the machine tool can be obtained using homogenous transformation matrices by defining necessary coordinate frames. General forms of transformation matrices for translational and rotational joints are given in Equation (3.1) and (3.2) respectively.

$$T = \begin{bmatrix} 1 & 0 & 0 & x \\ 0 & 1 & 0 & y \\ 0 & 0 & 1 & z \\ 0 & 0 & 0 & 1 \end{bmatrix} \tag{3.1}$$

$$R(V,\theta) =$$

$$\begin{bmatrix} V_x^2(1-c\theta)+c\theta & V_xV_y(1-c\theta)-V_z\sin\theta & V_xV_z(1-c\theta)+V_ys\theta & 0 \\ V_xV_y(1-c\theta)+V_zs\theta & V_y^2(1-c\theta)+\cos\theta & V_yV_z(1-c\theta)-V_xs\theta & 0 \\ V_xV_z(1-c\theta)-V_ys\theta & V_yV_z(1-c\theta)+V_xs\theta & V_z^2(1-c\theta)+c\theta & 0 \\ 0 & 0 & 0 & 1 \end{bmatrix} \tag{3.2}$$

where $c\theta = \cos\theta$ and $s\theta = \sin\theta$

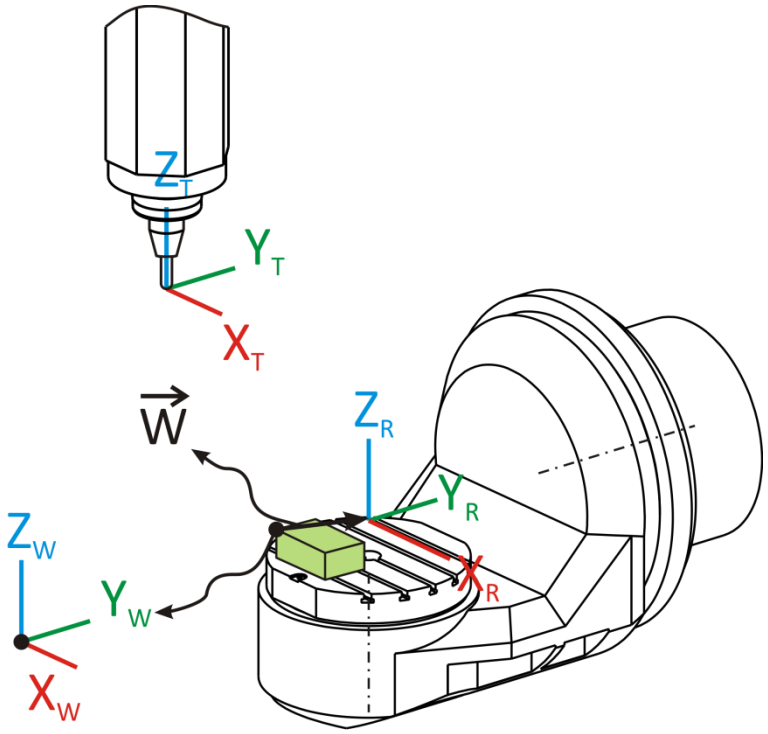

Figure 3.2: Definition of Coordinate Frames

Translation matrix T defines a motion along an arbitrary direction, where in vector notation is equal to $T = x\,\boldsymbol{i} + y\,\boldsymbol{j} + z\,\boldsymbol{k}$. Equation (3.2) describes a rotation around an

arbitrary vector $V = V_x\,\boldsymbol{i} + V_y\,\boldsymbol{j} + V_z\,\boldsymbol{k}$ by an angle of θ. Considering positive direction of rotation according to right hand rule rotation vectors for B and C axes are given as:

$$V_B = [0, -1, 0] \tag{3.3}$$

$$V_C = [0, 0, -1] \tag{3.4}$$

For a general five-axis motion, the path between two cutter location (CL) points can be defined as a 3D spline, where cutting tool moves relative to the workpiece. In order to define five-axis motion three coordinate frames is introduced as:

$X_T - Y_T - Z_T$: The fixed coordinate frame attached to the tooltip of the cutter.

$X_R - Y_R - Z_R$: The center of rotation of two rotary axes intersects at a point where machine rotary zero and the rotary zero coordinate frame are located.

$X_W - Y_W - Z_W$: Workpiece coordinate frame attached to the blank workpiece mounted on the machine. In practical use, it is also called work offset or fixture offset.

Detailed illustration of the coordinate frames is shown in Figure 3.2. The vector $\overrightarrow{W}$ in Figure 3.2 represents the offset distance from the workpiece coordinate frame to the rotary zero coordinate frames and denoted as $\overrightarrow{W} = W_x\boldsymbol{i} + W_y\boldsymbol{j} + W_z\boldsymbol{k}$.

As it is stated before, the position and the orientation of the cutting tool relative to workpiece coordinate frame can be obtained using homogenous transformations sequentially. First, workpiece coordinate frame is translated by the offset vector $\overrightarrow{W}$. Then, two consecutive rotations for C and B axis of the machine around Z_R and Y_R coordinate frame axes are applied respectively. Finally, the translation by a vector $\vec{D}$ is applied to construct the kinematic relationship. Overall transformation matrix which constitutes the forward kinematics of the machine can be given as:

$$T(W_x, W_y, W_z)R(Z_R, -\theta_z)R(Y_R, -\theta_y)T(D_x, D_y, D_z)\begin{bmatrix} 0 & 0 \\ 0 & 0 \\ 0 & 1 \\ 1 & 0 \end{bmatrix} \tag{3.5}$$

In Equation (3.5), θ_z represents the rotation angle of C axis and θ_y represents the rotation angle of B axis of the machine. These two rotations formulated to be in the negative direction because positive angles for machine rotary axes are in the opposite direction.

Inverse kinematics equations can be obtained by solving Equation (3.5).In a CLSF (Cutter Location Source File) or simply CL file, the position of the tooltip and the orientation of the tool are given as:

$$P = P_x\boldsymbol{i} + P_y\boldsymbol{j} + P_z\boldsymbol{k} \tag{3.6}$$

$$T = T_x\boldsymbol{i} + T_y\boldsymbol{j} + T_z\boldsymbol{k} \tag{3.7}$$

In matrix form it can be expressed as:

$$\begin{bmatrix} P & T \\ 1 & 0 \end{bmatrix} = \begin{bmatrix} P_x & T_x \\ P_y & T_y \\ P_z & T_z \\ 1 & 0 \end{bmatrix} \tag{3.8}$$

Since, Equation (3.5) and (3.8) are equal by solving these equations simultaneously, unknown parameters θ_y, θ_z and $\vec{D}$ can be found.

$$\begin{bmatrix} T_x \\ T_y \\ T_z \\ 0 \end{bmatrix} = \begin{bmatrix} -c\theta_z s\theta_y \\ s\theta_z s\theta_y \\ c\theta_y \\ 0 \end{bmatrix} \tag{3.9}$$

$$\begin{bmatrix} P_x \\ P_y \\ P_z \\ 1 \end{bmatrix} = \begin{bmatrix} D_x\{c\theta_z c\theta_y\} + D_y\{s\theta_z\} + D_z\{-c\theta_z s\theta_y\} + W_x \\ D_x\{-s\theta_z c\theta_z\} + D_y\{c\theta_z\} + D_z\{s\theta_z s\theta_y\} + W_y \\ D_x\{s\theta_y\} + D_z\{c\theta_y\} + W_z \\ 1 \end{bmatrix} \tag{3.10}$$

The rotation angles θ_y and θ_z have to be determined first from Equation (3.9). However, rotation angle θ_y is determined and then θ_z is solved accordingly because the solution for θ_z depends on the angle θ_y.

There are two possible solutions for θ_y which can be given as:

$$B = \theta_y = \cos^{-1}(T_z) \text{ for } 0 \leq \theta_y \leq \pi \tag{3.11}$$

$$B = \theta_y = -\cos^{-1}(T_z) \text{ for } -\pi \leq \theta_y \leq 0 \tag{3.12}$$

Considering the operating point of the machine appropriate solution for B axis has to be selected and, at each CL point validity of the solution has to be checked. This selection procedure is explained in Section 3.3. Rotation angle for C axis is found as:

$$C = \theta_z = atan2(T_y, T_x) \tag{3.13}$$

where $atan2$ is a four quadrant arctangent function.

Once rotation angles of the rotary angles are determined, position of the tooltip denoted as X, Y, Z is calculated by solving Equation (3.10) simultaneously as:

$$\begin{aligned} X = D_x + W_x &= [P_x - W_x]\{c\theta_z c\theta_y\} + [P_y - W_y]\{-s\theta_z c\theta_y\} + [P_z - W_z]\{-s\theta_y\} + W_x \\ Y = D_y + W_y &= [P_x - W_x]\{s\theta_z\} + [P_y - W_y]\{c\theta_z\} + W_y \\ Z = D_z + W_z &= [P_x - W_x]\{c\theta_z s\theta_y\} + [P_y - W_y]\{-s\theta_z s\theta_y\} + [P_z - W_z]\{c\theta_y\} + W_z \end{aligned} \tag{3.14}$$

3.3 Linearization and NC Data Correction

3.3.1 Linearization

In CAM packages, CL data is generated directly from the toolpath data considering that actual five-axis motion follows a linear trajectory. On the other hand, due to simultaneous movement of linear and rotary axes of the machine, actual toolpath and programmed

toolpath between two consecutive CL points deviate. This phenomenon is shown in Figure 3.3.

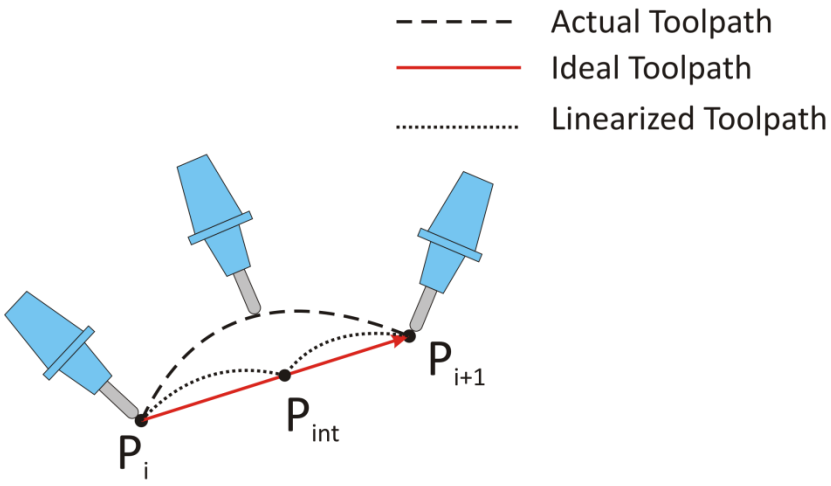

Figure 3.3: Linearization in Five-Axis Machining

In Figure 3.3, points P_i and P_{i+1} are two consecutive CL points from CL data, point P_{int} is the interpolated CL point as a result of linearization. Since, presented postprocessor will be used for feedrate scheduling or optimization purposes in five-axis machining; in this study linearization of the generated CL data is not used because CL data and the NC data have to match each other exactly. Any difference in the CL data and the corresponding NC data will directly affect engagement boundaries of the tool with the workpiece and the resulting cutting force. Instead of linearization, toolpath generation tolerance of CAM package is adjusted to minimize the deviations.

For convenience, a linearization algorithm could be introduced, however most of the existing interpolation methods [45], [46] are linear and interpolation of tool orientation vectors are not accurate. Spline interpolation may reduce the deviation from the actual toolpath and this may be studied as a future work but it is out of the scope of this thesis.

3.3.2 NC Data Correction

In Chapter 3.2 kinematic modeling of the machine tool is introduced and it is shown that there are multiple possible solutions for B and C axis angles. Therefore, appropriate solution among these candidates has to be chosen. For determining the B axis angle a simple yet effective method is used. For the first CL point in the CL data, lead angle of the tool with respect workpiece is found, and then the solution having the same sign with the lead angle is chosen.

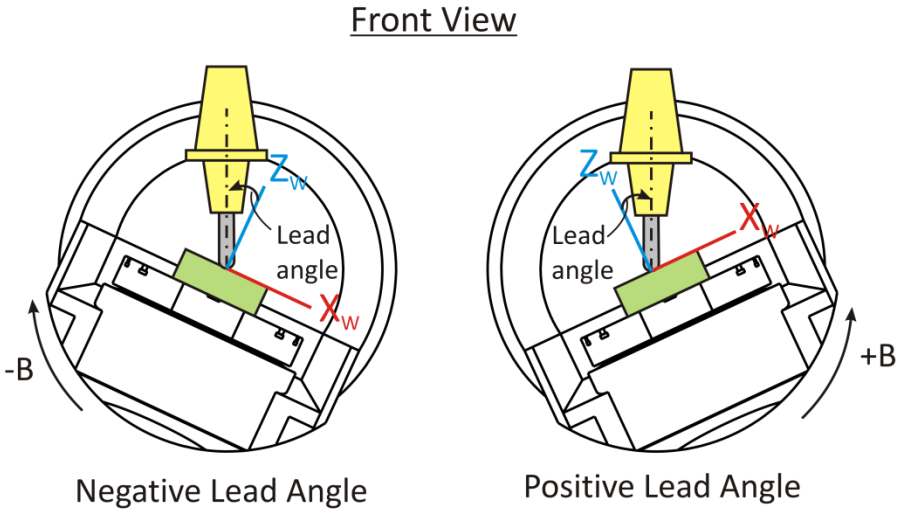

Figure 3.4: Relationship between Lead Angle and B Axis Angle

In Figure 3.4 the relationship between lead angle and the B axis angle is shown. Lead angle is defined as the rotation angle about Y_w which is Y axis of workpiece coordinate frame. Lead angle is calculated as:

$$lead = atan2(T_x, \sqrt{T_y^2 + T_z^2}) \tag{3.15}$$

For first CL point modifying the solution for B yields:

$$B = sgn(lead)cos^{-1}(T_z) \tag{3.16}$$

Following angles for B axis determined according to previous B axis angle selecting the solution which cause the shortest rotational motion.

Modification in C axis angles has to be made also. In Equation (3.13) C axis angle is determined by $atan2$ function which is a four quadrant function and gives the rotation angles in the range of $[-\pi, \pi]$. Therefore, appropriate solution for C axis has to be selected. Especially around kinematic singularities, sometimes C axis of the machine has to make quick turn which may damage the workpiece or may even result collision.

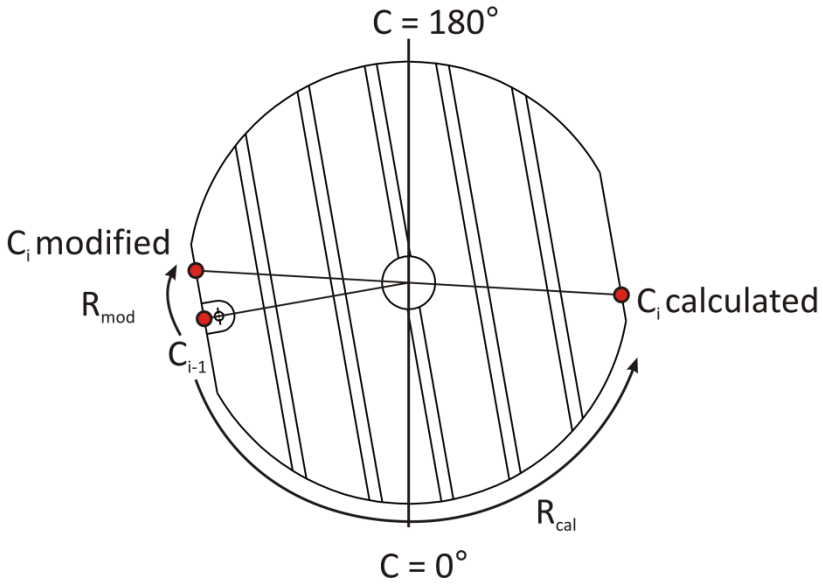

Figure 3.5: C Axis Angle Modification Method

Another reason for this situation is that, if the actual operating range of the machine allows more or less than the specified operating range and actual axis positions exceed these limits an alternative solution will be generated. If this is the case, rotary axis will make a full rotation in the opposite direction to reach the commanded position.

In proposed approach, which is shown in Figure 3.5, previous C axis angle C_{i-1} is compared with the current C axis angle $C_i\ calculated$ for each CL point in the toolpath if the absolute difference between two consecutive rotations is greater

than 90°, calculated rotation angle is increased or decreased by $\pm 90°$ until the modified rotation angle and the previous rotation angle lie in the appropriate range. An example of the proposed approach is shown in Figure 3.6.

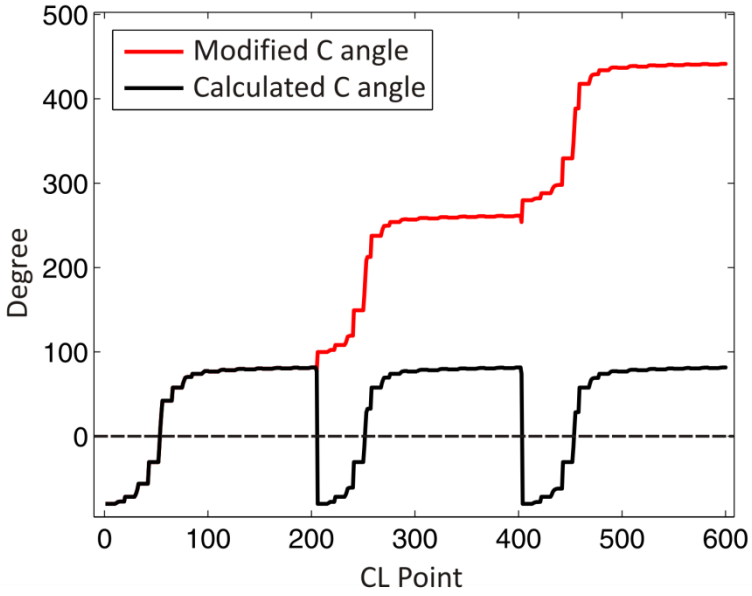

Figure 3.6: C Axis Angle Modification Example

From Figure 3.6, it is obviously seen that with the modification approach quick turns along the toolpath are avoided and a continuous rotation around the rotary axis is obtained. Since, continuous rotation in the toolpath along the same feed direction is satisfied possible feed marks due to feed direction change are also eliminated with this approach.

3.4 Virtual Simulation Module

A virtual machine simulation module is developed for determining the correctness of the postprocessed NC code. Flow chart for virtual machine simulation module is shown in Figure 3.7.

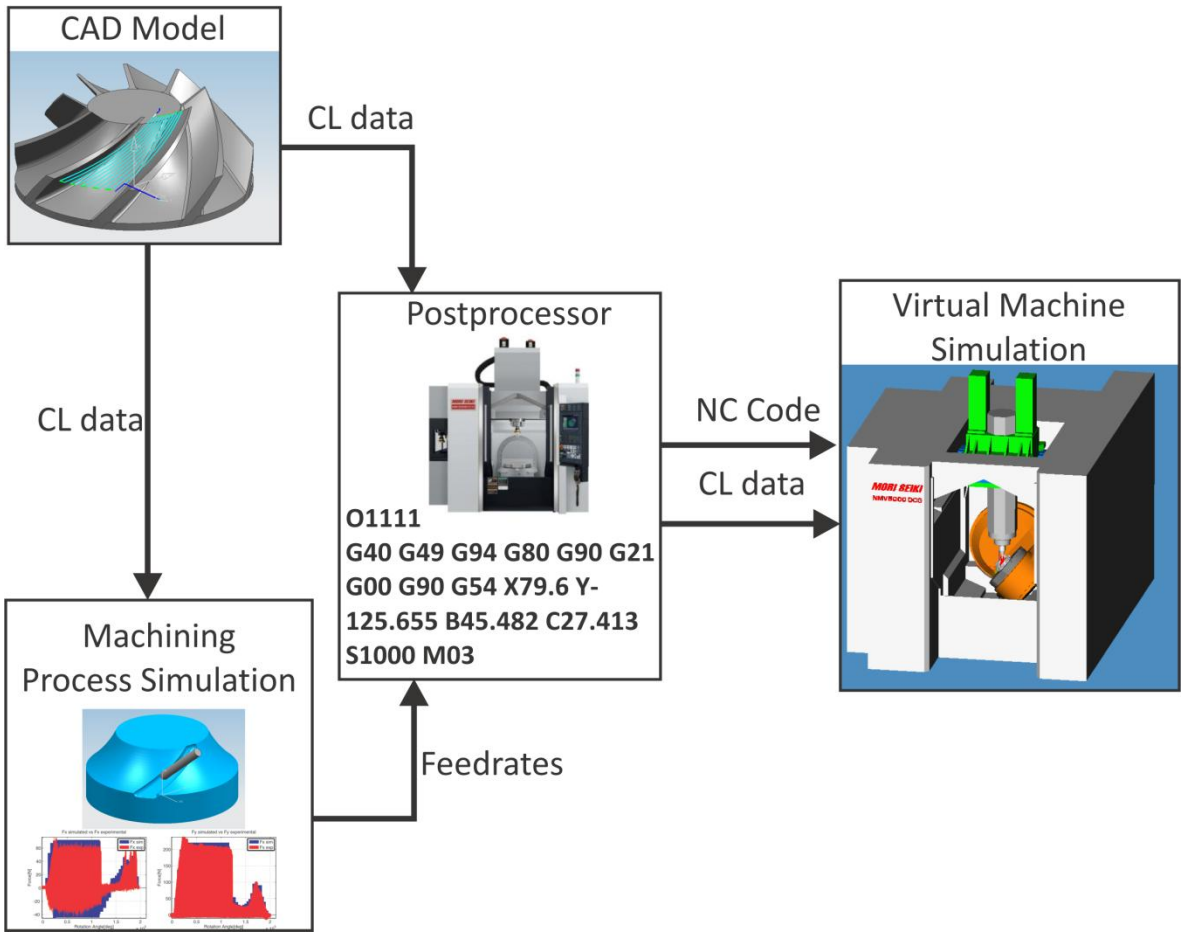

Figure 3.7: Virtual Simulation Module Flow Chart

The approach for virtual simulation can be summarized as follows. First, toolpath is generated using a CAM package, then the output CL data is used for physical simulation of machining process in machining process simulation module where cutting forces are simulated and a feedrate scheduling strategy is applied [47]. Corresponding feedrates for each CL point is obtained. By using this feedrate array and the CL data NC code is generated.

In virtual machine simulation module, machine parts are assembled using STL (Stereolithography) files for each axis of the machine. All simulation related parameters

such as tool offset, workpiece zero, machine home coordinate are set. NC code is used for the motion simulation of the machine axes which are postprocessed relative to workpiece zero. CL data is used for the illustration of the toolpath in the simulation. Validity of the NC code is proved by comparing CL data (toolpath in simulation) and tooltip position of the machine. If tooltip position and the corresponding CL point match then NC code is verified.

3.5 Implementation and Verification

The virtual machine simulation module described in Section 3.4 was implemented in Visual Studio C++ using the Coin3D graphics development API. Implementation of the proposed approach and virtual machine simulation module is verified on an impeller roughing toolpath which is shown in Figure 3.8. Toolpath is generated in Siemens NX6 software.

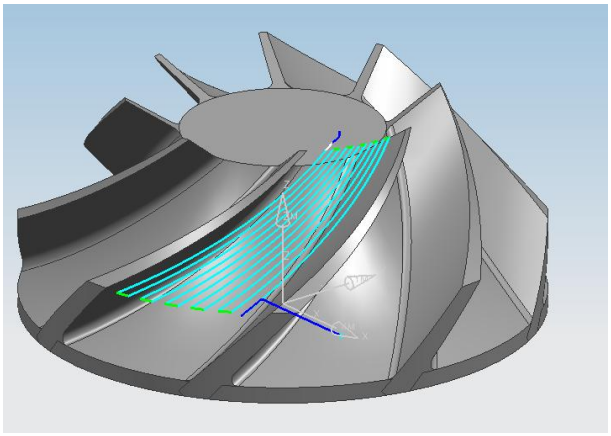

Figure 3.8: Impeller Roughing Toolpath.

For postprocessing, programmed zero is located at the bottom center of the workpiece and part is directly mounted on the C axis table, therefore workpiece offset distance is set to $W = 0\boldsymbol{i} + 0\boldsymbol{j} + 80\boldsymbol{k}$ mm. Selected tool and the holder have a tool offset length of 150 mm. The distance from the machine home position to the workpiece zero is $365\boldsymbol{i} - 255\boldsymbol{j} -$

640$\boldsymbol{k}$ mm. Virtual machine simulation module user interface and close-ups for 300th CL points are shown in Figure 3.9. In Figure 3.10, sample output of the NC code and the code postprocessed with a commercial postprocessor generated by NX6 Post Builder is shown.

From Figure 3.9 and Figure 3.10, it can be seen that programmed five-axis motion in the NC code matches perfectly with the CL data positions, therefore it may be concluded that the validity of the presented postprocessor and virtual machine simulation module is proved.

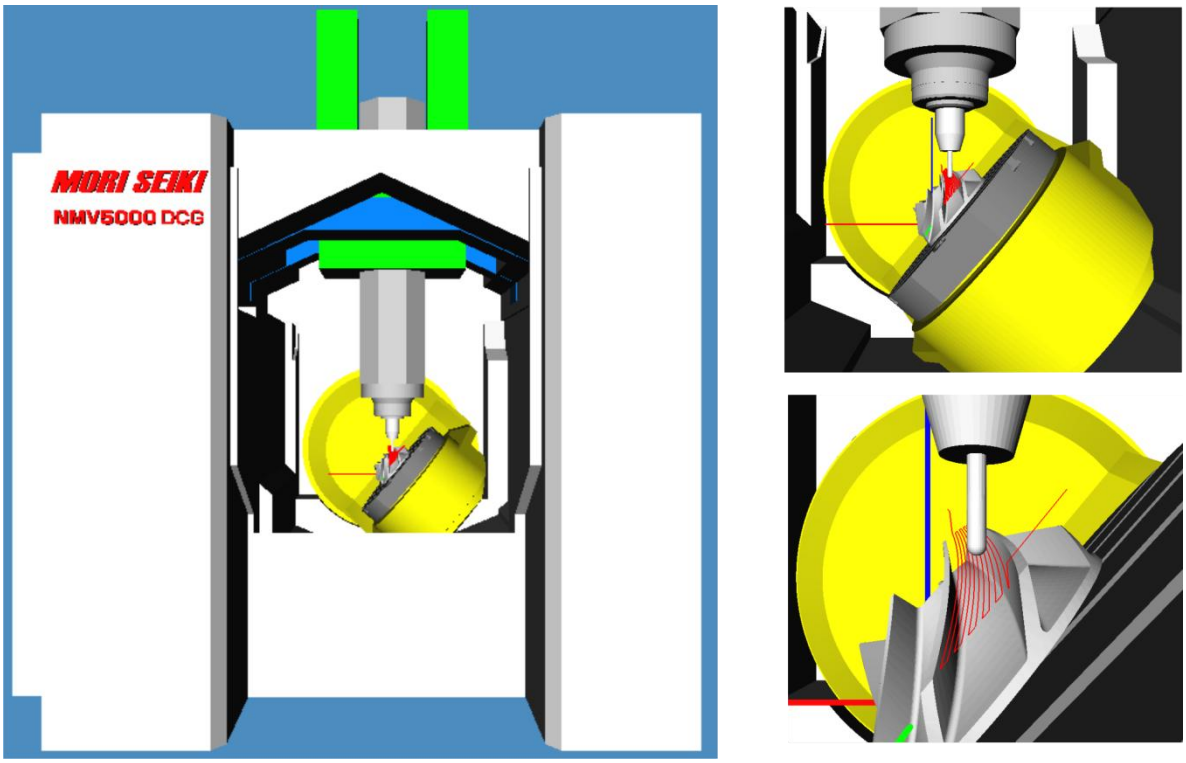

Figure 3.9: Virtual Machine Simulation Module and Close-ups for 300th CL Point

NX6 Post Builder Generated	Proposed method
G00 G90 G54 X17.607 Y-129.212 B45.482 C27.413 S0 M03 G43 Z96.562 H01 X-9.237 Y-109.356 Z69.264 Z45.264 G01 X-9.191 Y-108.494 Z44.465 F250. X-9.138 Y-107.492 Z43.85 X-9.08 Y-106.391 Z43.442 X-9.019 Y-105.231 Z43.258 X-8.957 Y-104.057 Z43.303 X-8.896 Y-102.915 Z43.577 X-8.84 Y-101.848 Z44.069 X-8.79 Y-100.897 Z44.76 X-8.454 Y-99.579 Z46.15 B45.564 C27.135 X-8.44 Y-99.509 Z46.22 B45.567 C27.124	G00 G90 G54 X17.6 Y-129.213 B45.482 C27.413 S1000 M03 G43 Z96.564 H5 X-9.237 Y-109.356 Z69.264 Z45.264 G01 X-9.191 Y-108.494 Z44.465 F250. X-9.138 Y-107.493 Z43.851 F250. X-9.079 Y-106.391 Z43.443 F250. X-9.018 Y-105.231 Z43.258 F250. X-8.957 Y-104.057 Z43.304 F250. X-8.896 Y-102.915 Z43.578 F250. X-8.840 Y-101.848 Z44.070 F250. X-8.790 Y-100.897 Z44.760 F250. X-8.454 Y-99.578 Z46.149 B45.564 C27.135 F255. X-8.440 Y-99.510 Z46.219 B45.567 C27.124 F253.

Figure 3.10: Sample Output of the NC Code

Chapter 4

CUTTER-WORKPIECE ENGAGEMENT MODEL

4.1 Introduction

In sculpture surface machining, the cutter/workpiece engagement region does vary along the cutter path and in general, unless some specific and very simple workpiece geometry is machined, it is difficult to find an exact analytical representation for the engagement region. Chip load and force calculations are based on the cutter/workpiece engagements; therefore the output of the engagement model is very critical. Mathematically, the swept volume is the set of all points in space encompassed within the object envelope during its motion. The basic idea in NC verification and simulation is to remove the cutter swept volume from the workpiece stock and thus to obtain the final machined surfaces.

In literature, NC machining simulation can be mainly categorized into three major approaches. The first approach is the exact Boolean, the second approach is the spatial partitioning, and the third approach is the discrete vectors. The direct Boolean subtraction approach is an exact and analytical approach. It directly performs the Boolean subtraction operation between a solid model and the volume swept by a cutter between two adjacent tool positions. Although this approach can provide accurate verification and error assessment, the computation cost is known to grow too much for a large number of tool-paths. The second approach uses spatial partitioning representation to define a cutter and the workpiece. In this approach, a solid object is decomposed into a collection of basic geometric elements, for example Z-map (Z-buffer), voxel, and ray representation, thus simplifying the processes of regularized Boolean set operations. However, its computation

time and memory consumption are increased drastically to get better accuracy. One of the other widely used NC simulation methods is based on the vector-clipping approach.

In this study both Solid based (Direct Boolean) method and Spatial partitioning method (Depth Buffer) is utilized. Solid Modeler based cutter-workpiece engagement method presented in Chapter 4.2 and Depth Buffer method is presented in Chapter 4.3.

4.2 Solid Modeler Based Cutter-Workpiece Engagement

Currently the most popular schemes used in solid modelers are the Boundary representation and Constructive Solid Geometry (CSG). In the B-rep methodology an object is represented by both its boundaries defined by faces, edges, vertices and the connectivity information.

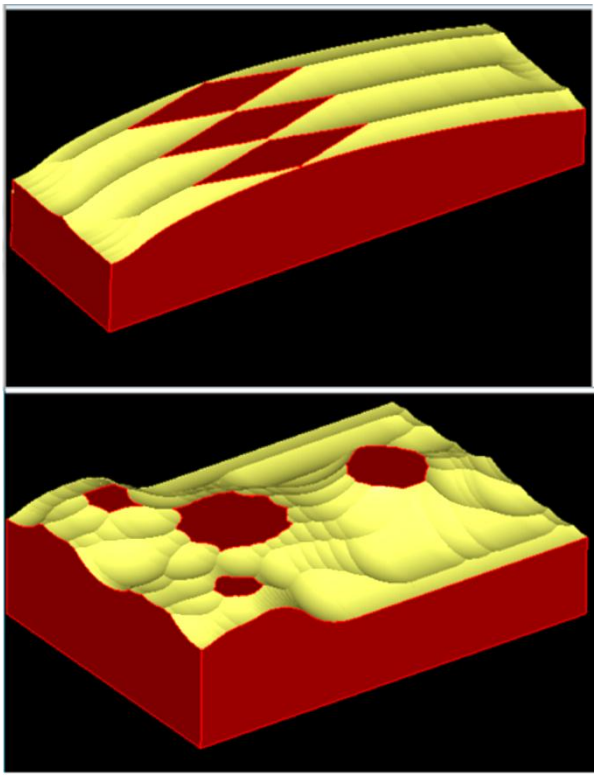

Figure 4.1: Simulated machined surfaces for airfoil and penguin surface geometry.

The prototype program is implemented using the commercial Parasolid solid modeler kernel. The tool movements are subtracted from the workpiece model by using Parasolid 'PK_BODY_sweep' and 'PK_BODY_boolean_2' function in order to find the in-process machined surface. Figure 4.1 shows the resultant machined surfaces for the airfoil and penguin surface examples used in Chapter 7.

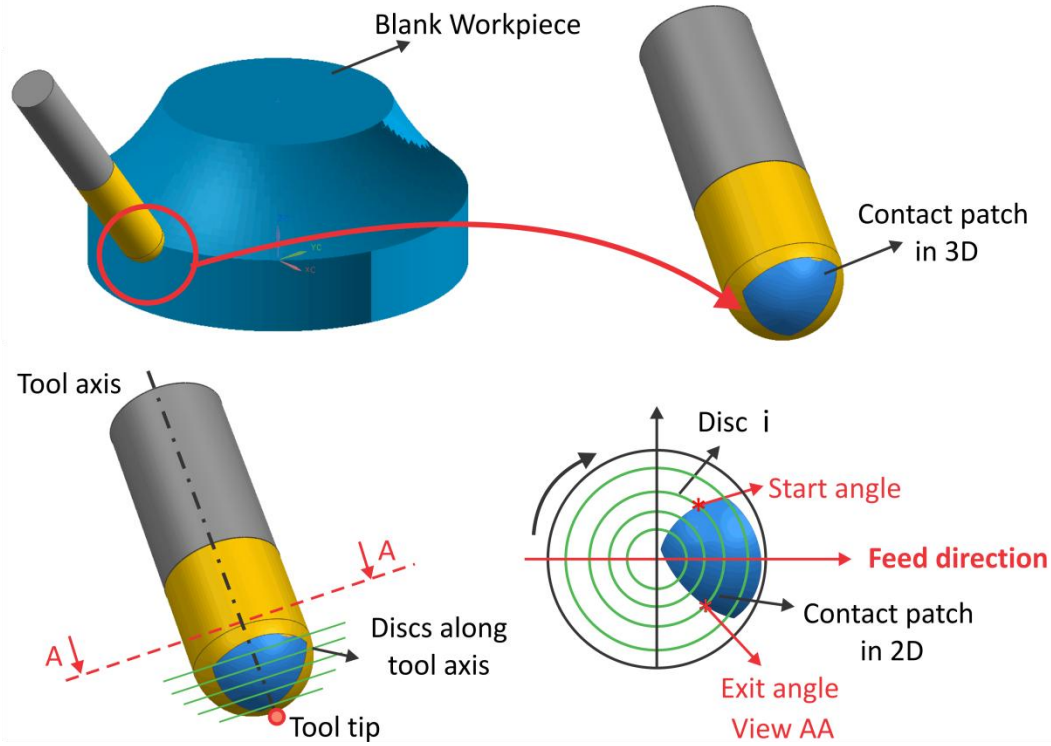

Figure 4.2: Cutter-workpiece engagement geometry extraction for ball-end mill

Once the in-process workpiece is obtained for each CL point, the contact patch surface between the tool and workpiece can be extracted by using Parasolid 'PK_BODY_boolean_2' function. Then, the resulting 3D contact surface, as illustrated in Figure 3, is projected to the plane perpendicular to the cutter axis by using parasolid 'PK_BODY_make_curves_outline' function. This step finds the enclosing boundaries and curves of the contact patch. Since the force model discretizes the cutter into slices

perpendicular to the tool axis and to perform force calculation for each slice, the discs at each level are projected to the plane perpendicular to the cutter axis.

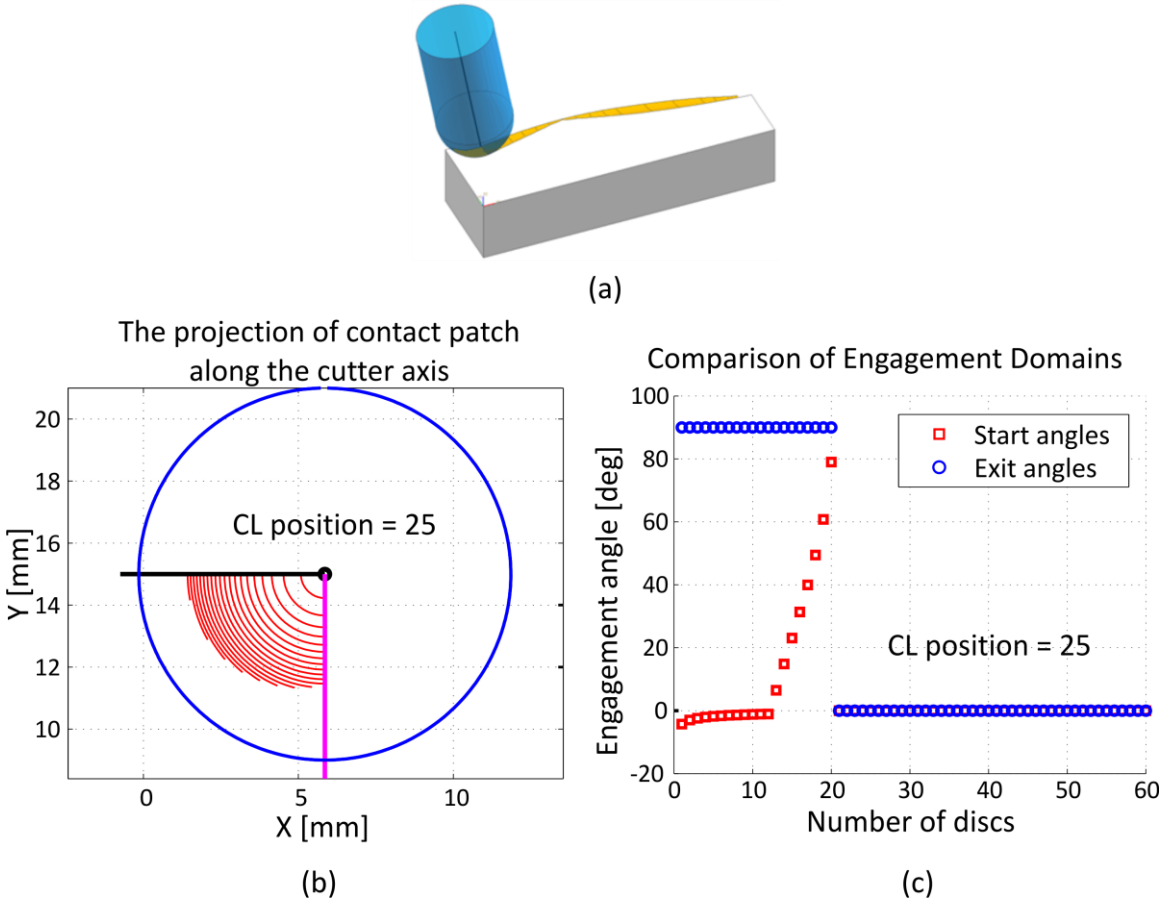

Figure 4.3: The engagement domain for CL point #25 for airfoil geometry test: (a) Previously machined surface with the tool instance, (b) Projected view of contact patch along cutter axis, (c) Start and exit angles for the discs along the cutter axis

Since engagement domain is simply the combination of start and exit angles of each discrete disc located on the cutter, the next step is to assign the start and exit angles to each respective projected disc by intersecting the 2D discs with the boundaries of the contact patch in plane by using Parasolid 'PK_CURVE_intersect_curve' function. A final step is

required to convert the intersection points into start and exit angles that are required for the force prediction model. Cutter-workpiece engagement geometry extraction for ball-end mill is shown in Figure 4.2.

The procedure described above is implemented in Visual Studio.NET using the Parasolid solid modeling Kernel and Parasolid Workshop on a Windows Core2Duo, 1.8 GHz/4GB Personal Laptop. The output of the program is processed in Matlab and the engagement angles are shown together with the contact patch for CL point #25 in Figure 4.3 for the airfoil geometry test. The computation time for the engagement domain for the corresponding examples are 21 sec and 48 sec for airfoil (137 CL points) and penguin (415 CL points) surfaces respectively.

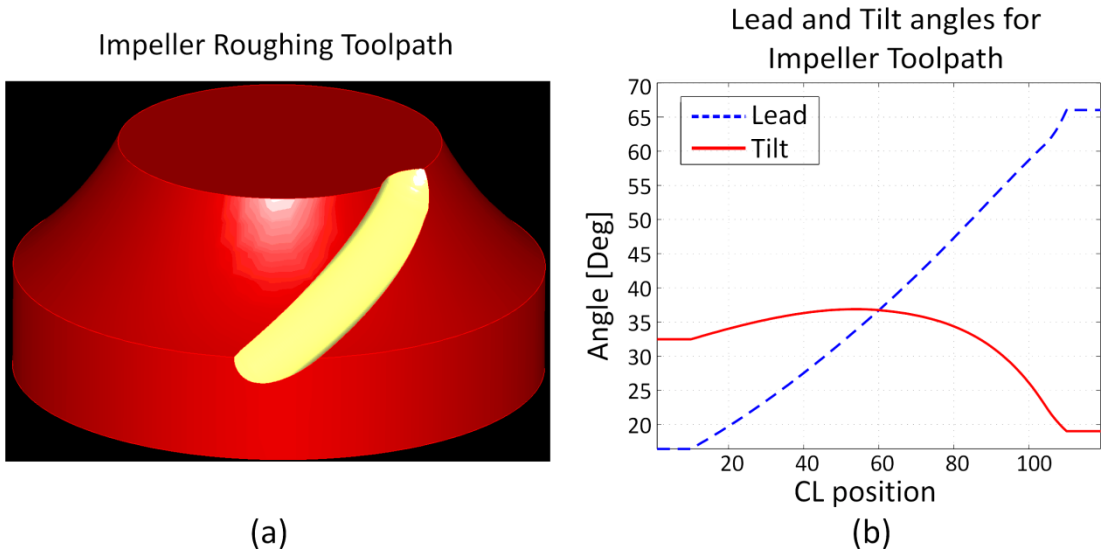

Figure 4.4: (a) Simulated workpiece for one-pass from Parasolid, (b) Lead and tilt angles for one-pass of impeller toolpath

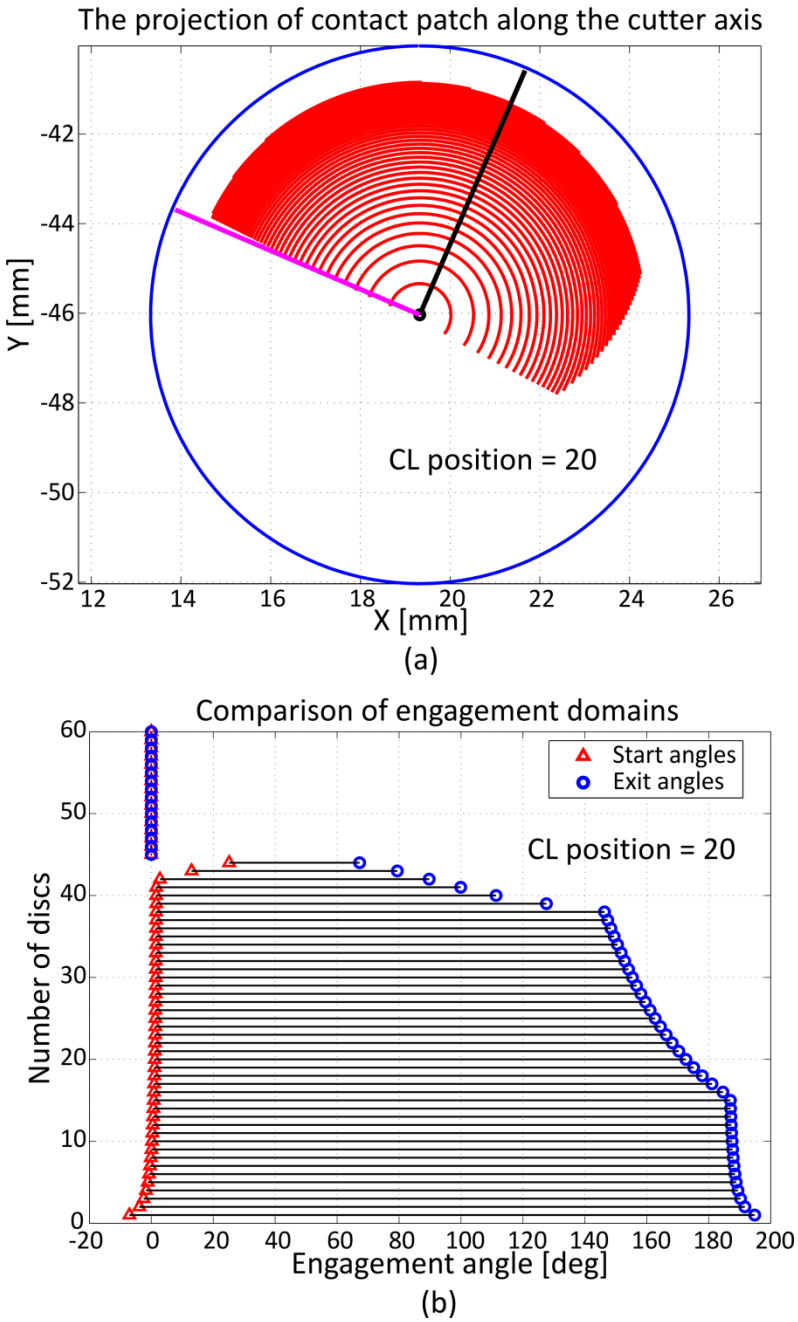

Figure 4.5: The engagement domain for CL point #20: (a) Projected view of contact patch along cutter axis, (b) Start and exit angles for the discs along the cutter axis.

For impeller toolpath, forces are compared for one pass where the tool moves from the lower rim of the cylinder workpiece to the upper rim of the cylindrical workpiece. This one pass has 119 CL points, the lead and tilt angles for one-pass is shown together with the simulated workpiece in Figure 4.4. The computation time for the engagement domain for this one-pass is 58 seconds for 119 CL points.

Engagement domains for the impeller toolpath are shown together with the contact patches for CL points #20 and #86. Figure 4.5 shows the engagement domain for CL point #20, where the engagement domain is one piece.

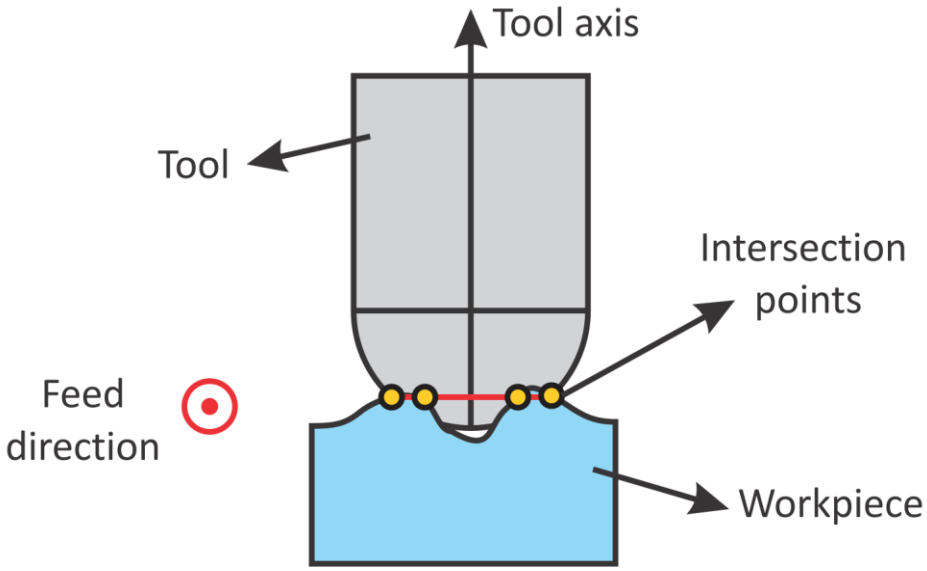

Figure 4.6: Illustration of multiple contact regions and intersections

However, the engagement domain can have more than one piece because of the complexity of the geometry of the workpiece and the tool motion as shown simply in Figure 4.6. In this case, the engagement domain will have more than two intersections for the discs along the cutter.

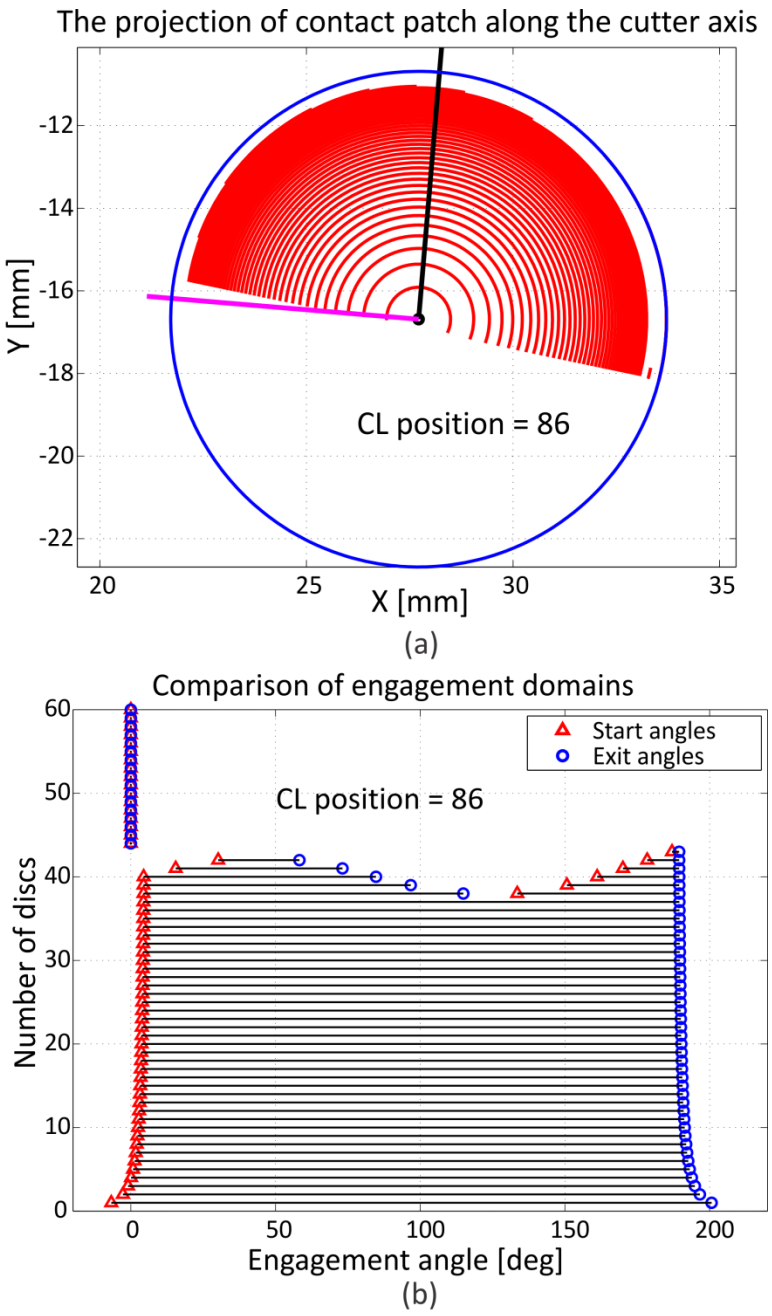

Figure 4.7: The engagement domain for CL point #86: (a) Projected view of contact patch along cutter axis, (b) Start and exit angles for the discs along the cutter axis.

There are many tool instances where the engagement domain has more than two pieces for this impeller surface example. The engagement domain for CL point #86 is shown in Figure 4.7.

4.3 Calculation of Cutter-Workpiece Engagement using Depth Buffers

There are several discrete methods used for the representation of the in process workpiece such as Octree, Voxel, ray representation and Depth buffer (Dexel) approaches.

Main advantage of discrete approaches is that they are computationally simpler than the solid modeling approach. Typically, discrete methods require intersection calculations between simple geometric primitives, allowing simple and robust analytical or algebraic solutions. This simplicity provides robust behavior, and also increases the computational efficiency.

Discrete representation of the geometry may result in the loss of geometric accuracy. However, if the simulation parameters are selected properly, considering both workpiece and toolpath tolerances, the error introduced by the discrete representation may be kept in an acceptable level.

In Octree and Voxel approach, workpiece is modeled as volume cells (Voxels), for instance cubes for the Octree data structure. Octree method is based on the divide-and-conquer principle that recursively subdivides a cube into octants up to specified resolution. Coordinates of each vertex (node) in a voxel is stored and by checking the inner-outer nodes stock workpiece is obtained. During NC simulation tool swept volume between two CL points is subtracted from the stock workpiece and machined workpiece is obtained. This method is simple and fast however, main drawback is the excessive memory requirements (especially at high resolutions) due to the large amount of data stored.

The most popular and commonly used Depth Buffer scheme in the literature and in the CAM software is Z-Buffer method. Z-buffer method is usually referred as Z-map method.

In conventional Z-map method [48], workpiece is represented as the intersection points of the Z direction vectors (ZDV) with the workpiece surface on a 2-D grid of ZDVs. These intersection points are also upmost part of the workpiece surface where only one intersection of the workpiece with a ZDV is permitted.

In 5-axis machining, conventional representation is not sufficient because almost all of the parts have walls with negative inclination angle and undercut machining is required. Hence, for 5-axis machining NC simulation extended Z-map approach is utilized. In extended Z-map approach, for one ZDV, multiple intersections and gap elements between the intersection points can also be stored most of the time using linked list data structure. Conventional and extended Z-map approaches are shown schematically in Figure 4.8.

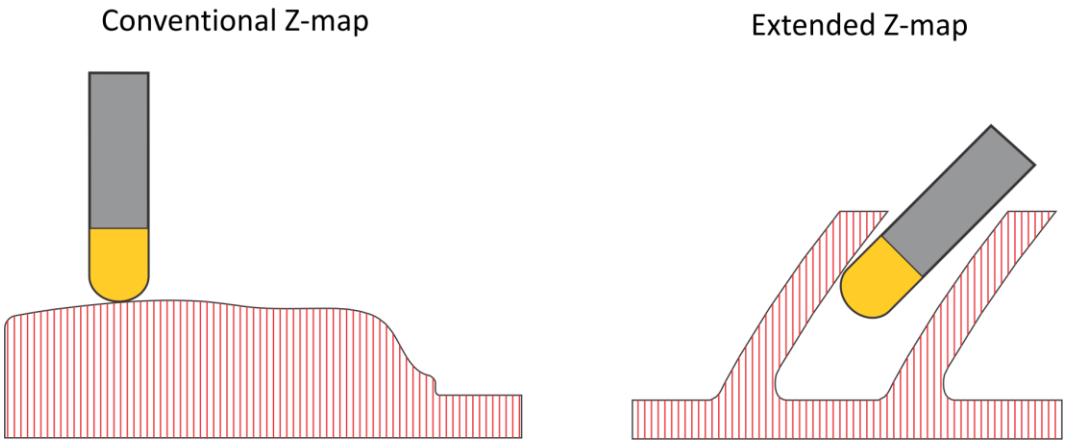

Figure 4.8: In process workpiece representations

Material removal simulation in extended Z-map approach is performed through calculation of intersections between ZDVs and the geometric representation of the tool swept volume (envelope). Resulting intersection points are compared to previously machined surface and updated for each tool movement along the toolpath.

4.3.1 Three-Orthogonal Dexelfield (Depth Buffer)

In this thesis, a commercial NC verification kernel from ModuleWorks [49] is used for machining simulation in order to obtain the contact patch between the tool and the workpiece. This verification kernel provides the use of three-orthogonal dexelfield which is similar to extended Z-map approach however the depth buffer is applied in three orthogonal directions. In other words, three-orthogonal dexelfield approach utilizes Z-map, Y-map and X-map simultaneously.

The use of three-orthogonal dexelfield is quite critical since in extended Z-map approach engagement region may not be obtained accurately due to the perpendicular intersection regions of the tool with the ZDVs. Therefore, in these regions contact patch is truncated from the actual contact patch even if the verification resolution is high. Moreover, contact catch may be obtained more accurately at lower resolutions. In Figure 4.9 and Figure 4.10, example tool position and corresponding three-orthogonal dexelfield obtained from the intersection points are shown respectively.

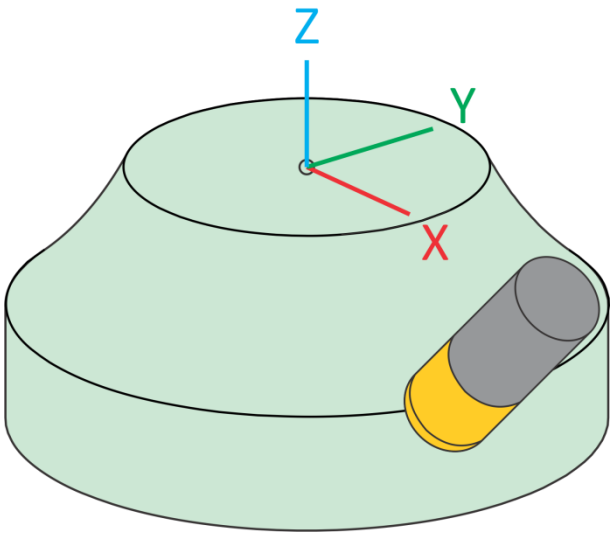

Figure 4.9: Example tool position

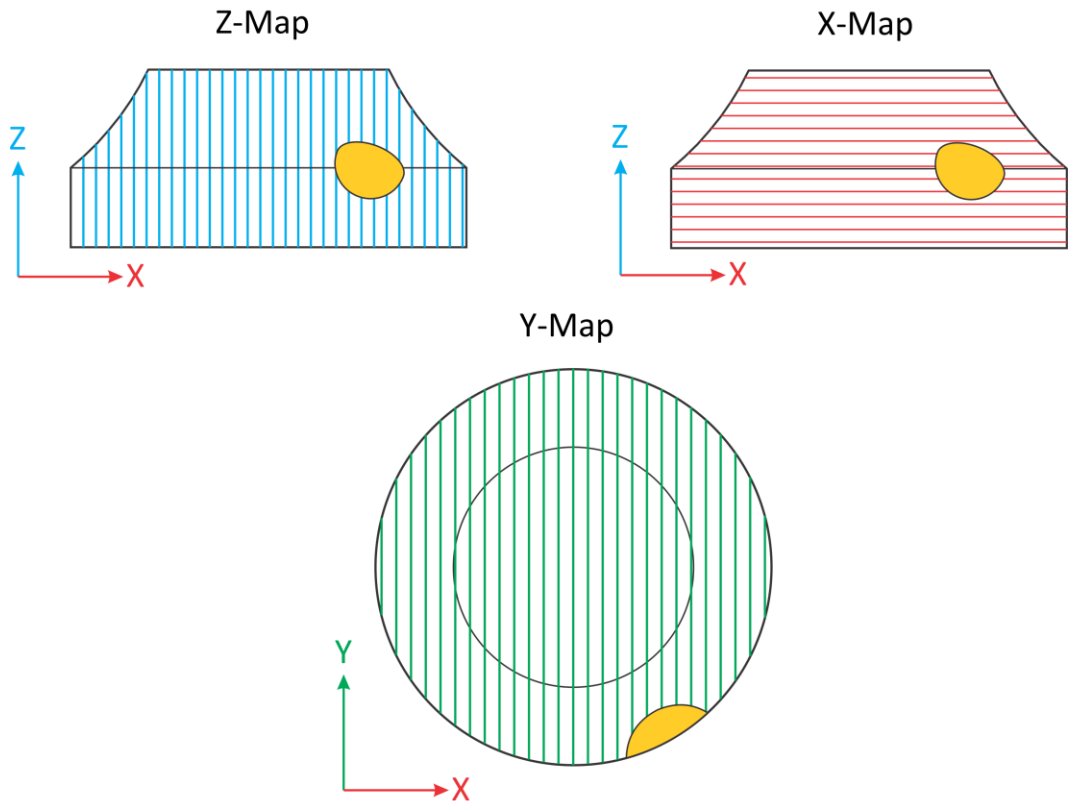

Figure 4.10: Illustration of three-orthogonal dexelfield

4.3.2 Cutting Result Entry Elements

In the previous chapter it is stated that, material removal is calculated by intersecting the tool swept envelope with the workpiece. For a given tool movement, if tool swept volume intersects with the workpiece (material removal occurs) cutting result elements are generated in three-orthogonal directions. In 5-axis machining, for an individual dexel element multiple intersections with the tool may occur due to tool axis rotation. For this reason, it has to be determined that whether the intersection point belongs to a point of the initial material-surface or to a point of the material-surface, after the cut was conducted. In

this respect, cutting result entry elements are defined using a height value distribution method. Cutting result entry height value distribution is illustrated in Figure 4.11.

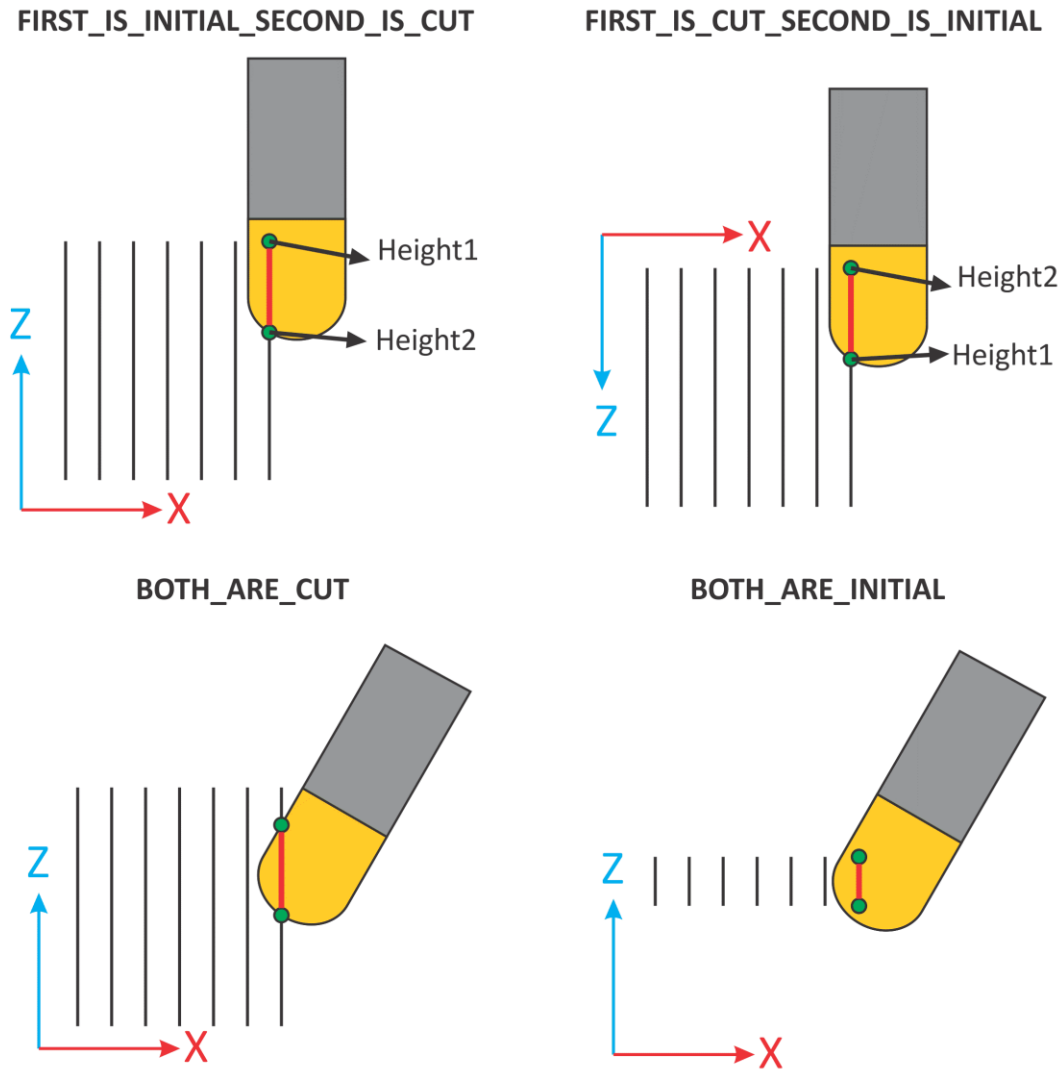

Figure 4.11: Cutting result entry height value distribution

As it is illustrated in Figure 4.11, there are four possible cases for a cutting result entry element which can be given as; FIRST_IS_INITIAL_SECOND_IS_CUT, FIRST_IS_CUT_SECOND_IS_INITIAL, BOTH_ARE_CUT and BOTH_ARE_INITIAL.

Height1 and Height2 fields represent the possible intersection points of the tool with the workpiece where Height1 is the upper intersection and Height2 is the lower intersection point. According to this distribution each cutting result entry is processed and “CUT” points are collected into a vector for the candidate contact patch points.

Another important property regarding the cutting result entry is transformation information with respect to workpiece coordinate frame. For the given example on the Z-map, the indices of the dexel block on the X-Y grid is stored internally and used for obtaining the cut point coordinates.

4.3.3 Calculation of Engagement Domain from Contact Patch (Points)

4.3.3.1 Coordinate Frames and Movement Vectors

Once contact region between the tool swept envelope and workpiece is obtained they are transformed (translated) from the workpiece coordinate frame to the tool tip of the cutter as shown in Figure 4.12.

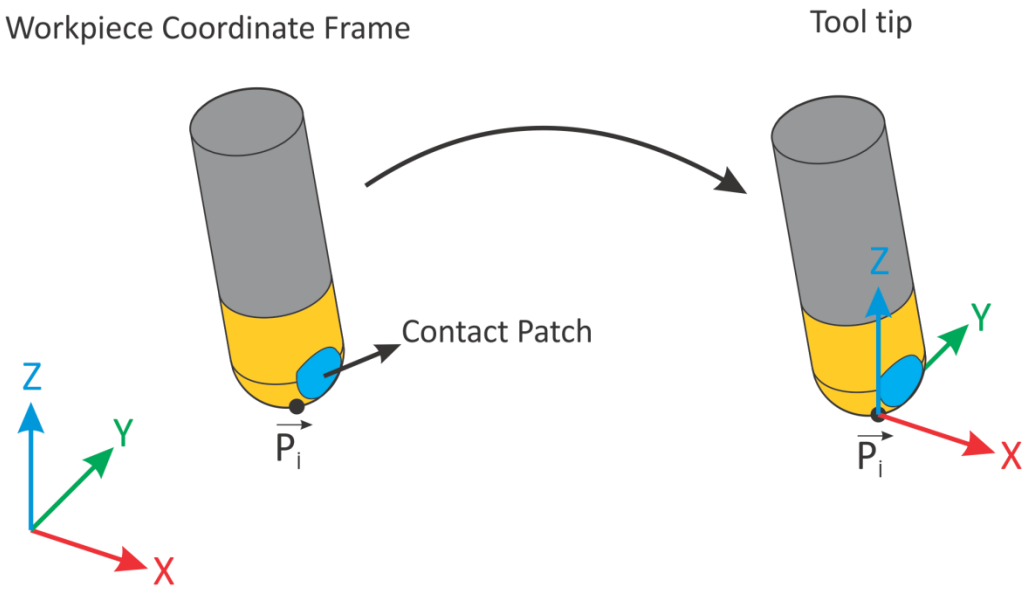

Figure 4.12: Transformation from workpiece coordinate frame to tool tip

In Figure 4.12, $\vec{P_i}$ represents the coordinates of the ith CL point in the toolpath in the workpiece coordinate frame. Contact patch is the surface obtained by combining all of the intersection points and is transformed into tool tip origin as,

$$\overrightarrow{CV} = \overrightarrow{CP} - \vec{P_i} \tag{4.1}$$

Where $\overrightarrow{CV}$ is cut vector in the tooltip origin and $\overrightarrow{CP}$ is the cut point in workpiece coordinate frame.

After the transformation given in Equation (4.1) is applied, basis of the tool movement vector, feed vector and feed coordinate frame is defined. Consider two consecutive 5-axis tool movements shown in Figure 4.13, where tool is first moving from (i-1)th CL point to the ith CL point then to the (i+1)th CL point.

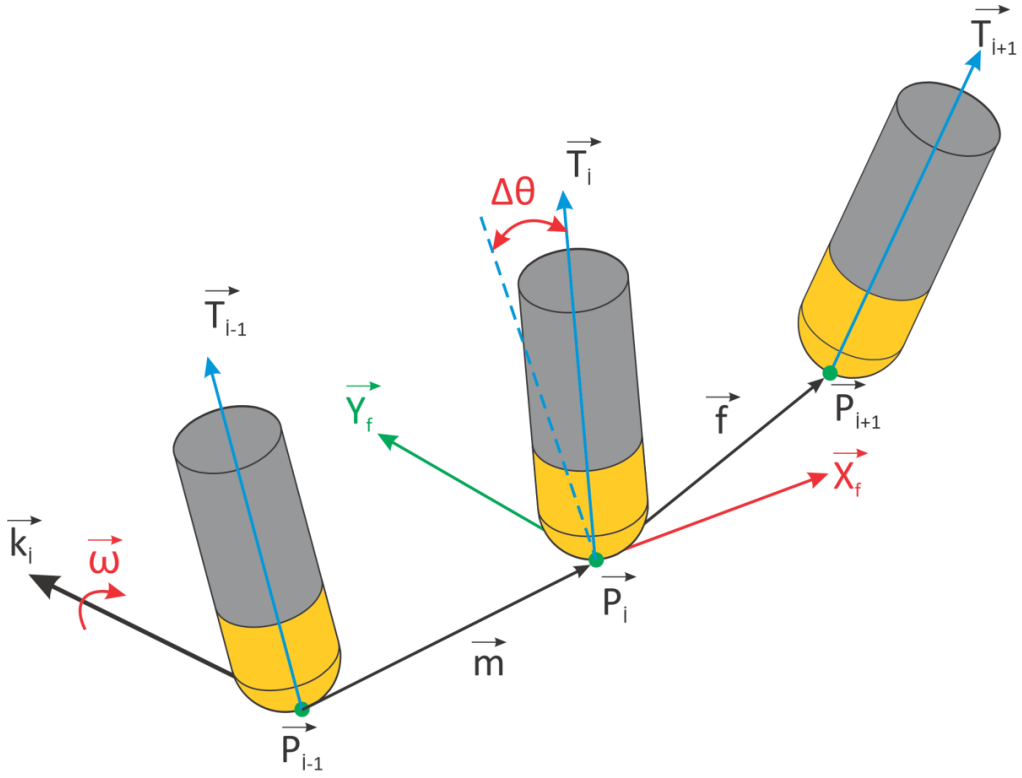

Figure 4.13: Basis of the tool movement vector, feed vector and feed coordinate frame

For determining the engagement domain for the i[th] CL point, tool swept volume from the (i-1)[th] CL point to the i[th] CL point has to be calculated. Therefore tool movement vector is defined as,

$$\vec{m} = (\vec{P_i} - \vec{P}_{i-1}) / \left\| \vec{P_i} - \vec{P}_{i-1} \right\| \tag{4.2}$$

In 5-axis machining tool can rotate as well as translate. Therefore, during translation tool axis rotates from $\vec{T}_{i-1}$ to $\vec{T}_i$ around an arbitrary axis $\vec{k}_i$ an amount of $\Delta\varphi$ where rotation axis is both orthogonal to $\vec{T}_{i-1}$ and $\vec{T}_i$. Rotation axis $\vec{k}_i$ and rotation angle $\Delta\varphi$ are calculated as,

$$\vec{k}_i = \frac{\vec{T}_{i-1} \times \vec{T}_i}{\left\| \vec{T}_{i-1} \times \vec{T}_i \right\|} \tag{4.3}$$

$$\Delta\varphi = atan2\left(\frac{\left\| \vec{T}_{i-1} \times \vec{T}_i \right\|}{\vec{T}_{i-1} \cdot \vec{T}_i} \right)$$

Cutting force model use the engagement domain for the i[th] CL point while cutting tool is moving from the i[th] CL point to (i+1)[th] CL point assuming that in this toolpath segment cutting forces are the same until tool arrives to (i+1)[th] CL point. In this respect, feed coordinate frame is constructed by using these CL points. Feed vector $\vec{f}$ can be expressed as,

$$\vec{f} = \left(\vec{P}_{i+1} - \vec{P}_i \right) / \left\| \vec{P}_{i+1} - \vec{P}_i \right\| \tag{4.4}$$

Another important property regarding feed coordinate frame is that, the feed direction and the cross feed direction denoted as $\vec{X}_f$ and $\vec{Y}_f$ respectively have to lie in a plane where the normal of this plane is $\vec{T}_i$. In other words, an orthogonal basis is defined using tool axis vector $\vec{T}_i$ and feed vector $\vec{f}$,

$$\vec{Y}_f = \vec{T}_i \times \vec{f} \tag{4.5}$$

$$\vec{X}_f = \vec{Y}_f \times \vec{T}_i \tag{4.6}$$

Here it is necessary to remind that Z axis of the feed coordinate frame $\vec{Z}_f$ is coincident with the tool axis orientation $\vec{T}_i$ at cutter location *i*.

4.3.3.2 Tool Swept Volume (Envelope)

NC verification kernel gives all of the cut points while tool is moving from one CL point to the other CL point. This yields that cut points have to be trimmed before the engagement region is determined. Schematic illustration of a ball-end mill sweep is shown in Figure 4.14.

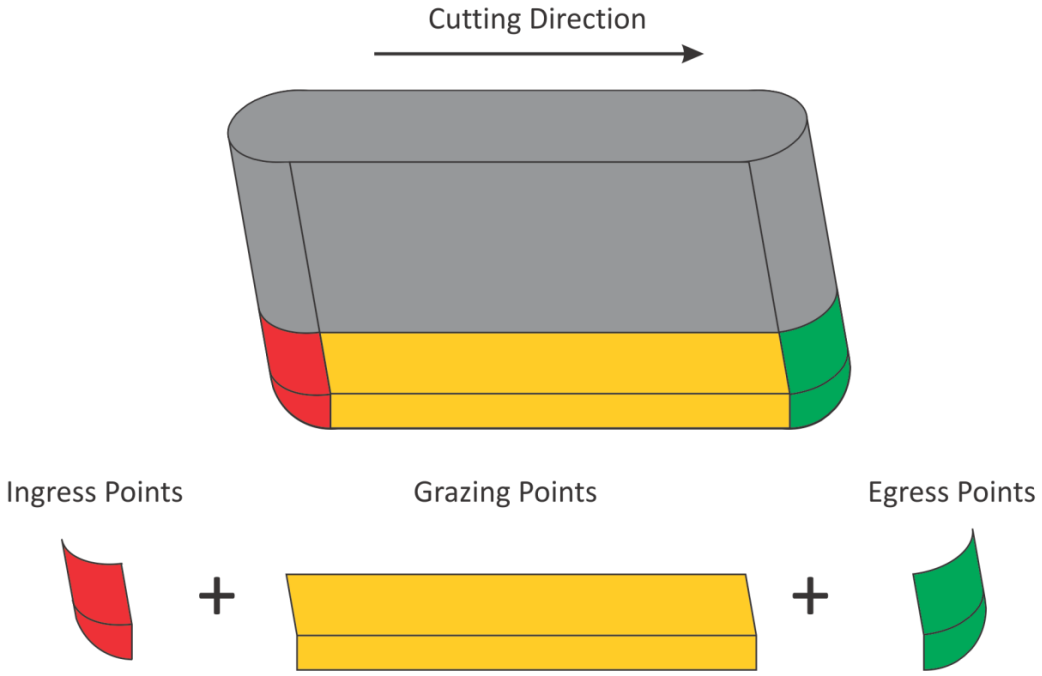

Figure 4.14: Tool swept volume of a ball-end mill.

As shown in Figure 4.14 tool swept volume of a ball-end cutter comprises three regions which are Egress points, Ingress points and Grazing points region. While obtaining the

swept volume most important parameter is cutting direction since it determines the grazing points together with the geometric properties of the cutter. Simply, egress points represent the front side, ingress points represents back side and grazing points represents the swept envelope of the cutter with respect to cutting direction. Hence, possible engagement domain of the cutter lies in the egress points region meaning that front side of the tool swept volume.

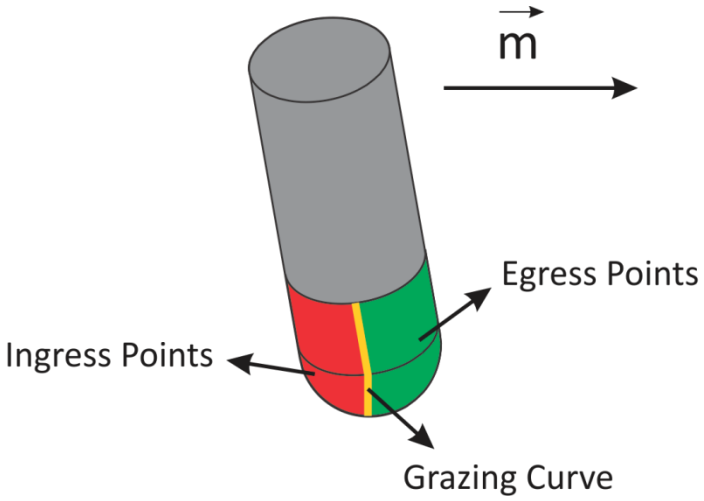

Figure 4.15: Illustration of swept regions on a ball-end mill

According to solid sweep theory [50], [51], three regions shown in Figure 4.15 can be obtained as follows,

$$\begin{aligned} \vec{n} \cdot \vec{m} > 0 \quad & \textit{Egress points} \\ \vec{n} \cdot \vec{m} = 0 \quad & \textit{Grazing Curve (points)} \\ \vec{n} \cdot \vec{m} < 0 \quad & \textit{Ingress points} \end{aligned} \tag{4.7}$$

where $\vec{n}$ is the surface normal of an arbitrary point on the cutter surface and $\vec{m}$ is the movement vector given in Eq. (4.2).

Tool motion in 5-axis machining also includes an arbitrary rotation and this effect must be taken into account if swept volume of the cylinder part of the cutter is in cut, on the other hand in free-form surface machining distance and angular rotation between is relatively small, therefore instead of applying exact 5-axis tool motion swept volume is modeled assuming 3+2 axis tool motion.

4.3.3.3 Surface Normals for a Ball-end Mill

Surface normal of a general milling cutter can be expressed analytically [51], however, in this study tool swept volume is not directly calculated. Primary aim of the swept volume modeling is to identify the cut points which are in the egress region. Therefore, surface normals are found geometrically.

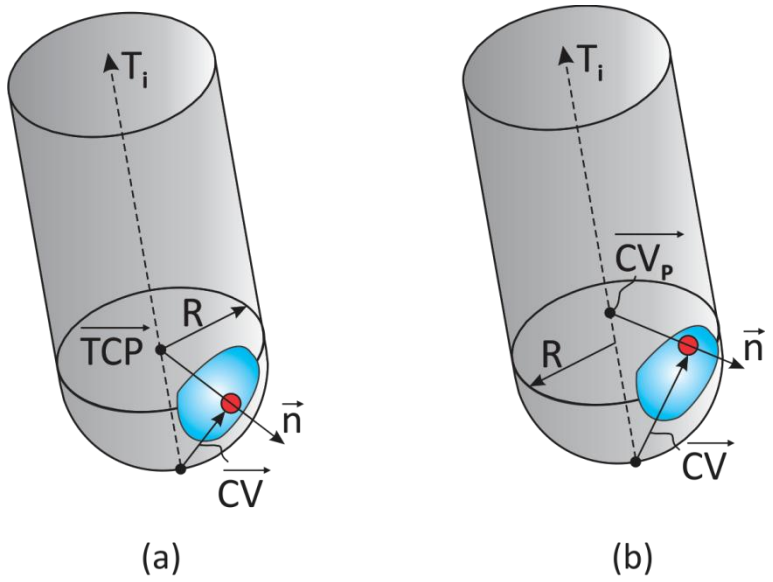

Figure 4.16: Surface normal calculation: (a) Sphere part, (b) Cylinder part

Figure 4.16 shows the calculation principle of the surface normals for a ball-end mill. Surface normal for the sphere part can be found as,

$$\overrightarrow{TCP} = R.\vec{T}_i$$

$$\vec{n} = \frac{\overrightarrow{CV} - \overrightarrow{TCP}}{\left\|\overrightarrow{CV} - \overrightarrow{TCP}\right\|} \tag{4.8}$$

where $\overrightarrow{TCP}$ is the tool center point, R is the radius to the cutting tool, $\vec{T}_i$ is tool axis vector for the CL point i and $\overrightarrow{CV}$ is the cut vector given in Equation (4.1).

Surface normal calculation for the cylinder part is quite different from the sphere part since cylinder part is not symmetric around tool center point. For this reason, first $\overrightarrow{CV}$ is projected on to the tool axis in order to determine the axial height from the tooltip, then surface normal is found.

$$\overrightarrow{CV_p} = \left(\overrightarrow{CV} \cdot \vec{T}_i\right).\vec{T}_i$$

$$\vec{n} = \frac{\overrightarrow{CV} - \overrightarrow{CV_p}}{\left\|\overrightarrow{CV} - \overrightarrow{CV_p}\right\|} \tag{4.9}$$

Before calculating the tool surface normal, each point has to be verified that the point is on the sphere part or on the cylinder part. If $\left\|\overrightarrow{CV_p}\right\| < R$, point belongs to sphere surface otherwise it belongs to the cylinder surface.

4.3.3.4 Calculation of Engagement Angles

In order to determine the engagement angle, cut vector is first projected onto $\vec{X}_f - \vec{Y}_f$ plane as follows,

$$\overrightarrow{CV_{xy}} = \left(\vec{T}_i \times \overrightarrow{CV}\right) \times \vec{T}_i \tag{4.10}$$

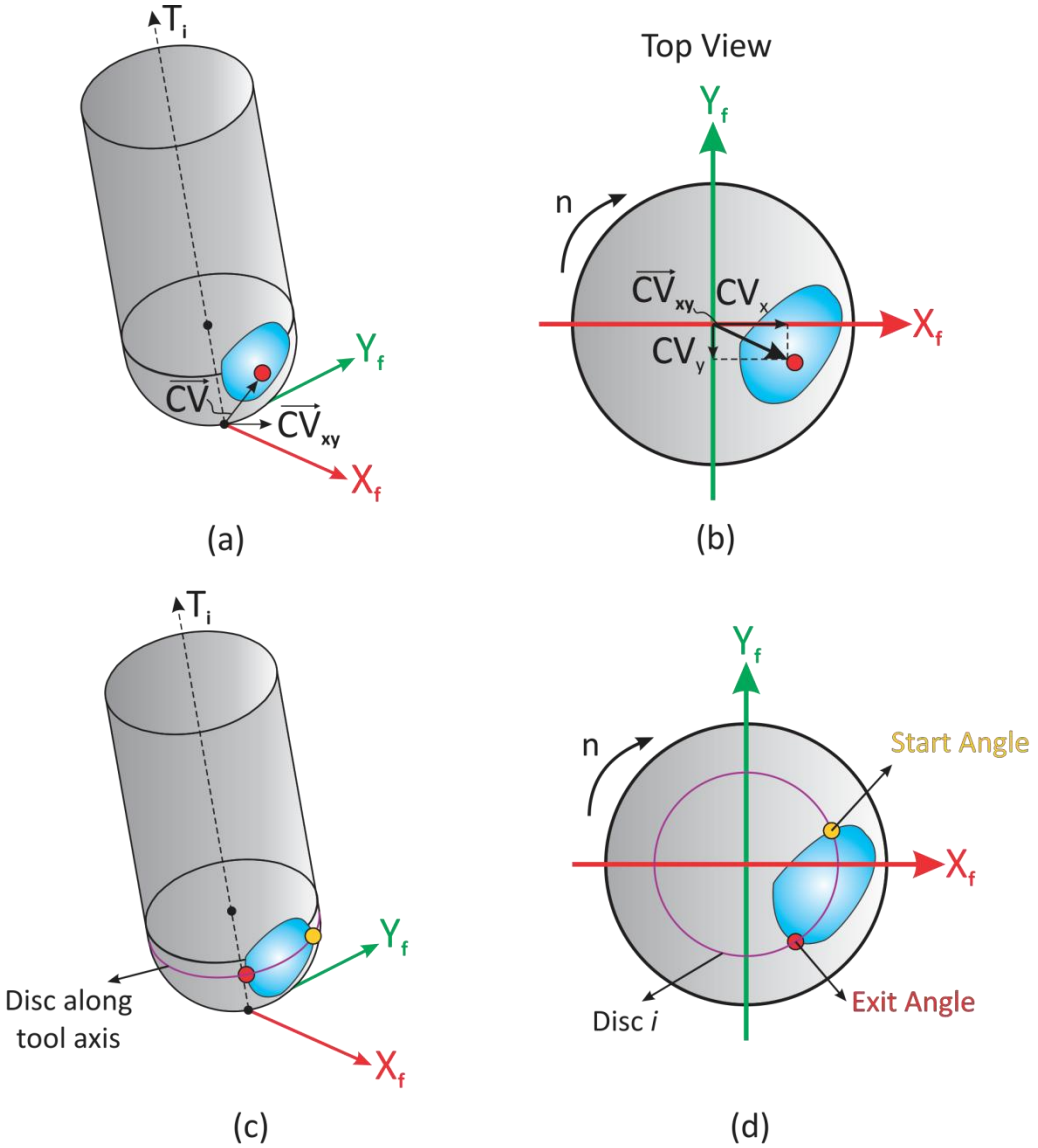

Figure 4.17: Engagement angle calculation: (a) Projection on $\vec{X}_f - \vec{Y}_f$ plane, (b) Projection on feed and cross feed directions, (c)-(d) Start and exit angles

Final step is necessary for determining the engagement angles by projecting $\overrightarrow{CV}_{xy}$ vector onto feed and cross feed direction, then angles are calculated using arctangent function.

$$CV_x = \overrightarrow{CV_{xy}} \cdot \vec{X}_f$$
$$CV_y = \overrightarrow{CV_{xy}} \cdot \vec{Y}_f \tag{4.11}$$
$$\theta_e = atan2(CV_x, CV_y)$$

where $atan2$ is a four quadrant arctangent function.

Since engagement angles are defined in clockwise direction, in Equation (4.11) the order of the X and Y components of the projected cut vector is reversed.

4.3.3.5 Determination of Engagement Quadrants

Start and exit angles of the engagement domain can be identified correctly by checking the quadrant of the engagement angle. The method for the quadrant determination can be given as follows,

$$\begin{aligned} CV_x > 0, \quad CV_y > 0 \Rightarrow Quadrant\ I \\ CV_x > 0, \quad CV_y < 0 \Rightarrow Quadrant\ II \\ CV_x < 0, \quad CV_y < 0 \Rightarrow Quadrant\ III \\ CV_x < 0, \quad CV_y > 0 \Rightarrow Quadrant\ IV \end{aligned} \tag{4.12}$$

In 3-axis machining engagement region is determined only by the tool movement direction since tool axis direction is fixed in vertical or horizontal direction. In contrary, tool orientation for 5 axis tool motion changes spatially, therefore possible engagement region is related to move direction and tool axis orientation. If $\vec{T}_i \cdot \vec{m} > 0$, $Quadrant\ I$ and $Quadrant\ II$ is valid. If $\vec{T}_i \cdot \vec{m} < 0$, $Quadrant\ I$, $Quadrant\ II$, $Quadrant\ III$ and $Quadrant\ IV$ is valid. The method explained above is illustrated in Figure 4.18.

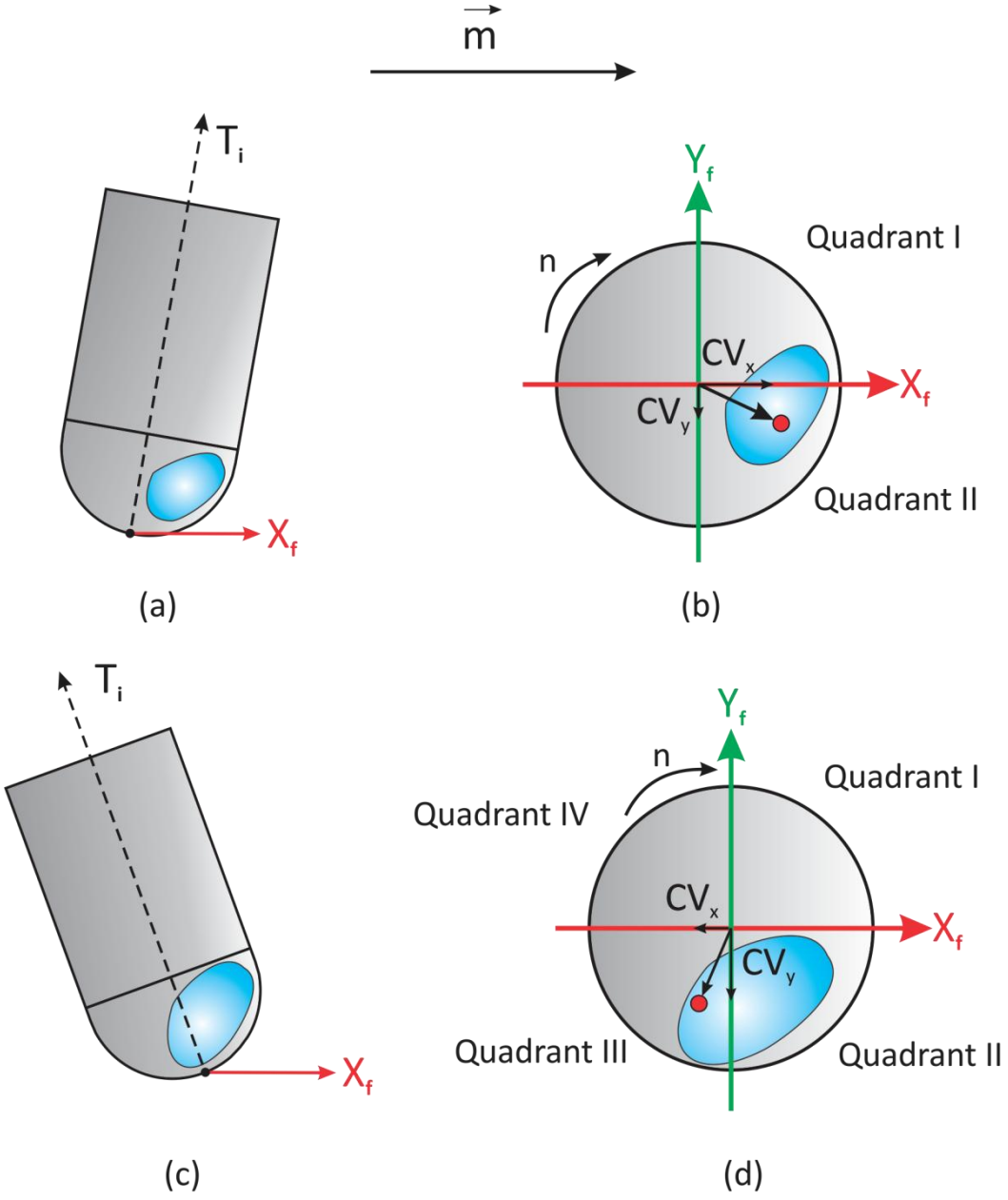

Figure 4.18: Engagement quadrant determination: (a) Tool move for $\vec{T}_i \cdot \vec{m} > 0$, (b) Valid engagement regions for $\vec{T}_i \cdot \vec{m} > 0$, (c) Tool move for $\vec{T}_i \cdot \vec{m} < 0$, (d) Valid engagement regions for $\vec{T}_i \cdot \vec{m} < 0$

4.3.3.6 Engagement Domain Results

Three-orthogonal dexelfield approach explained in Chapter 4.3.3 is implemented in Microsoft Visual Studio using C++ programming language. For the verification, impeller roughing toolpath shown in Figure 4.4 is simulated with the three-orthogonal dexelfield approach. In simulation, resolution (grid distance between discrete direction vectors or dexel blocks) is selected to be 0.1 mm and tool is divided into 60 discrete discs. Computation time for the simulation is 4 minutes and 57 seconds on a Windows 7 64-bit, Core2Duo 3.16 GHz / 8GB ram desktop PC. Simulated machined workpiece is shown in Figure 4.19.

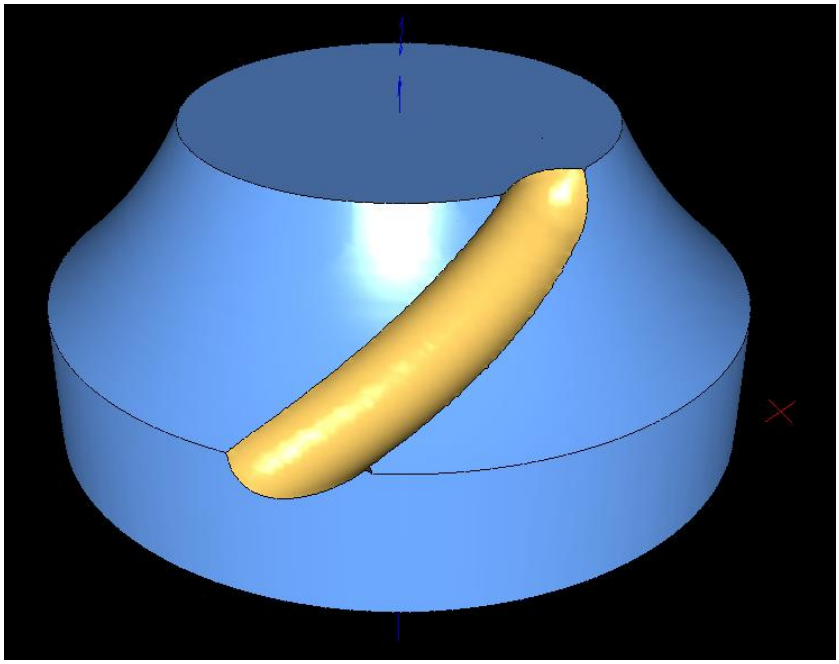

Figure 4.19: Machined workpiece using three-orthogonal dexelfield approach

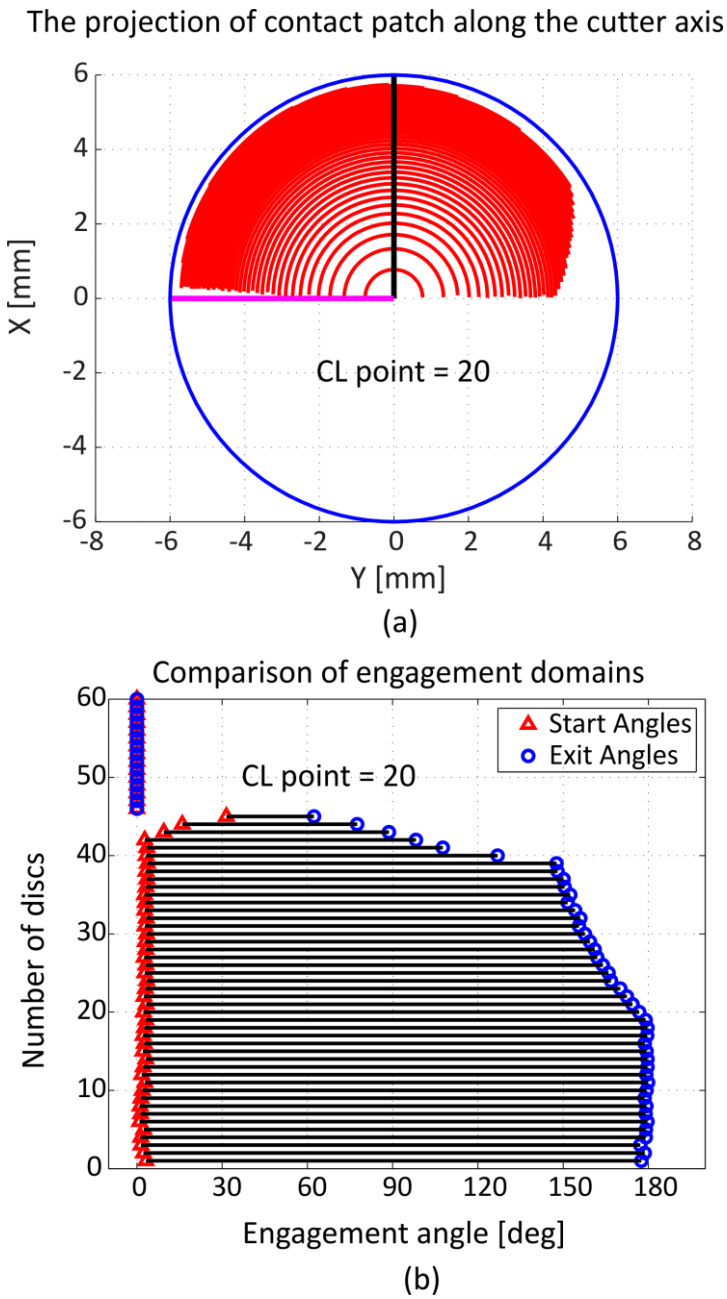

Figure 4.20: Three-orthogonal dexelfield engagement domain for CL point #20: (a) Projected view of contact patch along cutter axis, (b) Start and exit angles for the discs along the cutter axis.

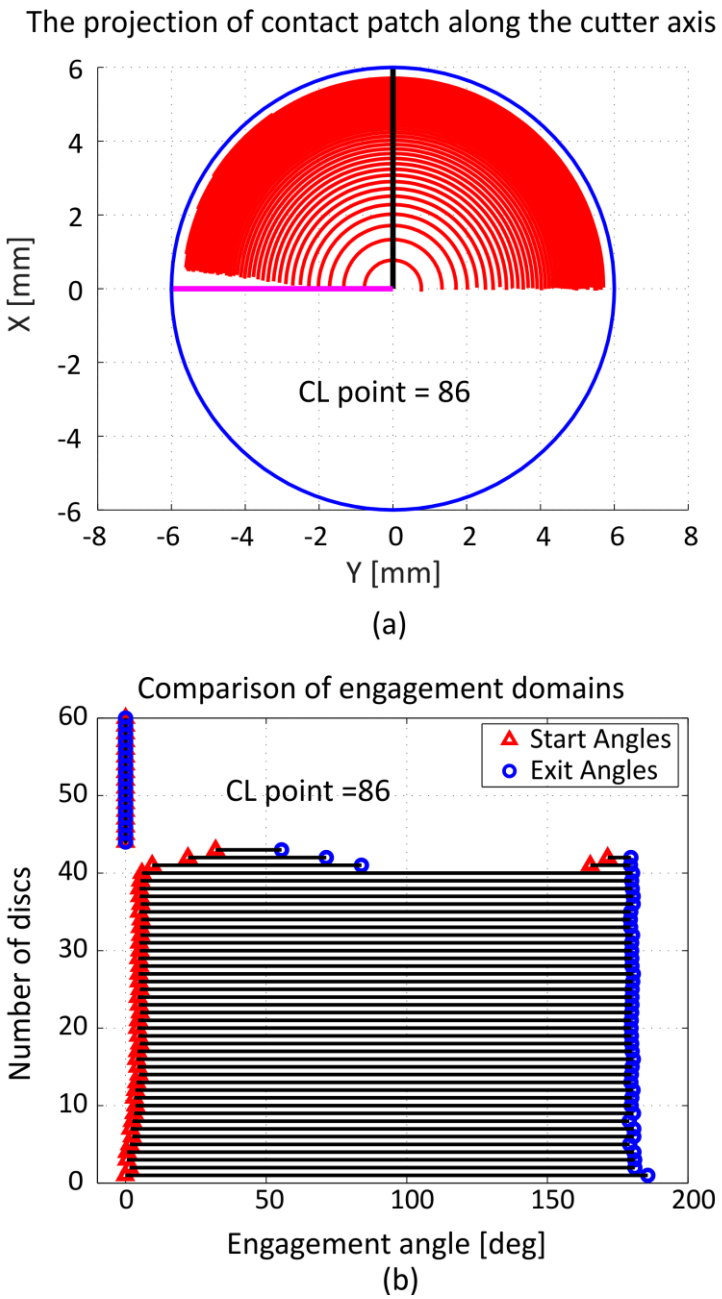

Figure 4.21: Three-orthogonal dexelfield engagement domain for CL point #86: (a) Projected view of contact patch along cutter axis, (b) Start and exit angles for the discs along the cutter axis.

In Figure 4.20 and Figure 4.21, engagement domains with their projections along the tool axis for CL point 20 and 86 are shown respectively. The engagement domain for the CL point 20 shows that the engagement region is one piece, for the CL point 86 engagement domain consists of two pieces. Multiple contact regions are obtained using the quadrant determination method explained in Chapter 4.3.3.5. This method can only determine the multiple contacts if the gap region occurs between the quadrants. If the gap region lies in one quadrant, all engagement angles have to be checked whether sudden increase or decrease occurs between consecutive engagement angles. However, this method comes with a decrease in computational efficiency since for the example CL point 86 there are 669780 intersection points in other words engagement angles. Therefore, determining the in-quadrant gap regions costs considerable amount computation time; as a result, a simplified approach is utilized for obtaining the multiple piece engagement domains along the toolpath.

4.4 Sample Results for Three-Orthogonal Dexelfield Engagement Model

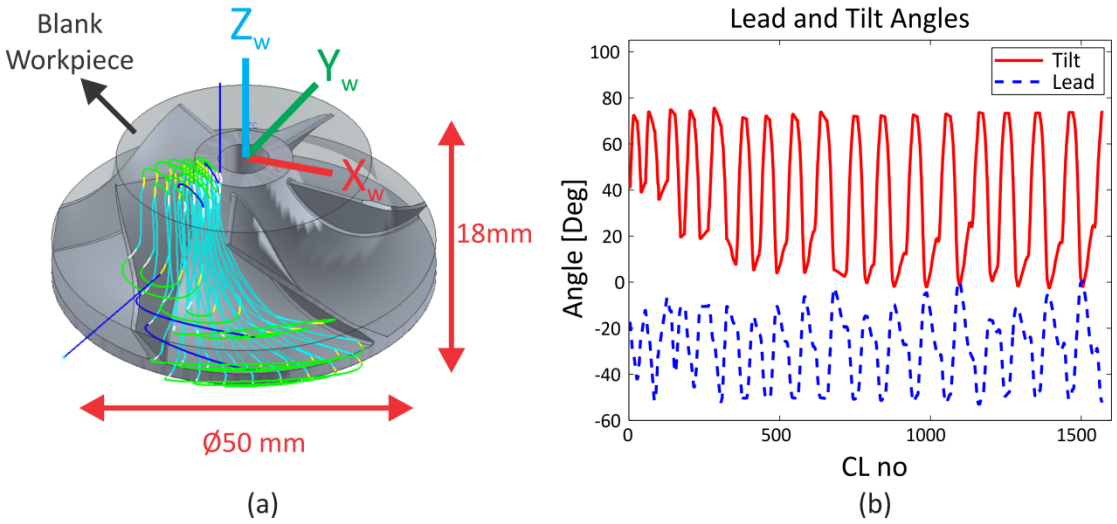

Figure 4.22: (a) Simulated Impeller Roughing toolpath, (b) Lead and tilt angles for the toolpath

Toolpath shown in Figure 4.22 which consists of 1572 CL points is simulated for the extraction of the Cutter-Workpiece Engagement maps. Force prediction results are also presented in Chapter 7.3 in detail. Impeller hub is machined using a 6 mm ball-end mill therefore in the simulation aforementioned cutting tool is selected. In order to demonstrate the complex and spatially changing engagement regions in 5-axis machining several 2D engagement maps is shown from Figure 4.23 to Figure 4.26.

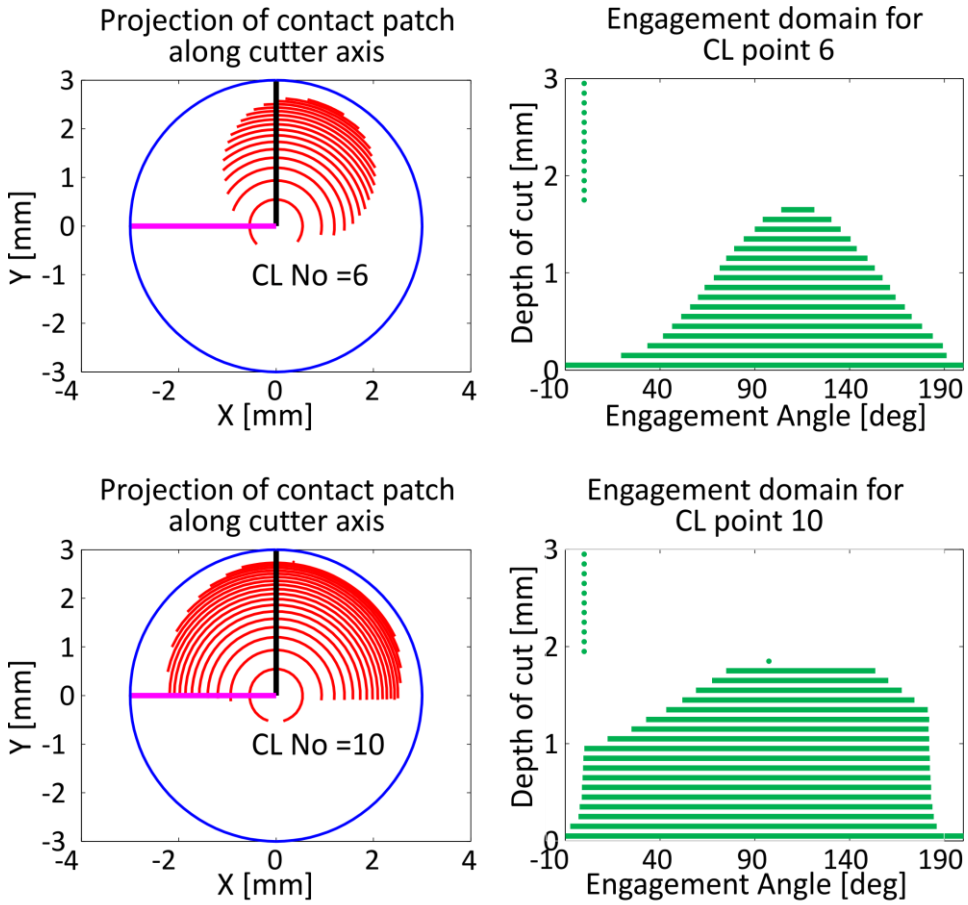

Figure 4.23: Engagement results for 6th and 10th CL points

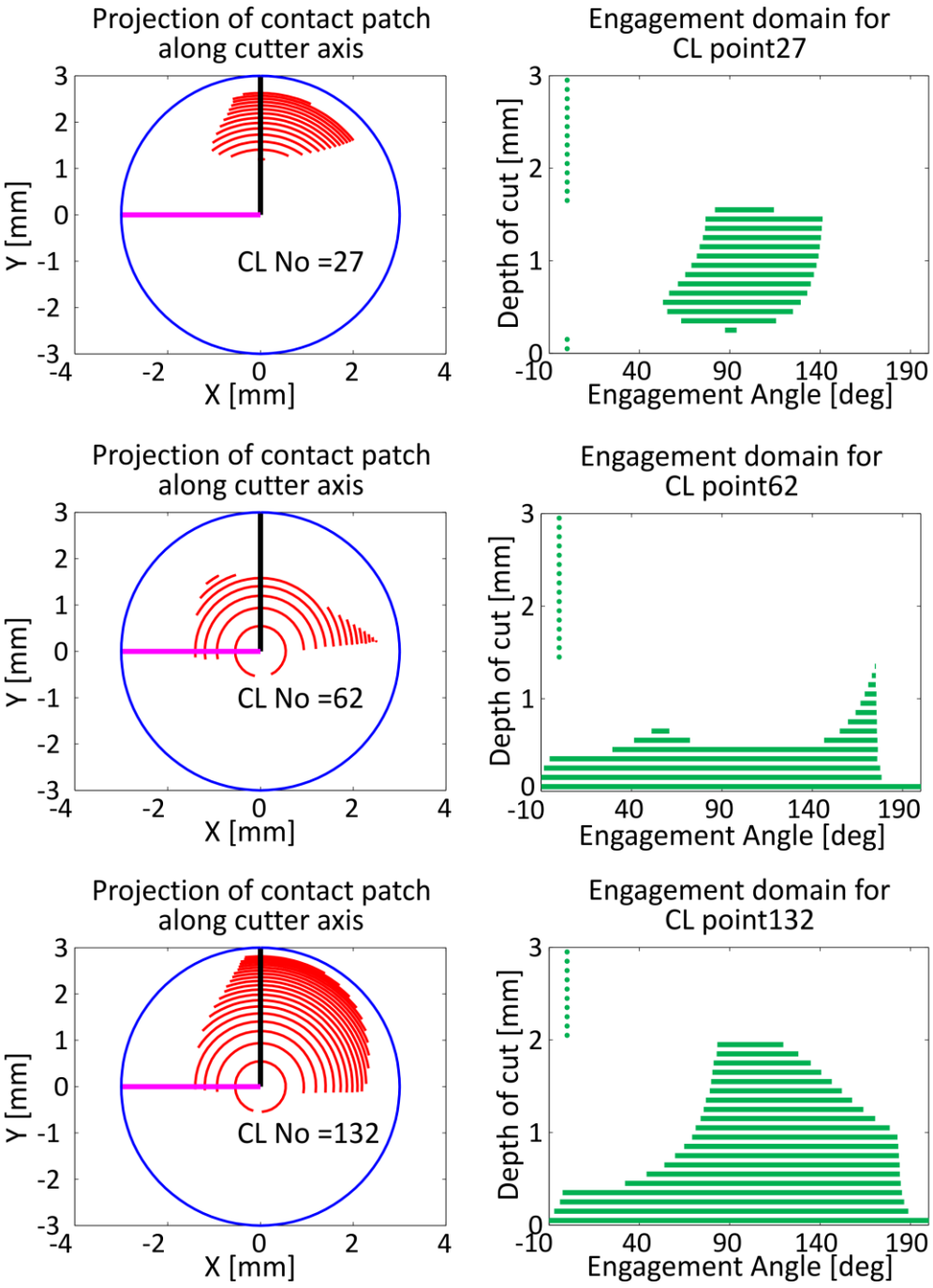

Figure 4.24: Engagement results for 27th, 62nd and 132nd CL points

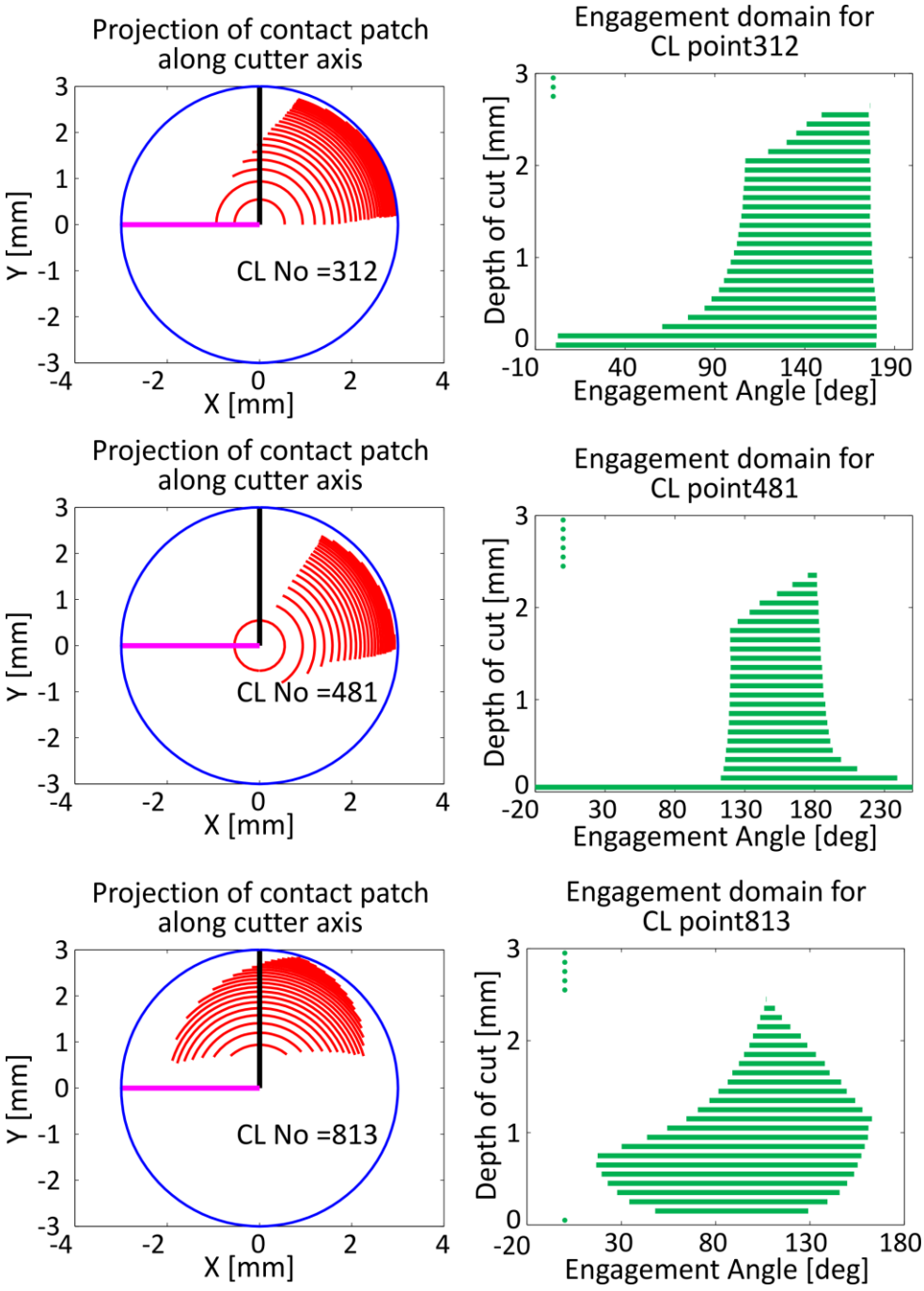

Figure 4.25: Engagement results for 312th, 481st and 813th CL points

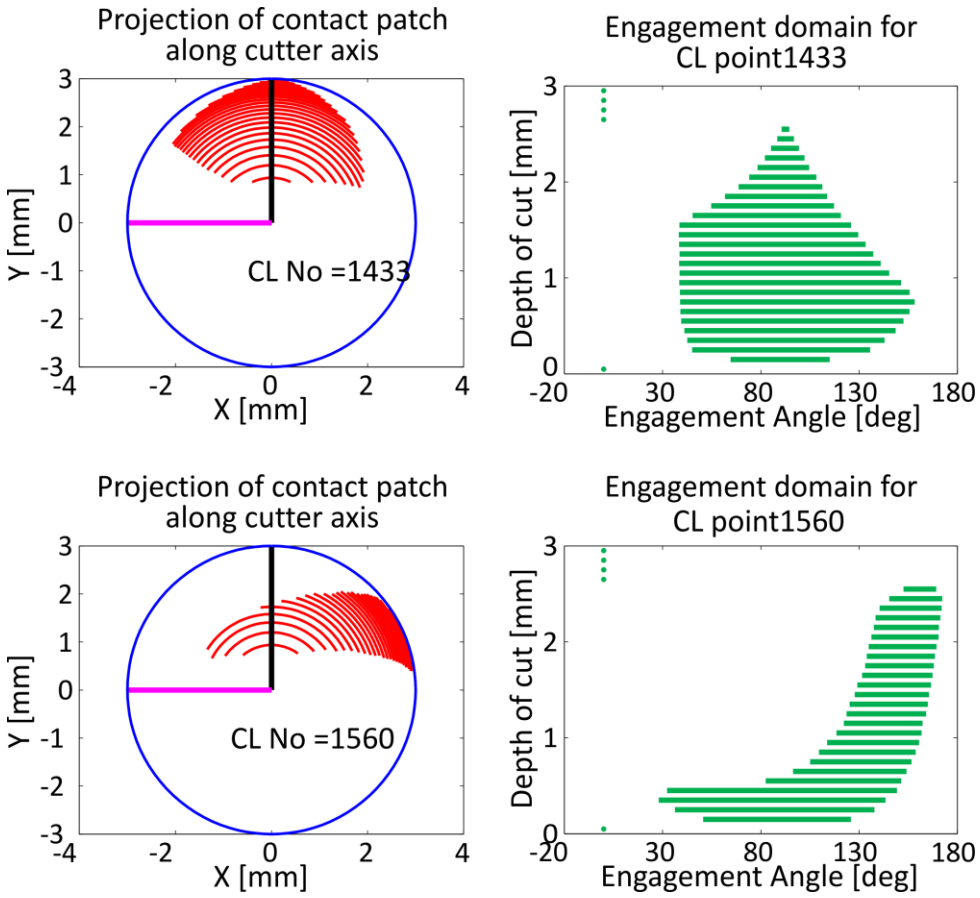

Figure 4.26: Engagement results for 1443rd and 1560th CL points

4.5 Comparison of Cutter-Workpiece Engagement Approaches

In conclusion, this thesis presents two different cutter-workpiece engagement calculation schemes. Namely, solid-modeler based and discrete vector representation (dexel, depth buffer) based cutter-workpiece methods.

The efficiency of these two methods is compared considering the computation time and the simulation accuracy. Regarding the computation time, it is demonstrated that solid-modeler based approach is approximately 4 times faster than the three-orthogonal dexelfield approach. As it is stated before, for the example impeller roughing toolpath

computation time in solid-modeler based approach is 58 seconds and for the three-orthogonal dexelfield approach computation time is 4 minutes 57 seconds.

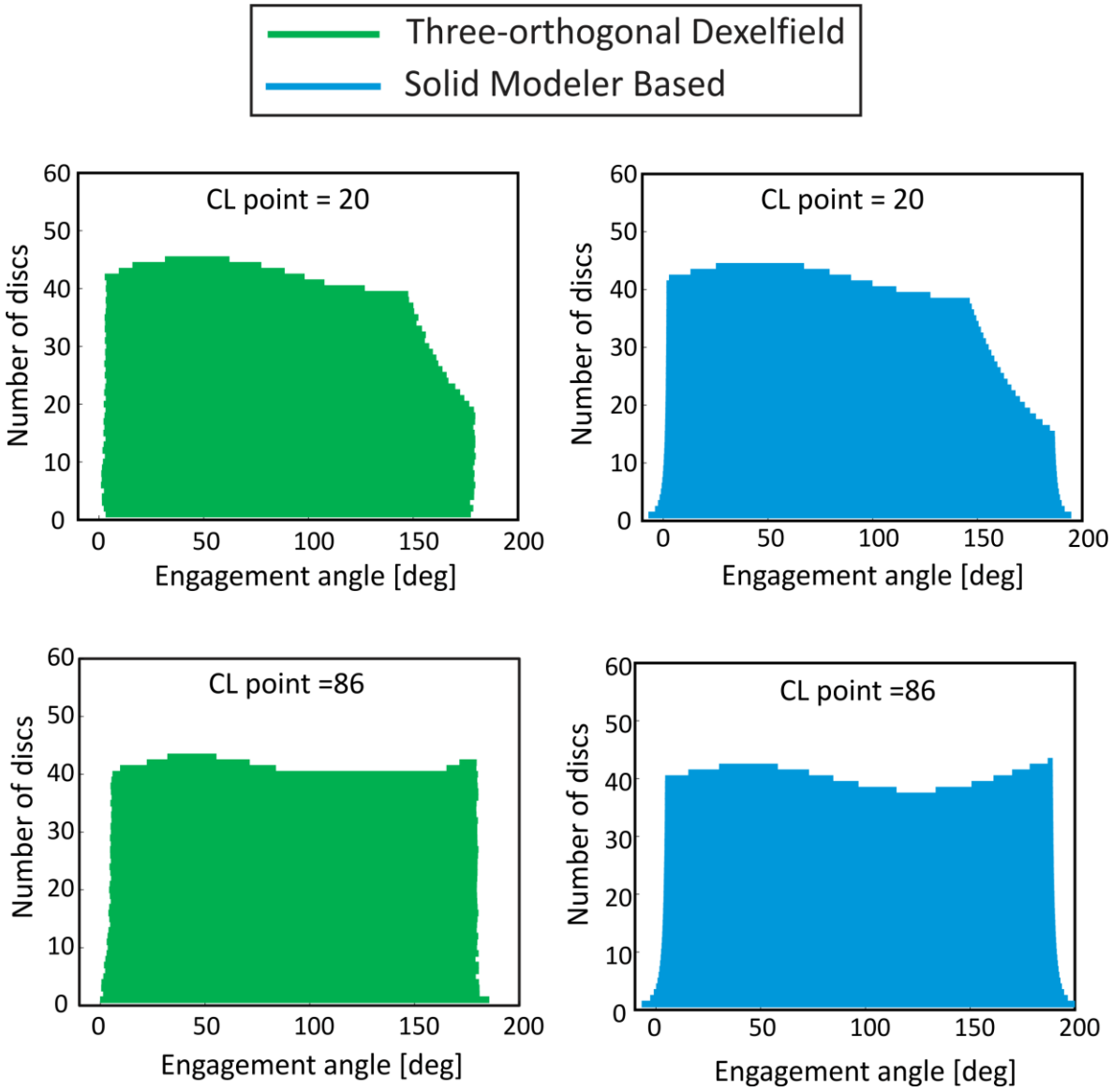

Figure 4.27: Comparison of engagement maps from the Three-orthogonal dexelfield (green) and the Solid-modeler based (blue)

This computational inefficiency of the three-orthogonal dexelfield approach arises from the use of three dexelfields simultaneously. Instead of using three dexelfields, if the conventional Z-map technique is used computation time can be reduced to approximately one third of the presented approach meanwhile losing the simulation accuracy.

Second important criteria while judging the efficiency of the cutter-workpiece engagement model is the accuracy of the model since precise determination of the engagement region is crucial for the cutting force model.

In this respect, solid-modeler based engagement model is superior to the three-orthogonal dexelfield approach. As it is illustrated in Figure 4.27 there are slight differences between two methods and it is observed that solid-modeler based approach is more accurate than the three-orthogonal dexelfield approach. Solid-modeler based approach uses exact Boolean operations between the cutter swept envelope and the workpiece, for this reason, surface patch boundaries are exact and smooth. In three-orthogonal dexelfield approach due to numerical instability and the nature of the intersections, fluctuations in the engagement angles and the trimming of the engagement region occur.

In conclusion, for five-axis milling, solid-modeler based cutter-workpiece engagement approach calculates the engagement angles more accurately and faster compared to three-orthogonal dexelfield approach. Furthermore, multiple engagement regions can be handled effortlessly and correctly whereas in three-orthogonal dexelfield approach in-quadrant contact regions are not considered, hence this may cause the incorrect interpretation of the engagement information.

Chapter 5

CALIBRATION PROCESS

5.1 Introduction

Cutting coefficient identification can be performed with two methods. First method is the orthogonal to oblique transformation [52]. In this approach transformation from orthogonal cutting to oblique cutting condition is performed. Parameters obtained from orthogonal cutting tests such as shear angle, shear stress, and friction coefficient are transformed in to oblique cutting by using geometric parameters of the cutting tool. This method is superior for simple cutting geometries since geometric parameters define the transformation. Besides, this method requires several turning test which is time consuming and costly. Therefore it is not appropriate for practical applications. Second method is the mechanistic identification of cutting force coefficients. Mechanistic calibration is performed by running a series of slot cutting tests at different feedrates for the cutting force identification. This method is less time consuming and suitable for practical applications, on the other hand this method is valid for the tool being calibrated. Tool with different geometry has to be calibrated separately for the identification of the cutting force coefficients.

In this study, Altintas's approach [52] is utilized for identification of cutting constants in milling with certain modifications which is explained in this section.

5.2 Cutting Force Coefficient Identification in Fixed Coordinate Frame

The experiments for calibration and validation are performed on Mori Seiki NMV5000 DCG 5-axis vertical machining center. The cutter is carbide ball-end mill cutter from

CoroMill Plura series of Sandvik with 12 mm diameter, 37 mm projection length and 30 degrees helix angle. The workpiece materials are aluminum blocks (Al7075) of size 250x200x40 [mm]. Kistler 3-component dynamometer (Model 9257B) and a charge amplifier are used to measure cutting forces. The 3-component dynamometer is fixed to the rotary table of the machine using clamps and the aluminum block is attached to the dynamometer using two 8M bolts as seen in Figure 5.1.

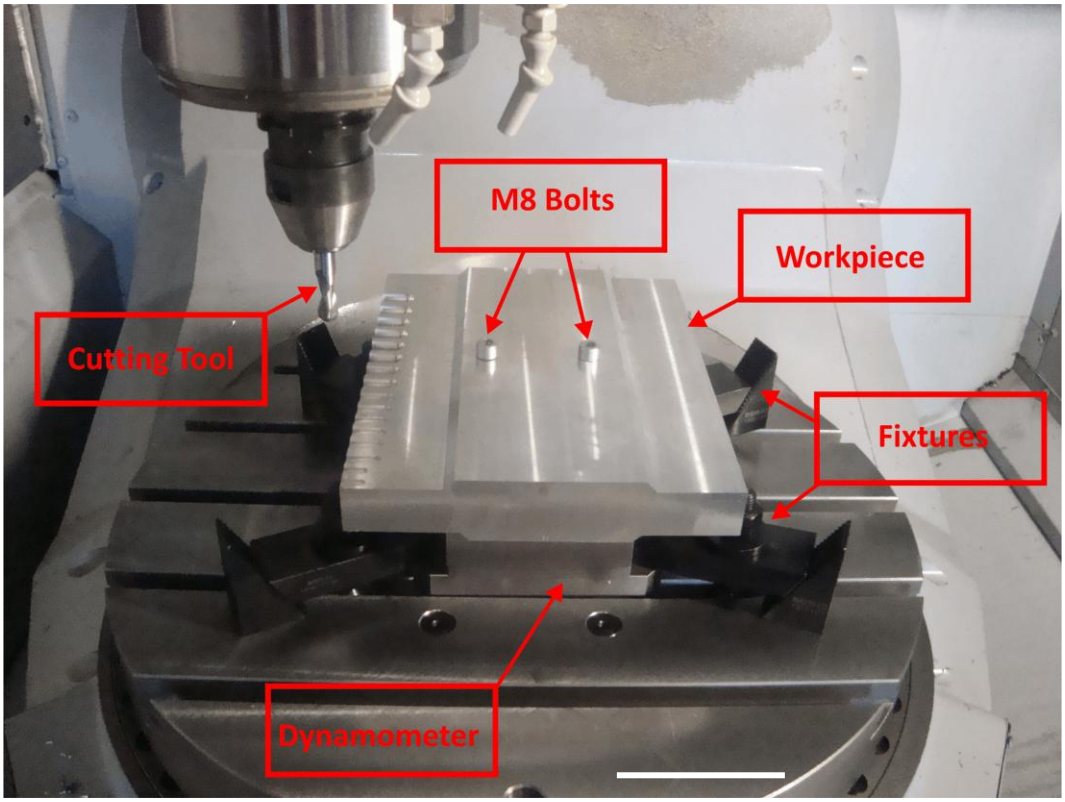

Figure 5.1: Workpiece and 3-component dynamometer fixed to VMC machine table for cutting tests

The cutting forces are sensed by the piezoelectric transducer in the dynamometer and an electric charge output is the outcome of this process. This electric charge is later taken by the charge amplifier and converted into voltage output. The sensitivity values for the three

channels (x, y and z) in the amplifier were 7.93, 7.90, and 3.69 pC/N respectively. Amplifier gain for the device was set to 300 N/V for all channels. Subsequently, through use of a proper data acquisition card with 1 MS/s sampling rate, +/-10 V analog input and software, the voltage output is displayed and recorded as cutting forces in Newton. Displaying and recording of the measured data was realized with a data acquisition program, MALDAQ module of CutPro. Schematic of experimental setup is shown in Figure 5.2.

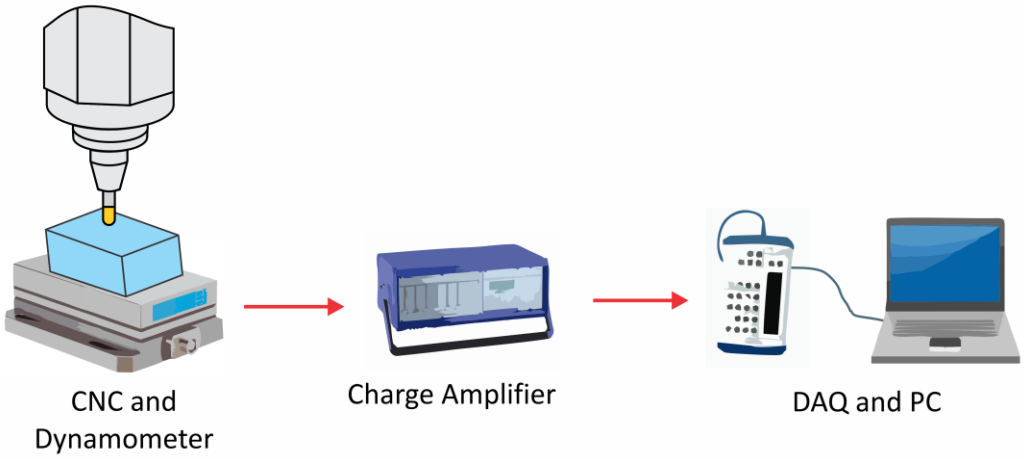

Figure 5.2: Schematic of experimental setup

First step to be taken is to obtain the cutting forces by conducting a set of milling experiments at different feedrate values. The 48-192 mm/min feedrate interval has been tested in this study. The ball part of the ball-end mill has been divided into 8 disks for a detailed analysis. Assuming the tip to be at zero level, these intervals were subsequently at 0-0.5, 0.5-1, 1-1.5, 1.5-2, 2-3, 3-4, 4-5, 5-6 mm distance from tip. Each interval has been tested for four different feedrate values; 48, 96, 144 and 192 mm/min. The collection of data is made at every discrete rotation angle $\Delta\theta$ degrees ($\Delta\theta$ is 3.6° for the system under investigation):

$$\Delta\theta = \frac{2\pi \cdot \frac{\omega}{60}}{f_s} \tag{5.1}$$

where the spindle speed (ω) was kept constant at 600 rpm. Data has been collected for 9 revolutions and with sampling frequency rate (f_s) of 1000 Hz at all tests. Two sets of experimental runs have been performed in order to increase reliability of results.

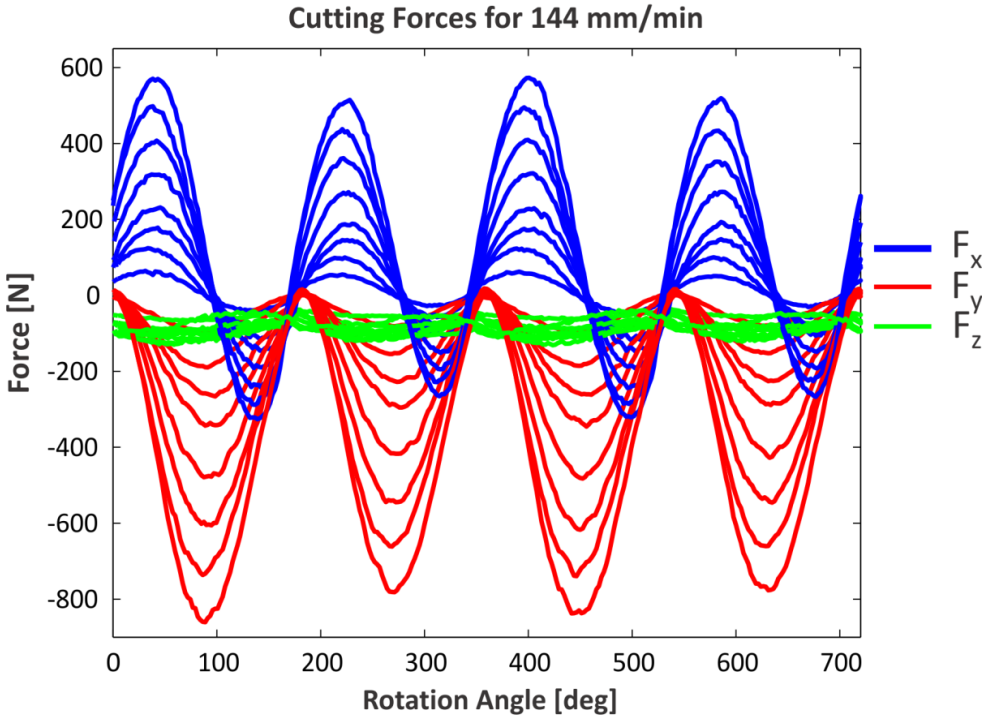

Figure 5.3: Cutting forces corresponding to chosen depth of cuts, at 144 mm/min

All the cutting forces of the first set of experiment for 144 mm/min for two revolutions can be seen in Figure 5.3. In order to obtain the cutting coefficients for a certain interval, the following procedure has been applied to all forces step by step:

1. The angular phase differences have been detected for all the collected data and by accounting for these differences all experimental force data have been equally aligned.
2. Maximum values of each tooth for all three components (X-Y-Z) of the cutting force have been found, and the averages of these peak points are taken for certain number of the revolutions in the collected data.
3. The differences between the average points have been obtained for each increment in the depth of cut (e.g., for 4-5 mm interval, cutting forces will equal the difference between 5 mm depth of cut and 4 mm depth of cut cutting forces).
4. Using the inverse transformation in Equation (6.14), collected force components which are in X-Y-Z global coordinate system have been transformed into radial, axial and tangential force components F_r, F_ψ, and F_t respectively.
5. Finally, once the F_r, F_ψ, and F_t values have been obtained for each depth of cut interval, a linear curve is fitted for these forces and chip thickness in order to obtain the cutting coefficients.
6. Once the F_r, F_ψ, F_t values have been obtained for each depth of cut interval, these values are plotted versus chip thickness in order to obtain the cutting coefficients. Two sample curve fits are shown in Figure 5.5 and Figure 5.6. The determination of cutting constants from experimental data is summarized in Figure 5.7.

As opposed to the straight-end mill, ball-end mill cutting edge geometry varies locally in the ball part. This variation is expressed with psi (ψ) angle as shown in Figure 5.4. The psi (ψ) angle is important for the depth of cut interval while obtaining the force versus chip thickness plots. This psi (ψ) angle is taken for the midpoint of depth of cut interval instead of taking the upper and lower limits of depth of cut interval.

For the z_1 –z_2 mm interval;

$$\psi = \arccos\left[\frac{R_b - (\frac{z_1 + z_2}{2})}{R_b}\right] \tag{5.2}$$

where z_1 and z_2 are measured from the tip of the sphere part and R_b is the ball radius of the cutter measured from the center of the sphere part. It is also shown in Figure 5.4.

The change in cutting coefficients along the cutting edge is displayed in Figure 5.8. It is observed in these plots that K_{tc} is the most dominant cutting coefficient. The edge coefficients, on the other hand, exhibit an almost completely random behavior; no trend can be clearly identified by observing their plot. The numerical values of the cutting coefficients determined with the calibration process can be summarized in the Table 5-1.

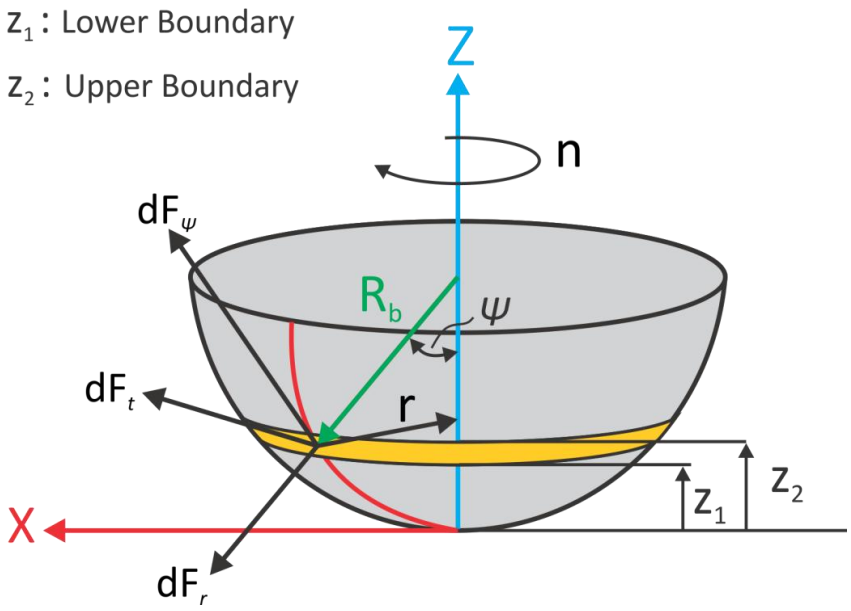

Figure 5.4: Illustration of force components and zenith (ψ) angle

Another important factor while using the cutting coefficients in force model is to select feedrate values according to the feedrate interval of calibration tests. The feedrate interval of this calibration is 48-192 mm/min. If 48-192 mm/min feedrate interval is used for the tip

of the cutter, there will be difference in force values. This discrepancy especially at 0.5 and 1mm depth of cuts is because of the insufficient calibration feedrate interval. Shearing and ploughing occurs at small depth of cuts (very close to tip of the cutter).

Table 5-1: Numerical values of cutting and edge coefficients for different intervals from tip

Interval from tip / **Coefficients**	**0 - 0.5 [mm]**	**0.5 - 1 [mm]**	**1 - 1.5 [mm]**	**1.5 - 2 [mm]**	**2 – 3 [mm]**	**3 – 4 [mm]**	**4 - 5 [mm]**	**5-6 [mm]**
K_{rc} [N/mm^2]	2072	479	49	249	109	173	125	398
K_{re} [N/mm]	45	13	22	7	11	11	19	5
$K_{\psi c}$ [N/mm^2]	1193	419	800	567	266	149	277	142
$K_{\psi e}$ [N/mm]	14	16	7	3	2	8	-2	5
K_{tc} [N/mm^2]	5275	2568	1903	1652	1406	1216	1127	1170
K_{te} [N/mm]	28	18	18	13	11	14	20	10

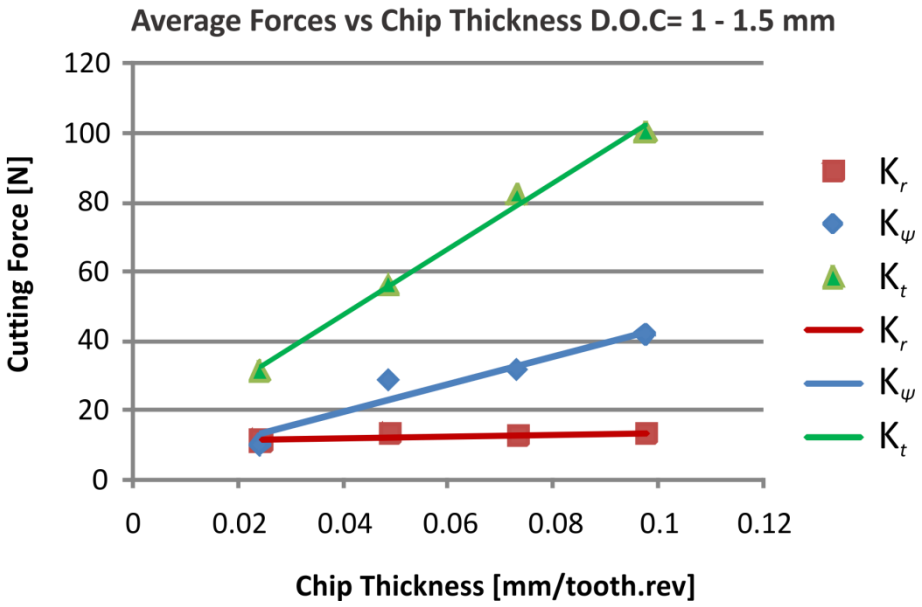

Figure 5.5: Cutting forces vs. chip thickness for 1 – 1.5 mm

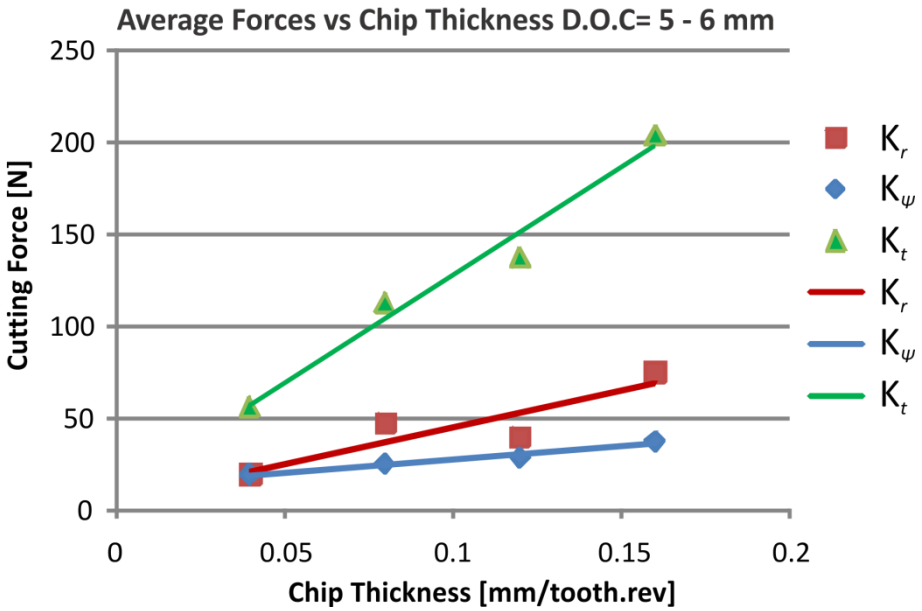

Figure 5.6: Cutting forces vs. chip thickness for 5 – 6 mm

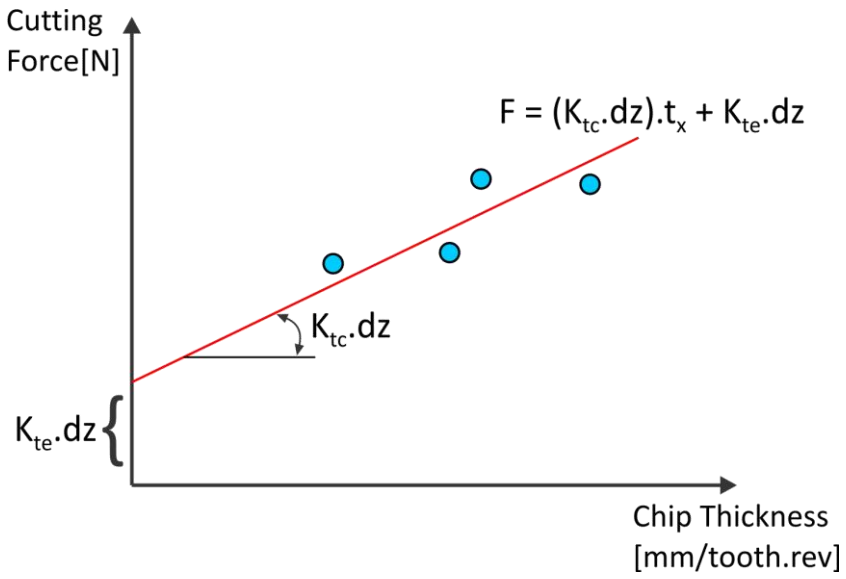

Figure 5.7: Determination of the cutting coefficients from experimental data

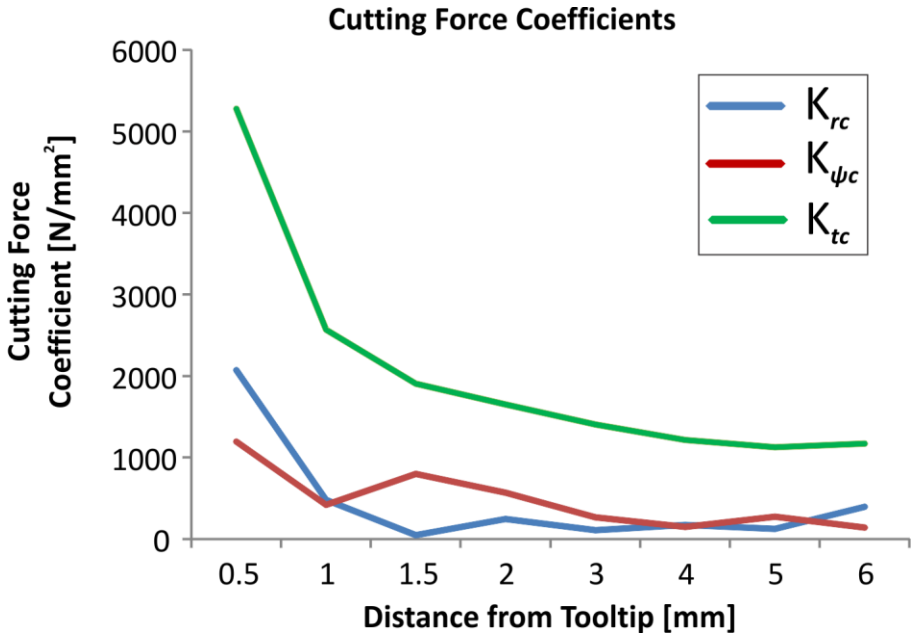

Figure 5.8: Cutting force coefficients

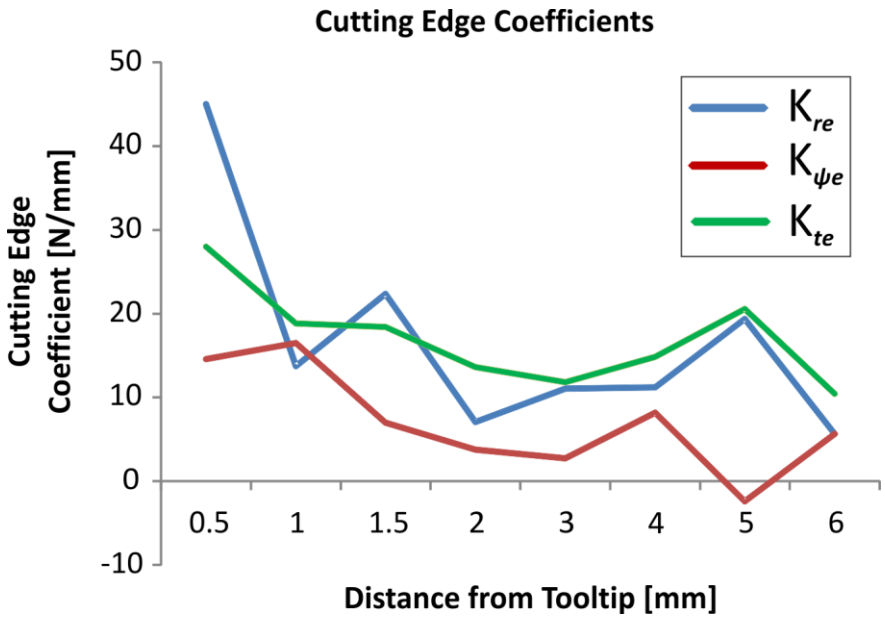

Figure 5.9: Cutting edge coefficients

Second calibration test is made for different set of milling parameters using the same cutting tool and workpiece material (12 mm diameter CoroMill Plura Sandvik ball-end mill and Al7075 material). In this calibration spindle speed is selected to be 3000 rpm and feedrate interval is selected between 300-900 mm/min. The ball part of the ball-end mill is divided into 8 disks for a detailed analysis. Assuming the tip to be at zero level, these intervals are subsequently at 0-0.5, 0.5-1, 1-1.5, 1.5-2, 2-3, 3-4, 4-5, 5-6 mm distance from tip. Each interval is tested for three different feedrate values; 300, 600 and 900 mm/min. Implementing the calibration procedure described above cutting force and edge coefficients are calculated. Obtained calibration coefficients are shown in Table 5-2.

Table 5-2: Numerical values of cutting and edge coefficients for second calibration test

Interval from tip / Coefficients	0 - 0.5 [mm]	0.5 - 1 [mm]	1 - 1.5 [mm]	1.5 - 2 [mm]	2 – 3 [mm]	3 – 4 [mm]	4 - 5 [mm]	5 - 6 [mm]
K_{rc} [N/mm^2]	2022.48	942.62	454.58	735.80	286.02	318.79	495.48	267.65
K_{re} [N/mm]	55.22	7.10	24.16	-4.01	10.30	2.70	-9.24	15.03
$K_{\psi c}$ [N/mm^2]	344.05	144.18	310.56	412.26	324.85	167.81	267.94	205.10
$K_{\psi e}$ [N/mm]	24.56	21.11	14.46	-2.56	-3.55	3.70	0.28	16.34
K_{tc} [N/mm^2]	4213.44	2095.01	1256.03	1155.68	1443	1097.21	928.33	657.52
K_{te} [N/mm]	50.89	23.16	38.07	29.12	-4.02	15.27	25.68	62.39

As shown in Table 5-2 tangential cutting force coefficients decrease since cutting speed is increased 5 times with respect to first calibration test. This also demonstrates that the ploughing effect is also eliminated especially for the region close to tooltip. Contrary to tangential cutting force coefficients, radial and axial cutting force coefficients are observed to increase due to the increase of the feed per tooth value. In the first calibration test maximum feed per tooth value was 0.16 mm/tooth.rev on the other hand for the second test it is selected as 0.2 mm/tooth.rev.

5.3 Cutting Force Coefficient Identification in Rotating Coordinate Frame

Cutting force coefficients for different type of dynamometers may alter due to their working principle. Since table type dynamometers are stationary and cutting tool moves with respect to the dynamometer they are more prone measurement errors due to induced cutting torque and cross-talk between measured forces. Hence, cutting force coefficients

are also obtained by using a rotating coordinate dynamometer (RCD). This may lead to more accurate interpretation of the cutting force coefficients due to measurement in tool coordinate frame.

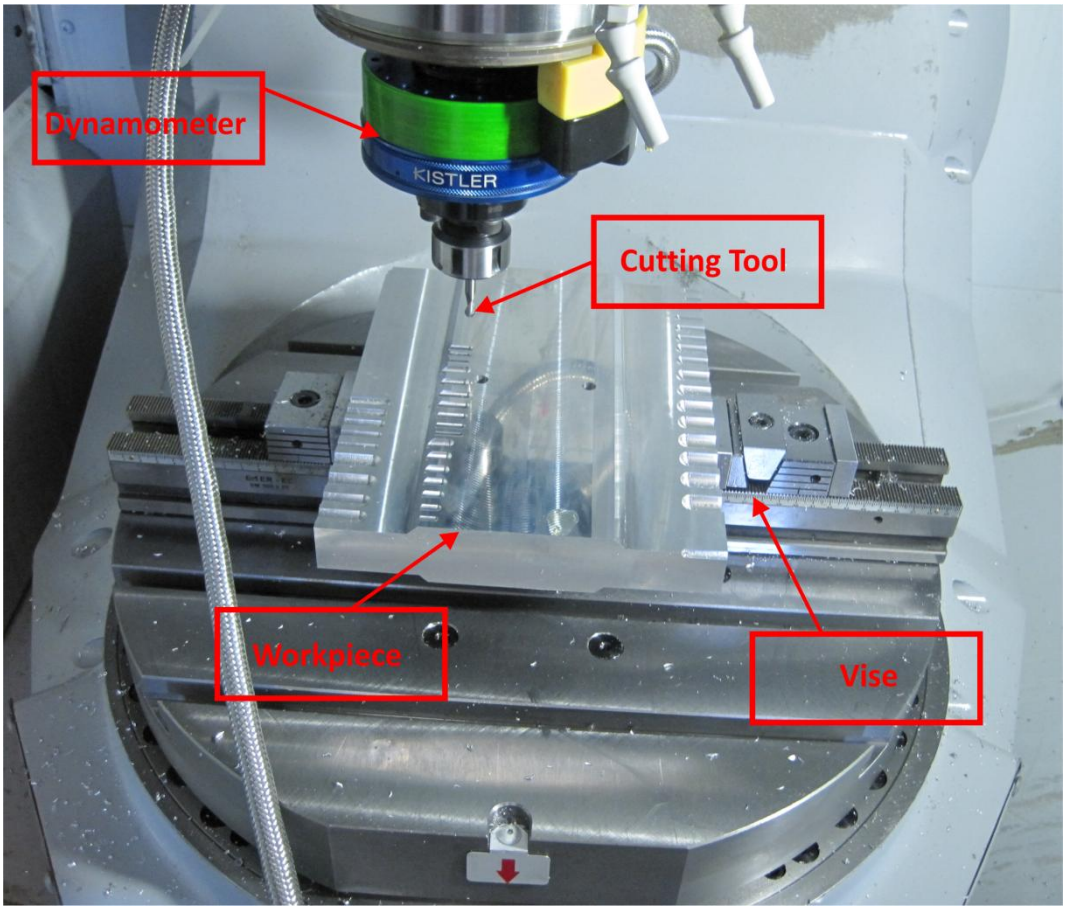

Figure 5.10: Experimental setup for the rotating coordinate dynamometer calibration test

The experiments are performed on Mori Seiki NMV5000 DCG 5-axis vertical machining center. The cutter is carbide ball-end mill cutter from CoroMill Plura series of Sandvik with 6 mm diameter and 30 degrees helix angle. The workpiece material is Al7075. Kistler 9123C rotating cutting force dynamometer and a charge amplifier is used

to measure cutting forces. The dynamometer is attached to the spindle of the machine and the workpiece is fixed to the rotary table of the machine using a vise as seen in Figure 5.10.

Cutting forces are measured for a set of milling experiments in the range of 250 - 750 mm/min. The ball part of the ball-end mill has been divided into 6 disks for a detailed analysis. Assuming the tip to be at zero level, these intervals were subsequently at 0-0.5, 0.5-1, 1-1.5, 1.5-2, 2-2.5, 2.5-3 mm distance from tip. Each interval has been tested for three different feedrate values; 250, 500 and 750 mm/min. The collection of data is made at every 4 degrees. Spindle speed is selected as 5000 rpm and the sampling frequency is set to 7500 Hz.

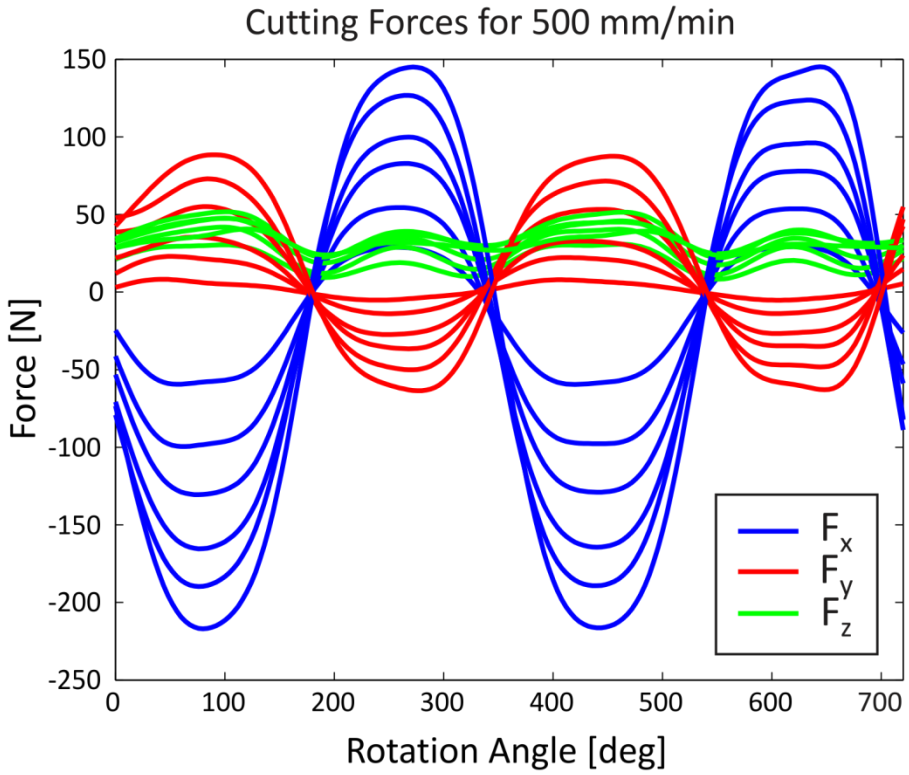

Figure 5.11: Cutting forces corresponding to chosen depth of cuts, at 500 mm/min

Cutting coefficients with a rotating coordinate dynamometer can be obtained using the same procedure described in Chapter 5.2 with minor modifications. For inverse

transforming the measured forces Equation (6.18) to Equation (6.22) is used. Results of the calibration tests are given in the Table 5-3.

Table 5-3: Cutting force and edge coefficients for the calibration with RCD

Interval from tip / **Coefficients**	**0 - 0.5 [mm]**	**0.5 - 1 [mm]**	**1 - 1.5 [mm]**	**1.5 - 2 [mm]**	**2 – 2.5 [mm]**	**2.5 –3 [mm]**
K_{rc} [N/mm^2]	968.03	559.22	410.09	434.06	571.55	477.24
K_{re} [N/mm]	16.29	1.10	3.22	2.77	-0.15	6.34
$K_{\psi c}$ [N/mm^2]	713.87	344.58	322.41	201.25	275.68	696.63
$K_{\psi e}$ [N/mm]	4.44	3.16	1.32	4.04	1.41	-20.40
K_{tc} [N/mm^2]	3749.68	1503.44	1085.98	938.61	788.19	856.15
K_{te} [N/mm]	14.39	17.57	15.32	12.16	13.33	10.44

Chapter 6

MECHANISTIC CUTTING FORCE MODEL

6.1 Introduction

End-mills can be characterized with many aspects, such as the macro geometry (helical-end, ball-end, bull-nose, flat-end, tapered, etc.), the micro geometry (helix, rake, clearance angles), the tool material (WC, PCD, HSS), the coating material (nanocomposite PVD, TiAlN, TiCN, etc.), the area of usage (rough, semi-finish, finish, super-finish milling), and the workpiece material (steel, aluminum, titanium, etc.). Illustration of different types of milling operations is shown in Figure 6.1.

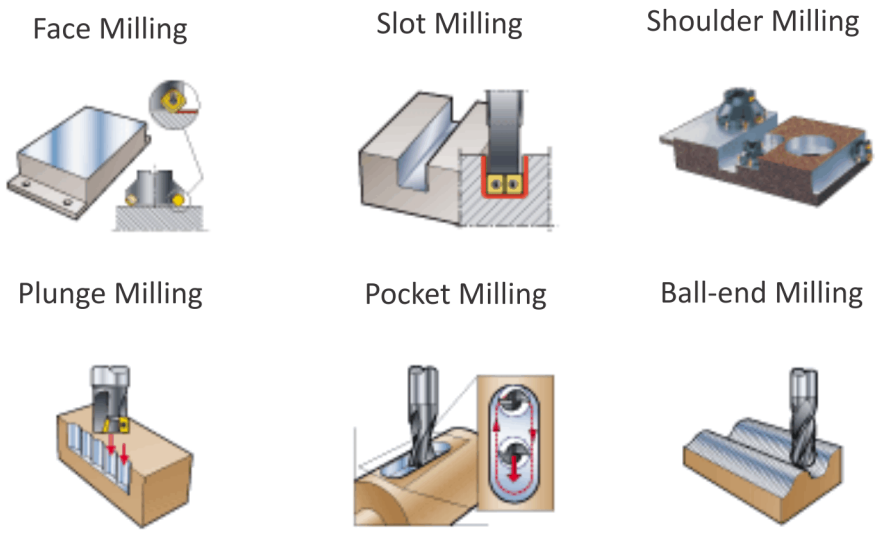

Figure 6.1: Different types of milling operations [53].

Detailed explanation of the micro-geometric properties of the end-mills as follows,

- Positive rake angle improves the shearing and cutting while decreasing the cutting forces. On the other hand, it weakens the cutting edge and makes it more vulnerable to wear and breakage.
- High helix angle smoothens and reduces the impact force during entry cutting and it help to remove away the chip.
- Clearance angle reduces the rubbing on the machined surface; therefore, it increases the surface quality. However, it weakens the cutting edge and more importantly, it increase the possibility of chatter vibrations by reducing process damping. A second clearance angle should be provided to reduce the amount of grinding during sharpening.
- Helical end-mills have constant radius and helix angle along the depth of cut. Ball-end mills differ from flat end mills by their ball part such that their radius varies along the ball-end. This varying radius r affects the cutting forces, because cutting speed changes with varying r. On the contrary, flat-end mills have constant cutting speed along the tool axis.

The detailed geometry of a ball-end mill is shown in Figure 6.2. It can be observed that each flute lies on the surface of the hemisphere, and has a changing helix angle. Due to the decreasing radius towards the tip of the cutter, the local helix angle changes with varying cutting velocity for a discrete point along the cutting flute.

The equation of the geometry of the ball part is given by,

$$x^2 + y^2 + (R_b - z)^2 = {R_b}^2 \tag{6.1}$$

where *x*, *y*, and *z* are the coordinates of cutting edge ball-end mill according to the coordinate axes shown in Figure 6.2, and R_b is the ball radius measured from the center of the sphere. The cutter radius is zero at the tip and at axial location z, in plane x-y,

$$r^2 = x^2 + y^2 \tag{6.2}$$

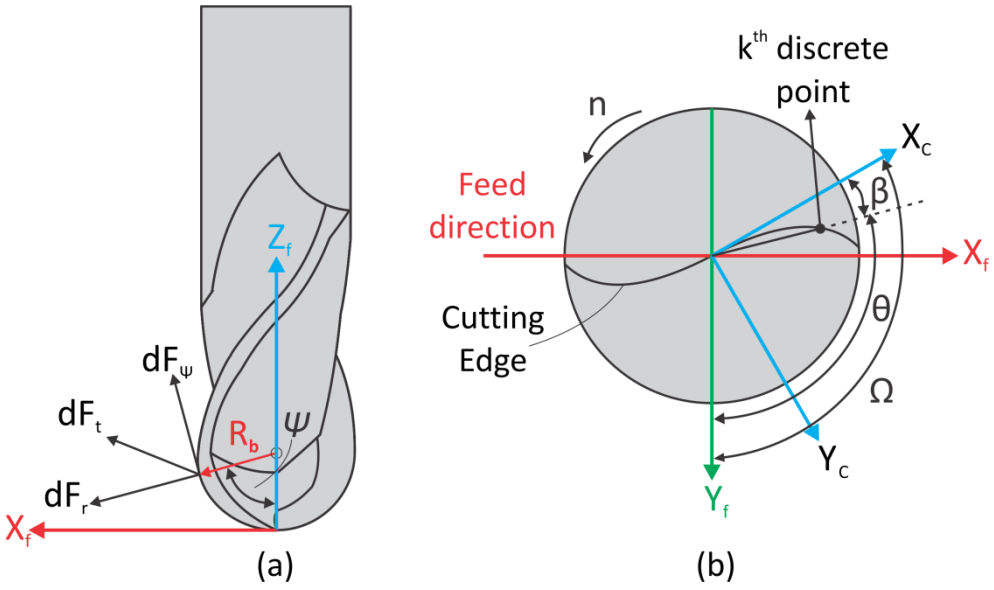

Figure 6.2: Illustration of cutting force vectors and angular relationships.

The ball-mill cutter used in calibration and validation tests is 12 mm diameter, two fluted ball-end mill from CoroMill series of Sandvik. Cutting edge geometry is taken from Erdim [9]. The author measured the cutting edge with a Coordinate Measuring Machine (CMM). Obtained data points were used to obtain following third degree polynomial that represents the cutting edge geometry for the cutting force model.

$$\beta = 0.0036 \times r^3 - 0.0205 \times r^2 + 0.0547 \times r - 0.041 \tag{6.3}$$

where r [mm] is the radius of an arbitrary point on the cutting edge perpendicular to the cutter axis, and β [deg] is the lag angle between the line which connects this arbitrary point to the tip and the line tangent to the cutting edge at the tip. Details of the cutting edge geometry can be seen in Figure 6.3. The cutting geometry can be represented in the cutter coordinate system as the following;

$$x_c = r \times \cos(\beta), \quad y_c = r \times \sin(\beta), \quad z_c = R_b - \sqrt{R_b^2 - r^2} \tag{6.4}$$

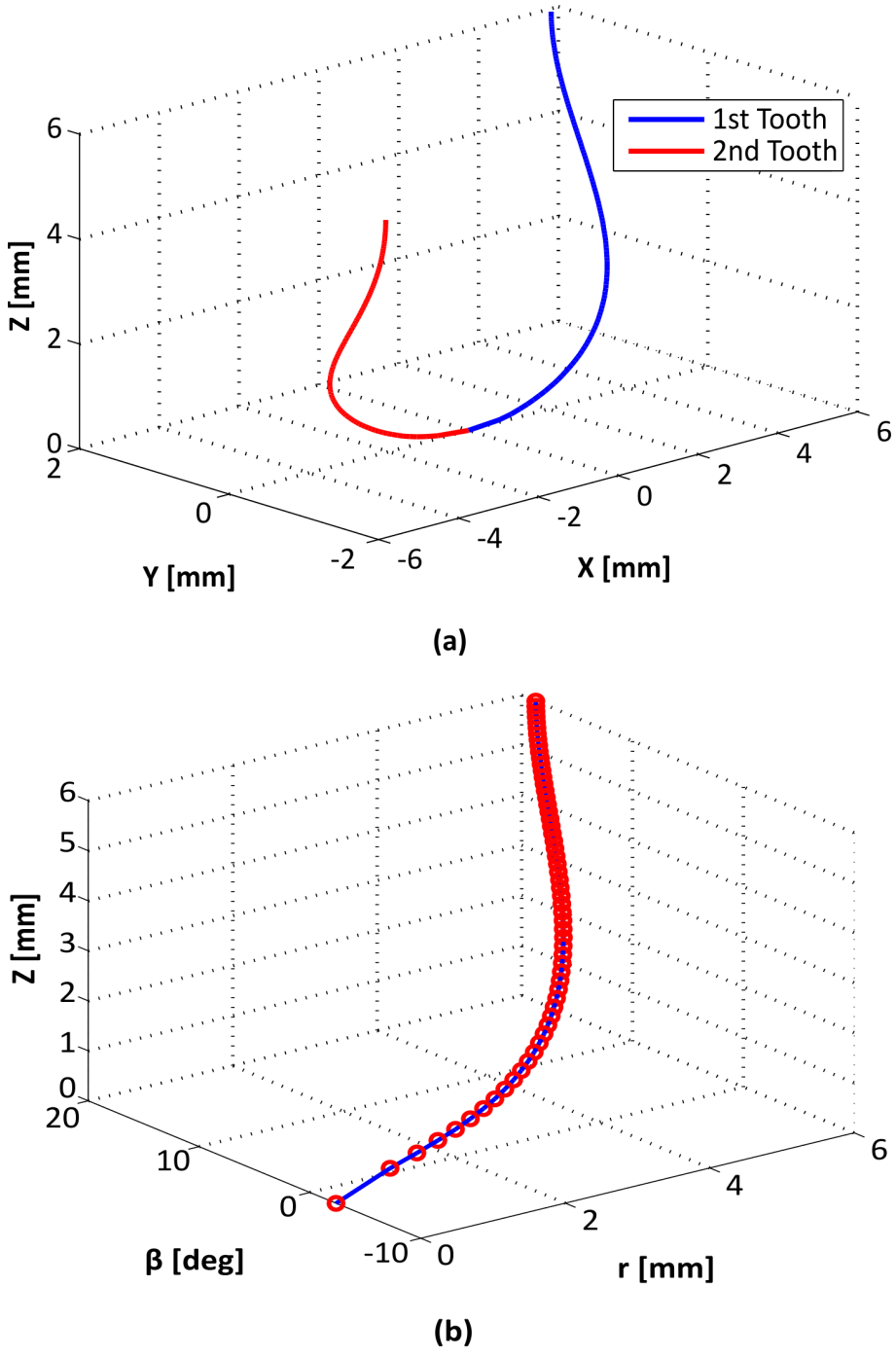

Figure 6.3: a) Cutting edges, b) Third degree polynomial fitting for $\beta(r)$.

Another approach for the determination of the lag angle of the cutter due to helix angle is given in [54]. In this approach lag angle is calculated spatially on the cutter considering the helix angle of the tool and the height from the tool tip. For practical applications this approach can also be used with acceptable error.

6.2 Geometry of 5-axis Milling

5-axis milling geometry differs from 3-axis milling geometry. Hence transformation from 3-axis milling to 5-axis milling has to be defined. In this section, important concepts and parameters which define geometry of 5-axis machining is introduced. Then, these formulations are used in mechanistic cutting force modeling of 5-axis machining.

In 3-axis milling tool movement is given as three translational motions along the X-Y-Z coordinate frame axes. In 5-axis milling two additional rotary axes are present. Consequently, tool motion is defined as a combination of three translational motions and two rotational motions. There are several different kinematic configurations in 5-axis machine tools [45]. In this study all of the formulations are presented according to a table tilting-rotating 5-axis vertical machine tool.

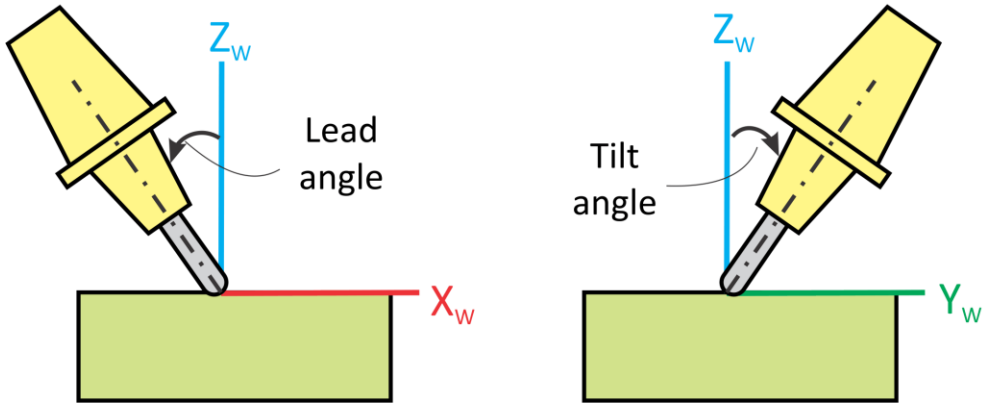

Figure 6.4: Definition of Lead and Tilt angles.

Contrary to 3-axis milling, tool orientation vector in 5-axis milling is not constant. Therefore, tool coordinate frame (TCF) has to be mapped on to the workpiece coordinate frame (WCF).

Two additional rotational motion in 5-axis milling is given as lead and tilt angles. Lead angle is defined as the rotation angle about Y_w which is Y axis of workpiece coordinate frame. Tilt angle is the rotation angle about $X_w$which is X axis of the workpiece coordinate frame. Definition of the lead and tilt angles is shown in Figure 6.4.

It is worthwhile to state that there are other conventions [42] which use feed and cross feed vectors as reference frames, however if these angles are calculated relative to these vectors, reference for angles naturally becomes drive surface and if the surface normal has a large angle with machine tool axis there may be unrealizable lead and tilt angles.

In order to extract lead and tilt angles from toolpath data CL (Cutter Location) output of Siemens NX6 is used. CL file is parsed via a pre-processor, and then CL points and tool orientation vectors in the form of direction cosines are obtained. Example CL block is shown in Figure 6.5. GOTO/ keyword states the beginning of a CL point block, three numbers after the keyword gives X, Y and Z coordinates of the tooltip in the workpiece coordinate frame respectively. Remaining three numbers gives the tool orientation vectors *i, j, k* respectively relative to workpiece coordinate frame.

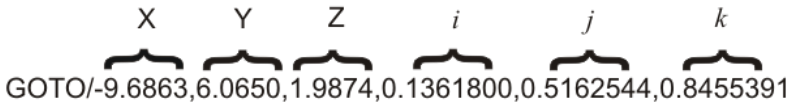

Figure 6.5: Example Cutter Location block.

Lead and tilt angles can be calculated as:

$$lead = atan2(i, \sqrt{j^2 + k^2}) \tag{6.5}$$

$$tilt = atan2(-j, k) \tag{6.6}$$

Since, transformation from the workpiece coordinate frame to the tool coordinate frame is necessary for inverse transforming the calculated cutting forces in cutting force model; the rotation matrix from workpiece coordinate frame to tool coordinate frame has to be calculated.

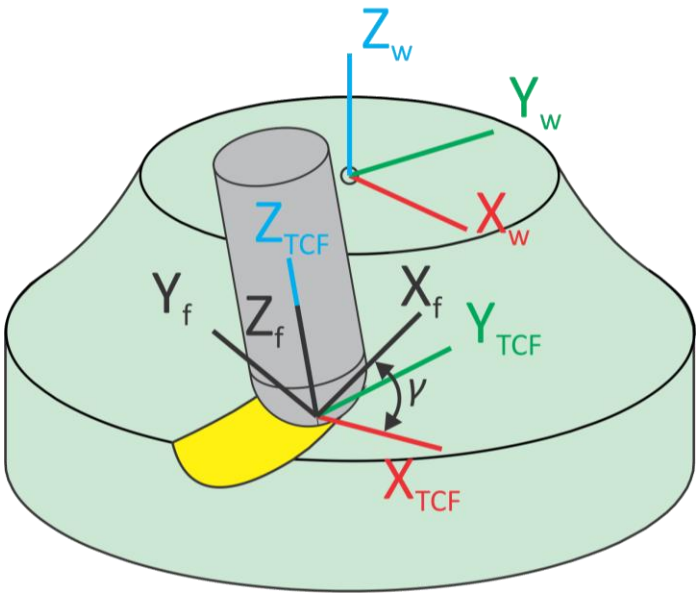

Figure 6.6: Illustration of coordinate frames.

Illustration of coordinate frames is shown in Figure 6.6 where $(X_f - Y_f - Z_f)$ is the feed coordinate frame, and it is be explained in the Chapter 6.3. Transformation matrix from workpiece coordinate frame to tool coordinate frame is given as:

$$T = \begin{bmatrix} \cos(lead) & 0 & \sin(lead) \\ \sin(tilt)\sin(lead) & \cos(tilt) & -\sin(tilt)\cos(lead) \\ -\cos(tilt)\sin(lead) & \sin(tilt) & \cos(tilt)\cos(lead) \end{bmatrix} \tag{6.7}$$

Inverse of transformation matrix T gives the necessary transformation from TCF to WCF as:

$$T_I = T^{-1} = T^T \tag{6.8}$$

Cutting forces calculated in TCF can be transformed to WCF as follows:

$$\begin{bmatrix} F_x \\ F_y \\ F_z \end{bmatrix}_{WCF} = T_I \begin{bmatrix} F_x \\ F_y \\ F_z \end{bmatrix}_{TCF} \tag{6.9}$$

6.3 Cutting Force Model in Fixed Coordinate Frame

In milling, cutting forces depend on the instantaneous chip thickness. Hence, for 5-axis machining cutting force predictions, accurate calculation of the chip thickness is quite critical since tool can rotate as well as translate within a toolpath segment.

In free-form surface machining the distance and the rotation angle between two CL points are relatively small, therefore the effect of rotational velocities of the tool is negligible. On the other hand, the effect of the lead and tilt angles on the cut geometry, and horizontal and vertical feed components has to be considered.

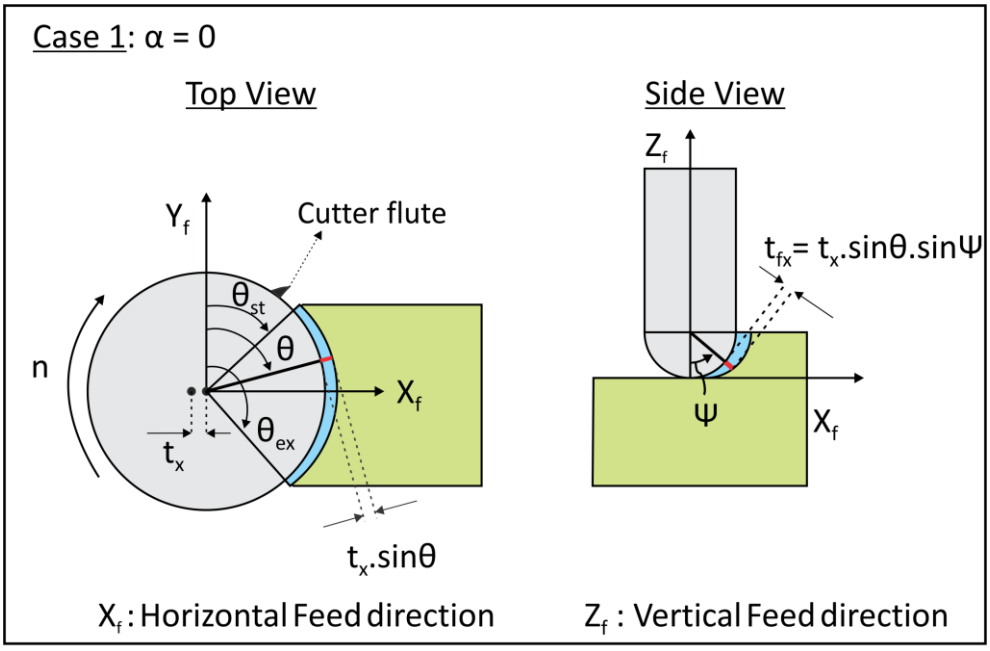

Figure 6.7: Chip thickness due to horizontal feed.

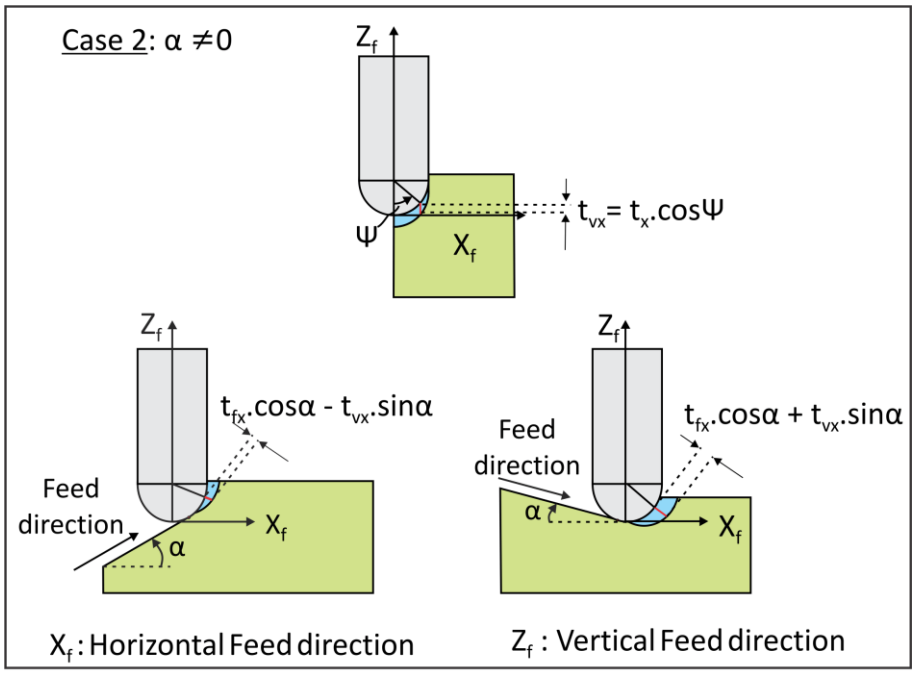

Figure 6.8: Chip thickness due to horizontal and vertical feed

For ball-end mill tool, instantaneous undeformed chip thickness is obtained as follows [55];

$$(t_c)_k = t_x \times \sin(\theta) \times \sin(\psi) \times \cos(\alpha) \pm t_x \times \cos(\psi) \times \sin(\alpha) \quad (6.10)$$

where $(t_c)_k$ is the chip thickness, t_x is the feed per tooth, θ is the immersion angle of the cutting point, ψ is the cutting element position angle, and α is the feed inclination angle measured with respect to horizontal feed direction. Distribution of horizontal and vertical chip thickness are shown in Figure 6.7 and Figure 6.8

The immersion angle of a discrete cutting point on the flute of the cutter is given as:

$$\theta = \Omega + 2\pi(n-1)/N_f - \beta_k \quad (6.11)$$

where θ is the immersion angle for flute n, k represents the number of discrete point on a cutting edge, Ω is the cutting edge rotation angle, N_f is the total number of flutes and β_k is the lag angle due to helix angle of the cutter in the respective kth disk.

The instantaneous infinitesimal chip load is written as follows:

$$dA_c = (t_c)_k \times (dz)_k \tag{6.12}$$

For a differential chip load dA_c in the engagement domain, the differential cutting forces in radial, axial, and tangential directions (r, ψ, t) is written as follows;

$$\begin{aligned} dF_r &= K_{rc} \times dA_c + K_{re} \times dz \\ dF_\psi &= K_{\psi c} \times dA_c + K_{\psi e} \times dz \\ dF_t &= K_{tc} \times dA_c + K_{te} \times dz \end{aligned} \tag{6.13}$$

where K_{rc}, $K_{\psi c}$ and K_{tc} are radial, axial and tangential cutting force coefficients and K_{re}, $K_{\psi e}$ and K_{te} are cutting edge coefficients respectively. Cutting force and edge coefficients are determined by mechanistic calibration procedure where these coefficients vary along tool axis direction [55].

Transformation matrix A transforms the cutting forces into feed coordinate frame which is initially coincident with TCF. If the angle between feed direction and X_{TCF} is not zero, B matrix transforms the cutting forces into tool coordinate frame.

$$A = \begin{bmatrix} -\sin(\psi) \times \sin(\theta) & -\cos(\psi) \times \sin(\theta) & -\cos(\theta) \\ \sin(\psi) \times \cos(\theta) & \cos(\psi)\cos(\theta) & -\sin(\theta) \\ \cos(\psi) & -\sin(\psi) & 0 \end{bmatrix} \tag{6.14}$$

$$B = \begin{bmatrix} \cos\gamma & -\sin\gamma & 0 \\ \sin\gamma & \cos\gamma & 0 \\ 0 & 0 & 1 \end{bmatrix} \tag{6.15}$$

In this formulation, a table type dynamometer (fixed coordinate frame) is used. Therefore, cutting forces in feed coordinate frame are transformed into WCF which is also dynamometer coordinate frame. By using transformation matrix T_I given in Equation 6.8, cutting forces in WCF is written as:

$$\begin{bmatrix} dF_X \\ dF_Y \\ dF_Z \end{bmatrix} = [T_I][B][A] \times \begin{bmatrix} dF_r \\ dF_\psi \\ dF_t \end{bmatrix} \tag{6.16}$$

Finally calculated cutting forces are summed for the all of the axial disks and the cutting flutes in order to obtain total cutting force for an immersion angle of $\theta(z,k)$.

$$\begin{bmatrix} F_X \\ F_Y \\ F_Z \end{bmatrix} = \sum_{n=1}^{N_f} \sum_{k=1}^{K} \begin{bmatrix} dF_X \\ dF_Y \\ dF_Z \end{bmatrix} \Big|_{k,n} \tag{6.17}$$

6.4 Cutting Force Model in Rotating Coordinate Frame

Cutting force measurement in 5-axis machining is a challenging task due to the varying orientation of the tool axis with respect to the workpiece. In 5-axis milling cutting forces can be measured in two ways.

First one is using a table type dynamometer which is attached to the rotary table of the machine tool. In this method dynamometer coordinate frame is fixed and transformation from tool coordinate system to dynamometer coordinate frame is difficult. Furthermore, due to the rotation of the rotary axis of the machine tool measured data is affected by the weight of the workpiece and forces induced by the cutting torque.

Second method requires the use of a rotary dynamometer. Rotary dynamometer is directly attached to the spindle of the machine tool and cutting tool is attached to the dynamometer. In other words, cutting forces are directly measured with respect to tool coordinate frame and the effects of the machine tool rotary axes are eliminated. In this

study, Kistler 9123C rotating cutting force dynamometer is used. Detail of the Kistler 9123C rotating cutting force dynamometer is shown in Figure 6.9.

Figure 6.9: Kistler 9123 rotating cutting force dynamometer

With this rotating cutting force dynamometer (RCD) cutting forces in three orthogonal directions ($X_D - Y_D - Z_D$ directions) and the cutting moment about the Z_D axis can be measured. $X_D - Y_D - Z_D$ represents the rotating dynamometer coordinate frame.

6.4.1 Transformation to Rotating Coordinate Frame

In Chapter 6.3, cutting force modeling in feed coordinate frame and its transformation to fixed coordinate frame is given. In this section, transformation from feed coordinate frame $(X_f - Y_f - Z_f)$ to rotating dynamometer coordinate frame $(X_D - Y_D - Z_D)$ is introduced.

Consider a two fluted ball-end mill where the cutting flute of the cutter is supposed to be aligned with the X axis of the dynamometer and is traveling along an arbitrary direction.

In this position, the angle between Y axis of the dynamometer (Y_D) and the first cutting flute of the cutter is represented as the reference rotation angle Ω_R. The rotation angle Ω is the angle between the cross feed direction and the cutting flute. Reference rotation angle is constant unless tool alignment changes with respect to dynamometer coordinate frame. In contrary, rotation angle is updated during the simulation at each time step by the given rotation increment angle. For inserted milling cutters and end mills alignment of the cutting flute with the X_D axis can be performed easily on the other hand for ball mills due to the complex cutting flute geometry perfect alignment may not be achieved. In this case, a misalignment angle Ω_a is defined in order to compensate the error introduced. Detailed illustration of the transformation angles is shown in Figure 6.10.

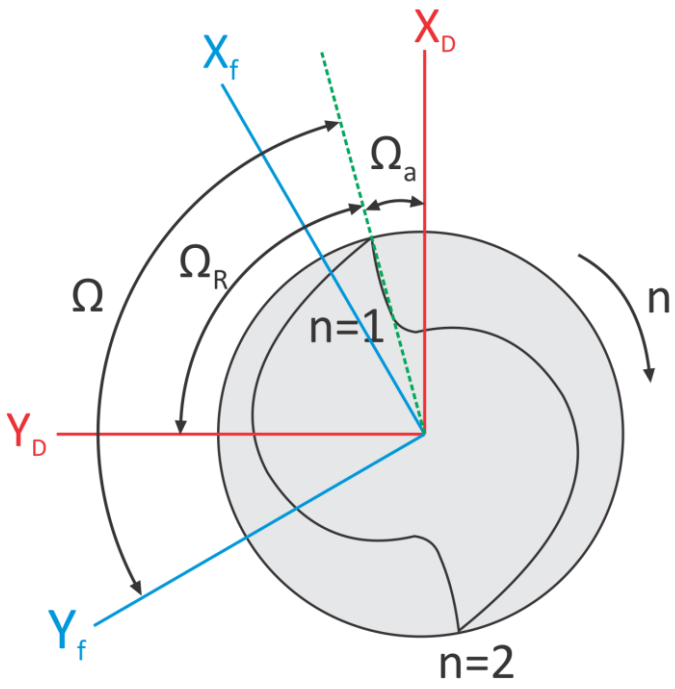

Figure 6.10: Rotating coordinate frame transformation angles

General definition of the rotating coordinate frame is given above. For clarity two special cases are shown in Figure 6.11 and Figure 6.12.

In the first case, at the instant shown consider that cutting edge of the cutter is perfectly aligned with the X axis of the rotating dynamometer therefore reference rotation angle Ω_R is 90° and rotation angle Ω is 0°, meaning that feed coordinate system must be rotated 90° counter clockwise for mapping the feed coordinate frame onto dynamometer coordinate frame.

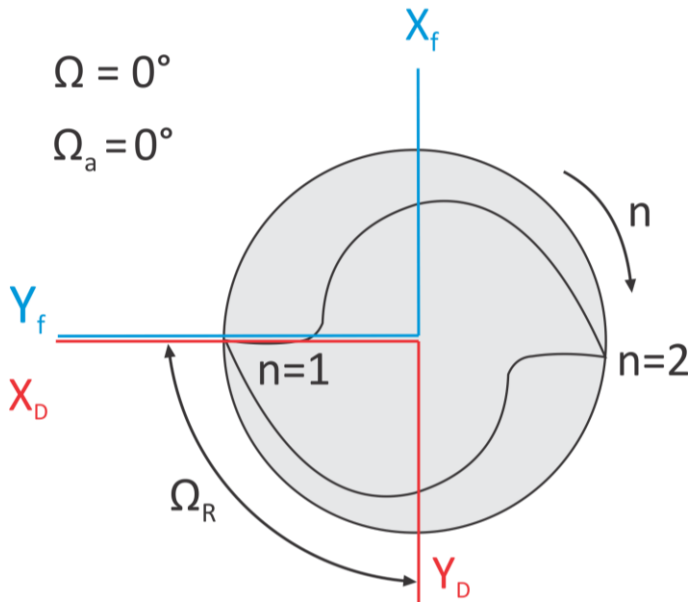

Figure 6.11: Special case 1 $\Omega_R = 90°$

For the second case, at the instant shown consider that cutting edge of the cutter is perfectly aligned with the Y axis of the rotating dynamometer therefore reference rotation angle Ω_R is 0° and rotation angle Ω is 0°, therefore feed coordinate frame and dynamometer coordinate frames are coincident. In both cases, since it is assumed that tool cutting edge is perfectly aligned with the desired rotating coordinate frame axis misalignment angle Ω_a is equal to 0°.

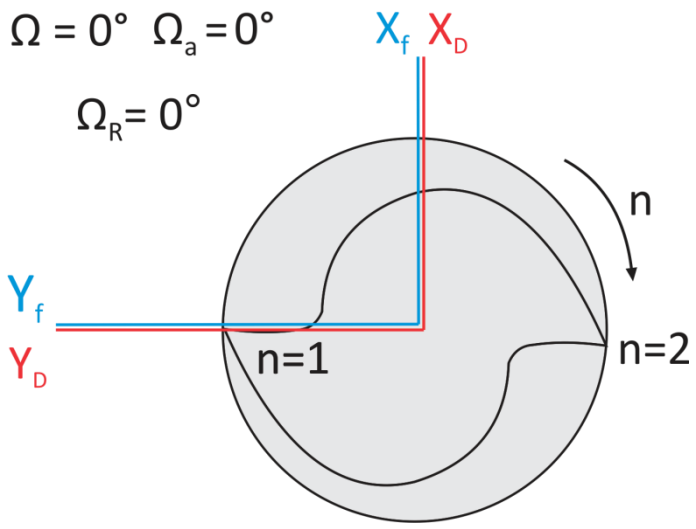

Figure 6.12: Special case 2 $\Omega_R = 0°$

In order to obtain the transformation from the $(r - \psi - t)$ coordinate frame to feed coordinate frame transformation matrix given in Equation 6.14 is modified as,

$$A = \begin{bmatrix} -\sin(\psi) \times \sin(\theta) & -\cos(\psi) \times \sin(\theta) & -\cos(\theta) \\ -\sin(\psi) \times \cos(\theta) & -\cos(\psi)\cos(\theta) & \sin(\theta) \\ \cos(\psi) & -\sin(\psi) & 0 \end{bmatrix} \tag{6.18}$$

Transformation from the feed coordinate system to rotating dynamometer coordinate frame can be obtained using these matrices,

$$B = \begin{bmatrix} \cos(\Omega_R + \Omega) & -\sin(\Omega_R + \Omega) & 0 \\ \sin(\Omega_R + \Omega) & \cos(\Omega_R + \Omega) & 0 \\ 0 & 0 & 1 \end{bmatrix} \tag{6.19}$$

$$C = \begin{bmatrix} \cos(\Omega_a) & -\sin(\Omega_a) & 0 \\ \sin(\Omega_a) & \cos(\Omega_a) & 0 \\ 0 & 0 & 1 \end{bmatrix} \tag{6.20}$$

If the reference rotation angle is known or can be measured, forces in $X_D - Y_D - Z_D$ can be calculated as,

$$\begin{bmatrix} dF_X \\ dF_Y \\ dF_Z \end{bmatrix}_{\text{RCD}} = [B][A] \times \begin{bmatrix} dF_r \\ dF_\psi \\ dF_t \end{bmatrix} \tag{6.21}$$

If the reference rotation angle is not known or cannot be measured due to complex cutter geometry, misalignment angle can be extracted by running simple slot cutting tests. By examining the force magnitudes for one tool revolution and taking the difference of the simulated peak force rotation angle with the experimental peak force rotation angle.

If this is the case, it is assumed that cutting edge of the cutter is perfectly aligned with the intended coordinate axis of the dynamometer and the misalignment matrix accounts for the misalignment in the calculation.

$$\begin{bmatrix} dF_X \\ dF_Y \\ dF_Z \end{bmatrix}_{\text{RCD}} = [C][B][A] \times \begin{bmatrix} dF_r \\ dF_\psi \\ dF_t \end{bmatrix} \tag{6.22}$$

Chapter 7

FORCE VALIDATION TESTS

7.1 Introduction

Force validation tests are gathered in two groups since cutting force modeling is performed using different types of coordinate frame conventions. In the first part, cutting force modeling for the fixed coordinate frame convention and the in the second part for the rotating coordinate frames cutting force modeling is validated. In fixed coordinate frame modeling cutting forces are measured using a table type dynamometer which is fixed to the rotary table of the machine. For the rotating coordinate frame cutting force modeling a rotating coordinate dynamometer is used which is directly attached to the spindle of the machine tool.

7.2 Validation Tests in Fixed Coordinate Frame

Preliminary study for the validations is performed on 5-axis slotting cases. Five different toolpaths with different lead and tilt angles are simulated and compared with the measured forces. These slotting cases are given in Table 7-1. In these tests, a two fluted carbide ball-end mill with a diameter of 12 mm, nominal helix angle of 30°, and projection length of 37 mm is used on Al7039 workpiece material. The spindle speed and the feedrate are 600 rpm and 48 mm/min respectively. Cutter runout of 10 microns is observed in the measured data and the effect of the runout is taken into account by using the approach given in [56]. Simulated and measured forces are given through Figure 7.1 to Figure 7.10.

Table 7-1: 5-axis slotting experiments

Case #	Lead Angle (°)	Tilt Angle (°)
1	10°	0°
2	10°	-10°
3	10°	10°
4	0°	10°
5	0	-10°

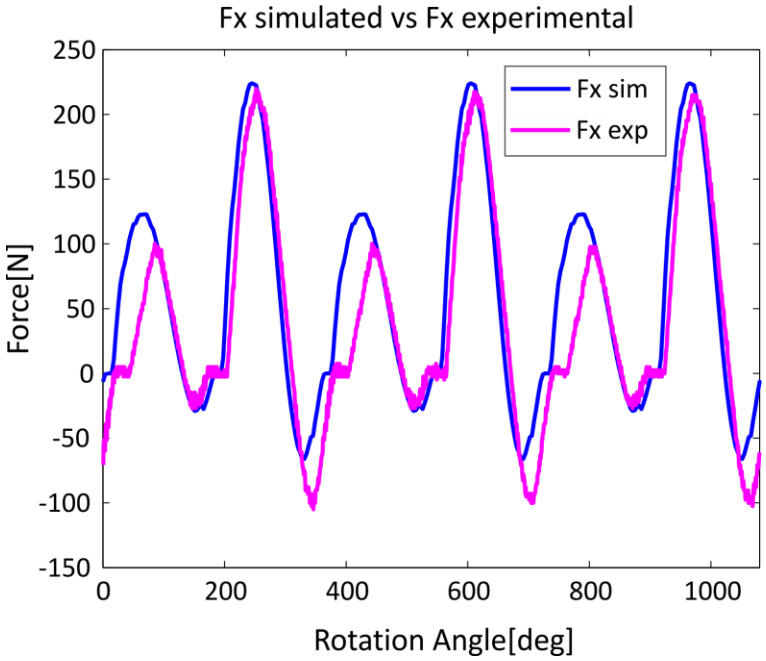

Figure 7.1: Case #1, simulated and experimental Fx forces

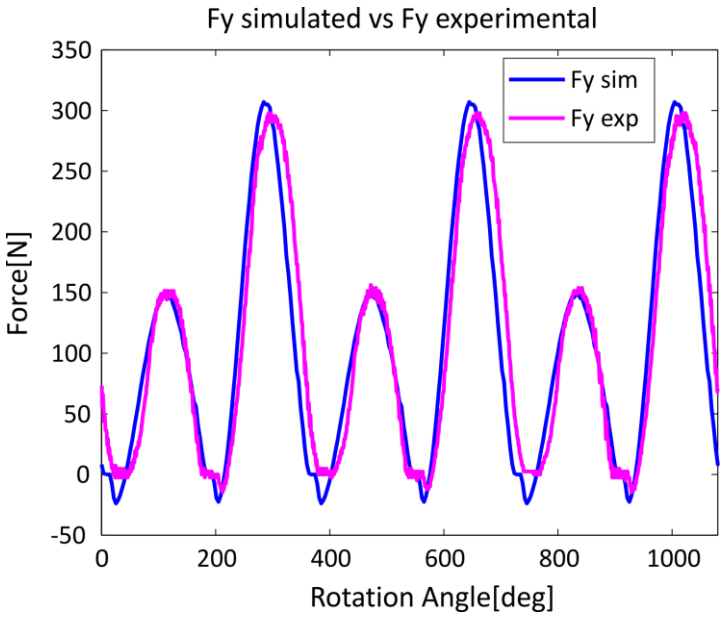

Figure 7.2: Case #1, simulated and experimental Fy forces

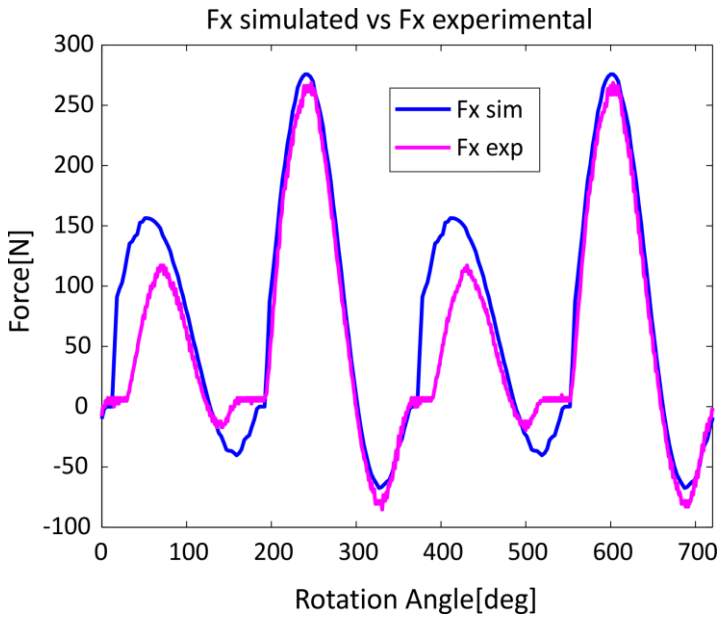

Figure 7.3: Case #2, simulated and experimental Fx forces

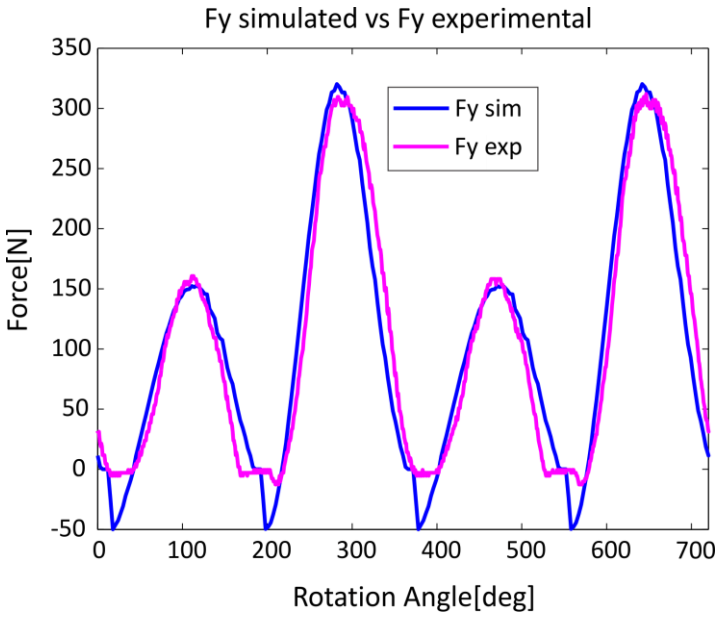

Figure 7.4: Case #2, simulated and experimental Fy forces

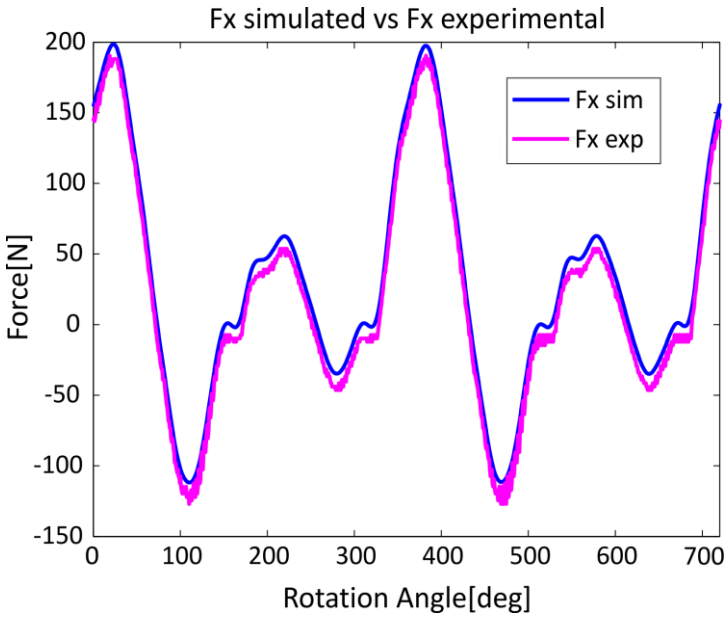

Figure 7.5: Case #3, simulated and experimental Fx forces

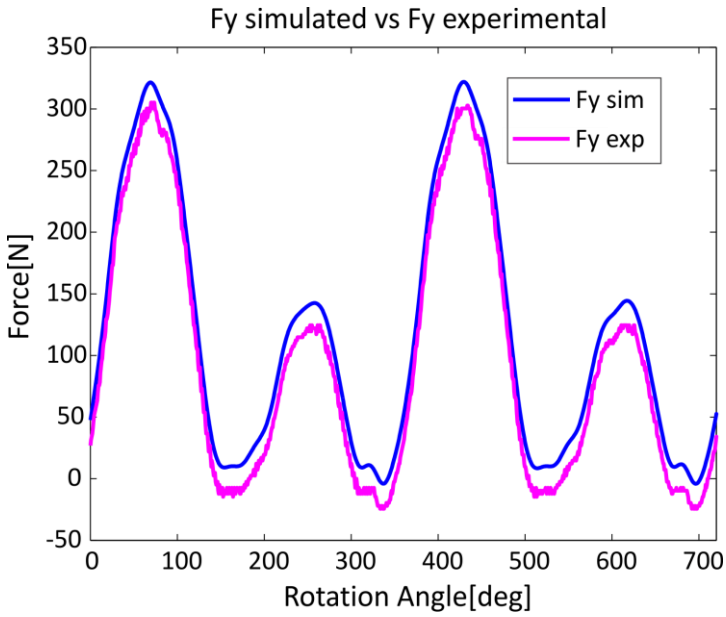

Figure 7.6: Case #3, simulated and experimental Fy forces

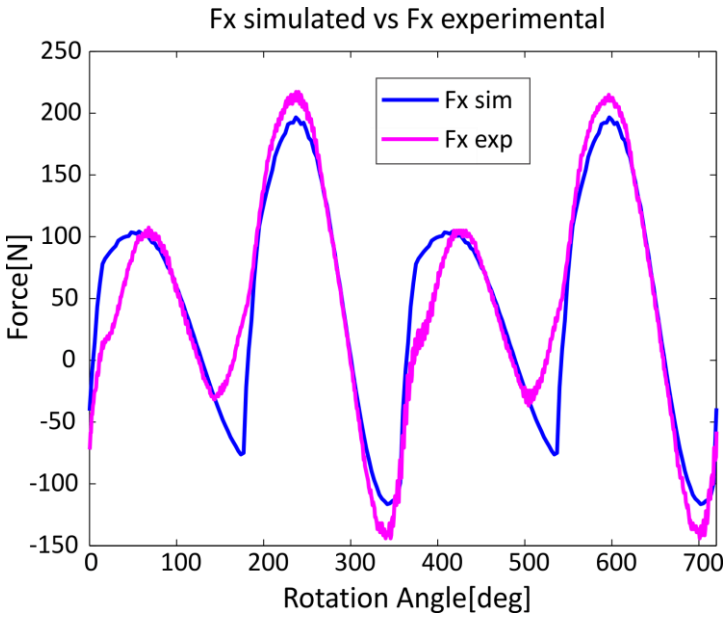

Figure 7.7: Case #4, simulated and experimental Fx forces

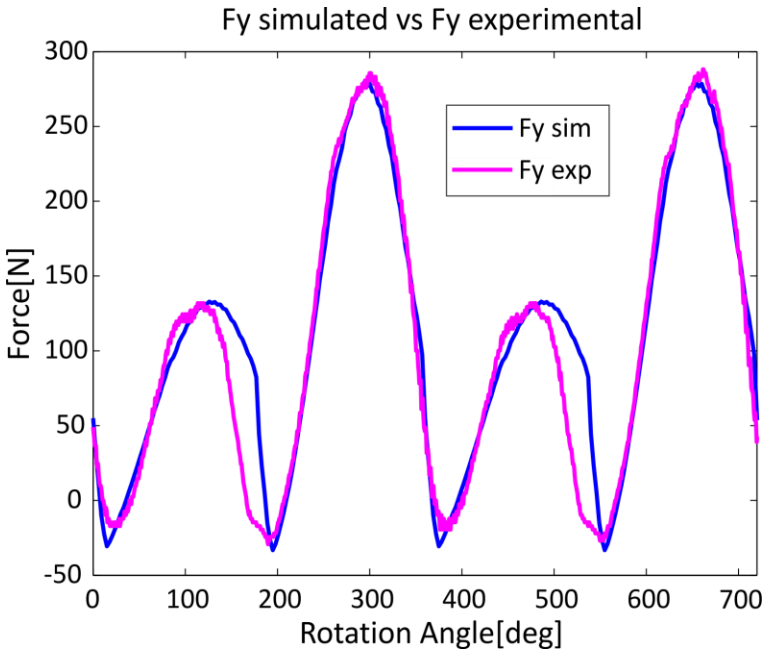

Figure 7.8: Case #4, simulated and experimental Fy forces

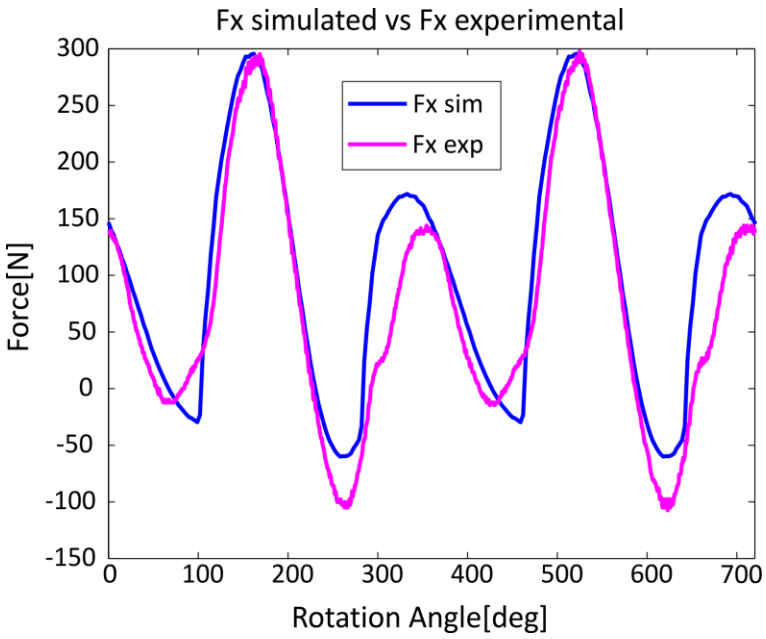

Figure 7.9: Case #5, simulated and experimental Fx forces

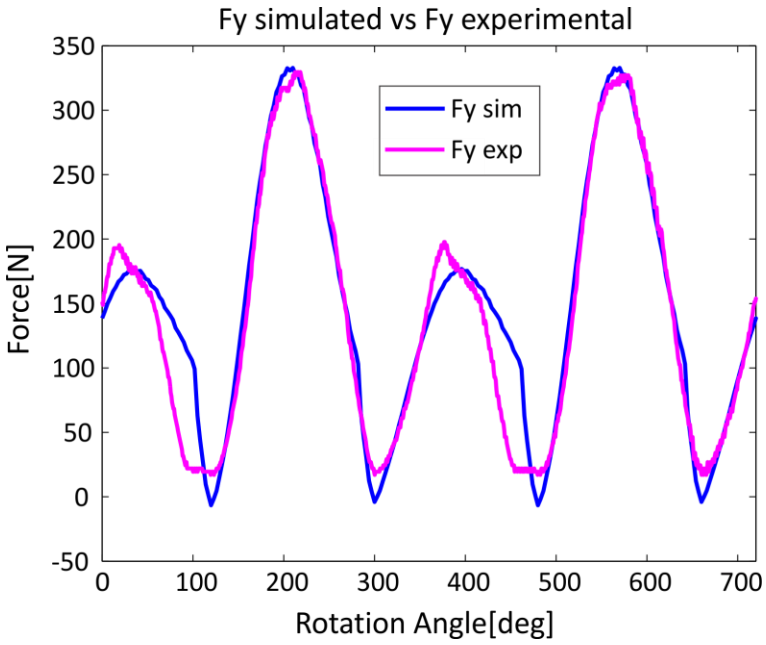

Figure 7.10: Case #5, simulated and experimental Fy forces

As it is demonstrated in the figures, simulated and measured forces match quite well for slotting cases, however main discrepancy in the forces can be attributed to the cutter runout since used model is the simplified model of the true chip formation kinematics.

Free-form surface validation tests are performed on three different toolpaths. First one is airfoil geometry and the other one is the penguin free-form surface. For airfoil geometry test nominal 10° lead angle with smoothing, for penguin free-form surface constant 15° lead and 5° tilt angle is simulated. Details of first two toolpaths are shown in Figure 7.11.

Kistler table type dynamometer is used for measuring forces which is attached to the rotary table of the machine. Although the cutting forces for whole toolpaths are measured and simulated, one passes of both toolpath simulations are compared against experiments for better illustration of the comparison.

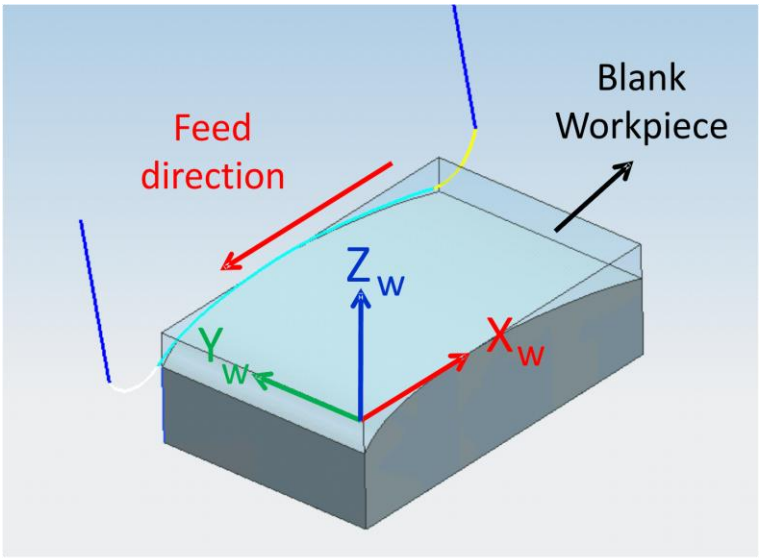

(a)

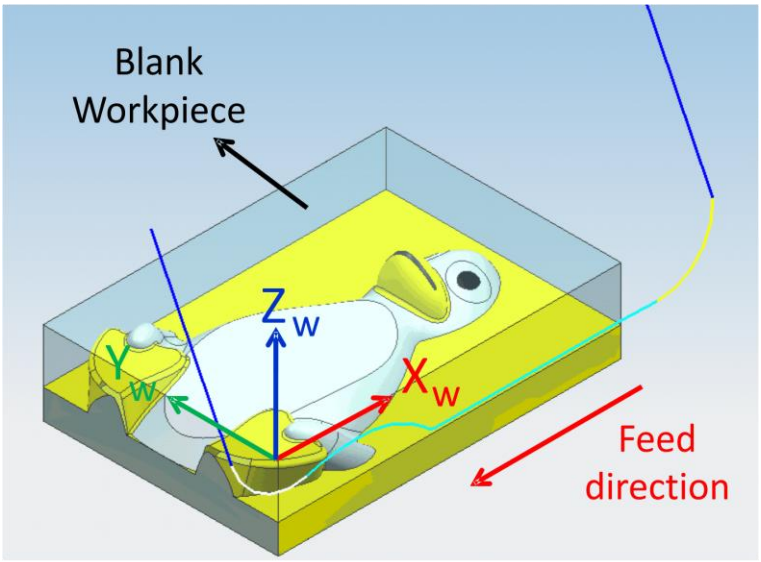

(b)

Figure 7.11: (a) Airfoil geometry, (b) Penguin free-form surface toolpaths.

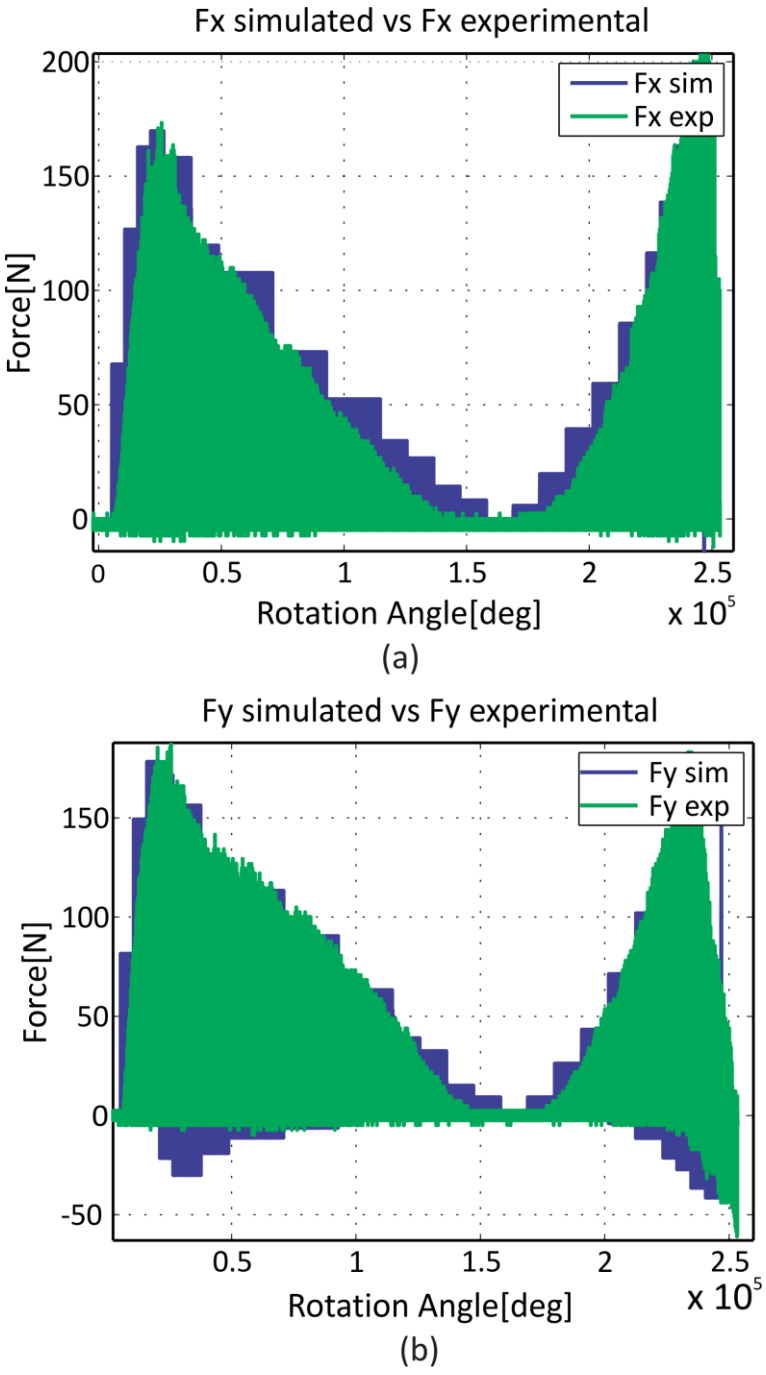

Figure 7.12: Airfoil geometry simulation and experimental cutting force comparison.

The spindle speed and the feedrate for these toolpaths are kept constant at 600 rpm and 48 mm/min respectively. A two fluted ball-end mill with a diameter of 12 mm, nominal helix angle of 30°, and projection length of 37 mm is used on Al7039 workpiece material. Depths of cut during two toolpaths vary approximately between 0 – 5 mm along tool axis.

Figure 7.12 and Figure 7.13 show the comparison for the simulation and the experimental cutting forces. As it is demonstrated in the figures simulated and experimental cutting forces match quite well not only in their trends but also in their amplitudes. In most of the regions, the error between simulation and the experimental force amplitudes is below 15 % which can be considered as acceptable for 5-axis milling process simulations.

The main differences in cutting force predictions can be attributed to the unequal cutter radius of the flutes which may change the force amplitudes with a phase difference in peak forces. This phenomenon is observed in the cutting tool, although a set of the same tool is used. Another reason can be stated as; penguin surface has free-form geometry, in some regions tooltip contact with the workpiece occurs. Therefore, cutting edge of the tool may be rubbing the workpiece material rather than cutting due to zero cutting velocity at the tooltip.

For the third validation test an impeller roughing toolpath is simulated for the cutting force prediction of 5-axis ball-end milling. Lead angles vary between 17° and 66°, and tilt angles vary between 32° and 19°. The simulated toolpath is shown in Figure 7.14. Dimensions of the blank workpiece and the workpiece coordinate frame are also illustrated in Figure 7.14.

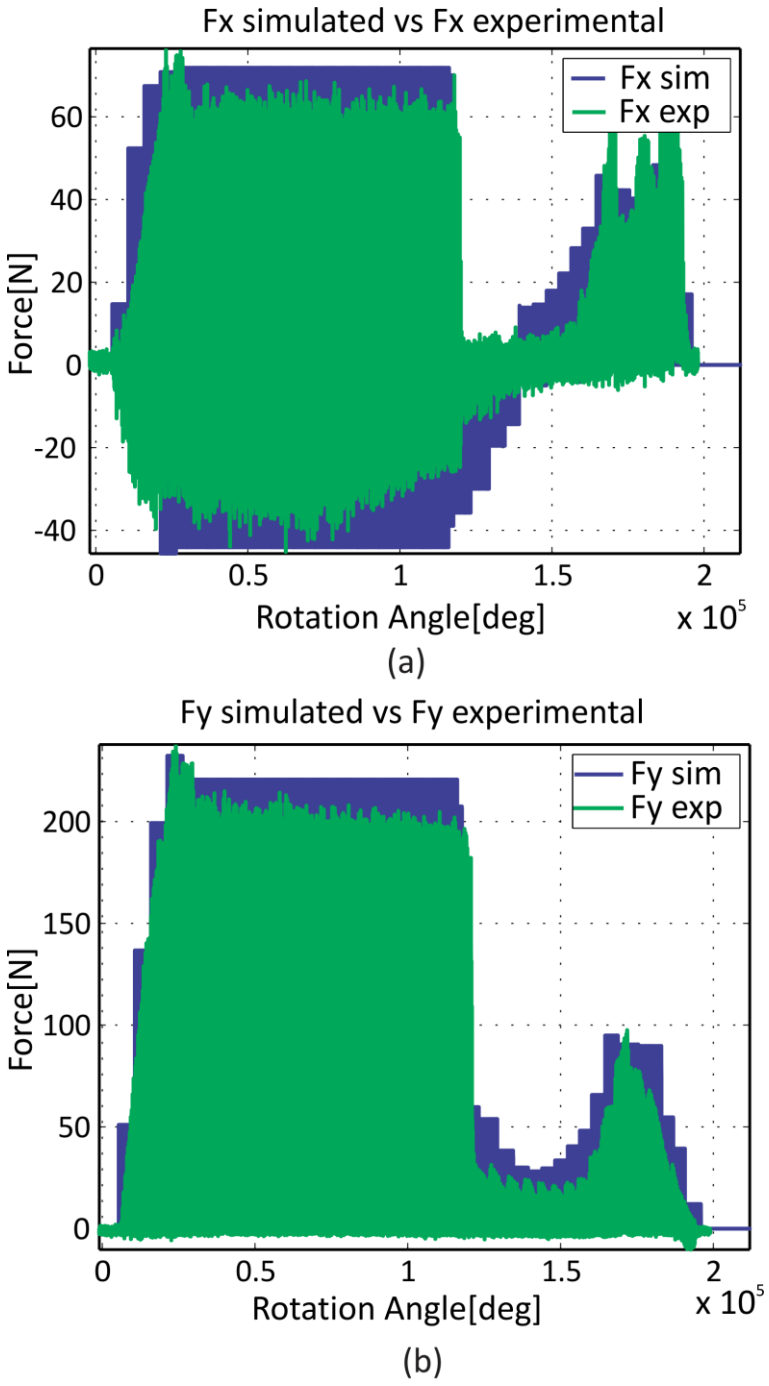

Figure 7.13: Penguin surface simulation and experimental cutting force comparison.

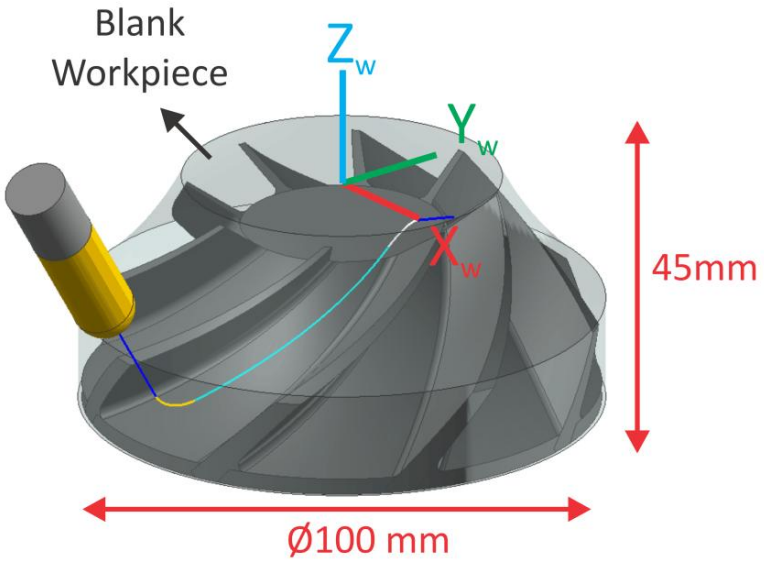

Figure 7.14: Simulated impeller roughing toolpath

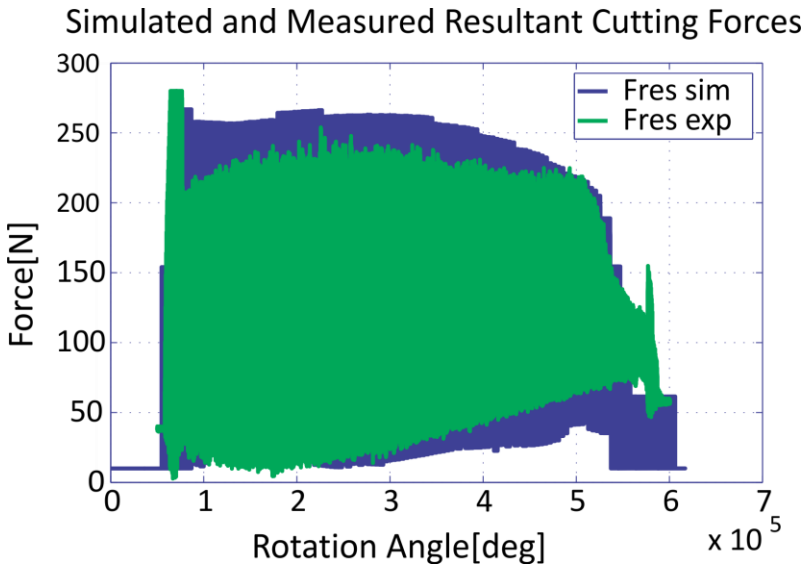

Figure 7.15: Impeller toolpath simulation and experimental resultant cutting force comparison

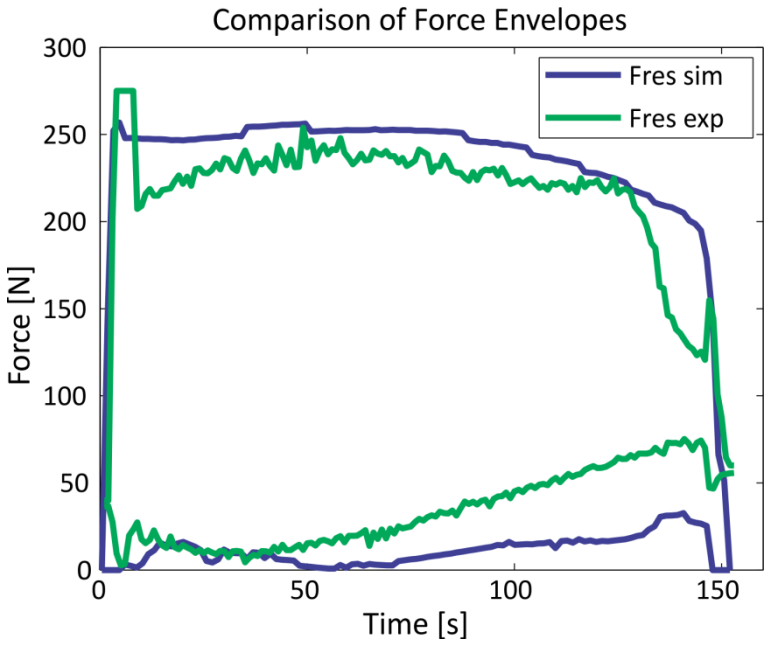

Figure 7.16: Comparison of force envelopes for impeller toolpath

Cutting parameters such as feedrate, spindle speed are selected to be the same as the first two validation tests. Sandvik two fluted ball-end mill with a diameter of 12 mm, nominal helix angle of 30°, and projection length of 37 mm is used as the cutting tool and Al7075 as workpiece material. Depths of cuts during the toolpath vary approximately between 0 – 5 mm along tool axis.

Figure 7.15 shows the comparison of the resultant cutting forces for simulated and measured cases. As it is demonstrated in Figure 7.15 simulated and experimental cutting forces match quite well. In general, the difference between simulation and the experimental force amplitudes is below 20 % which can be considered as acceptable for simultaneous 5-axis milling process simulations.

Figure 7.17: Experimental Impeller machining test

The discrepancy in cutting force predictions can be attributed to use of a table top dynamometer for this test. While machining the workpiece on the machine tool the workpiece has a contribution on the cutting forces due to its weight, furthermore this force component is not constant and change relative to rotation of the rotary axes of the machine tool. Experimental setup of impeller machining test is shown in Figure 7.17.

Another reason for the discrepancy in the cutting forces is due to induced cutting force component by the cutting torque. Workpiece length is adjusted to be approximately 150 mm in order to avoid the risk of collisions; therefore this induces the forces due to cutting torque.

7.3 Validation Tests in Rotating Coordinate Frame

For the validation of the cutting force model in rotating coordinate frame, an impeller roughing toolpath pass similar to path shown in Figure 7.14 is simulated and tested. Details of the toolpath are illustrated in Figure 7.18.

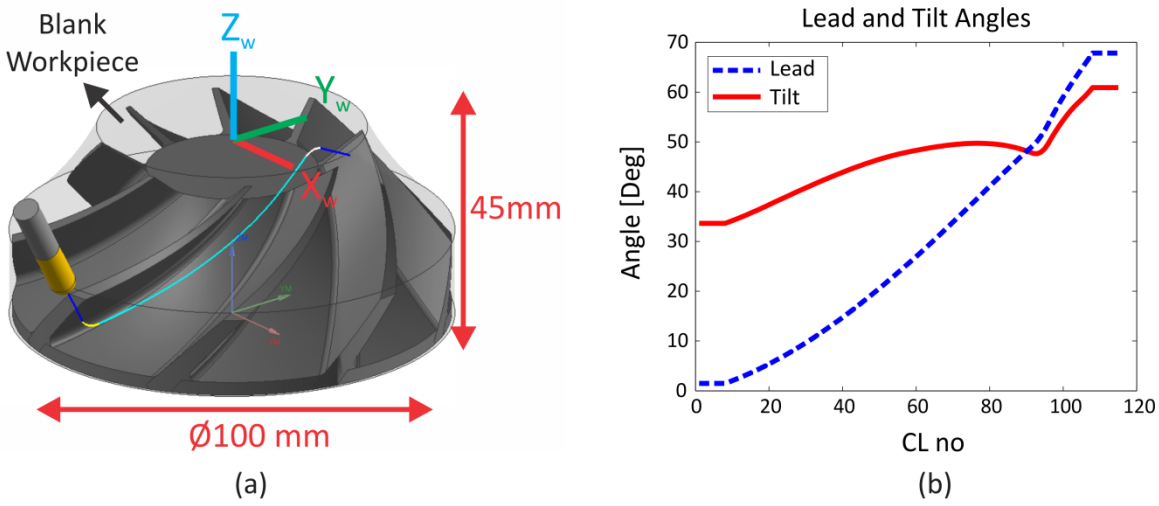

Figure 7.18: (a) Simulated impeller roughing toolpath, (b) Lead and tilt angles for one-pass of impeller toolpath

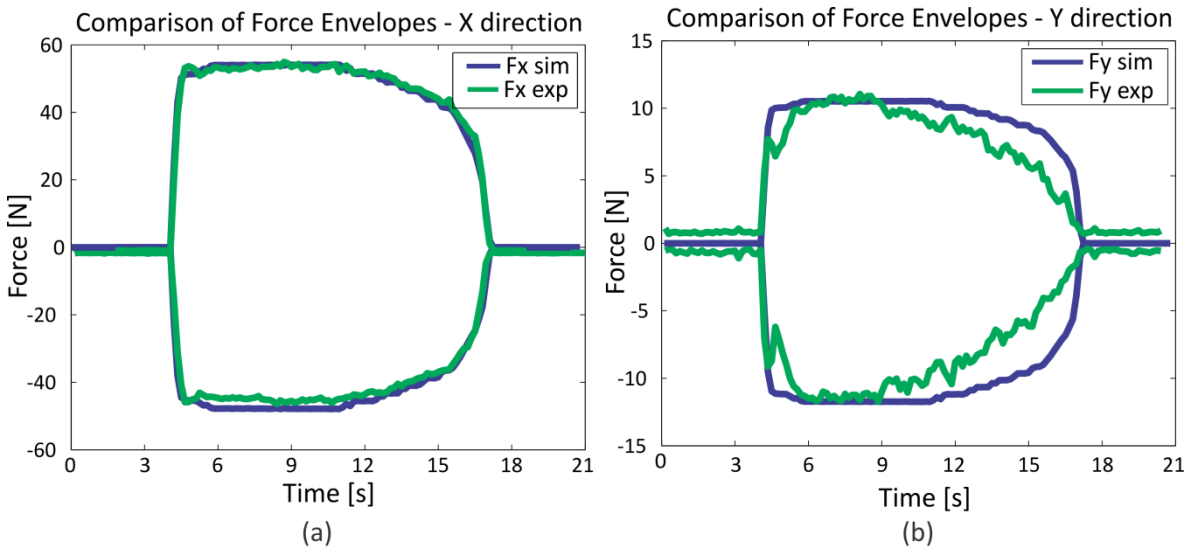

Figure 7.19: Comparison of cutting force envelopes, (a) X direction, (b) Y direction

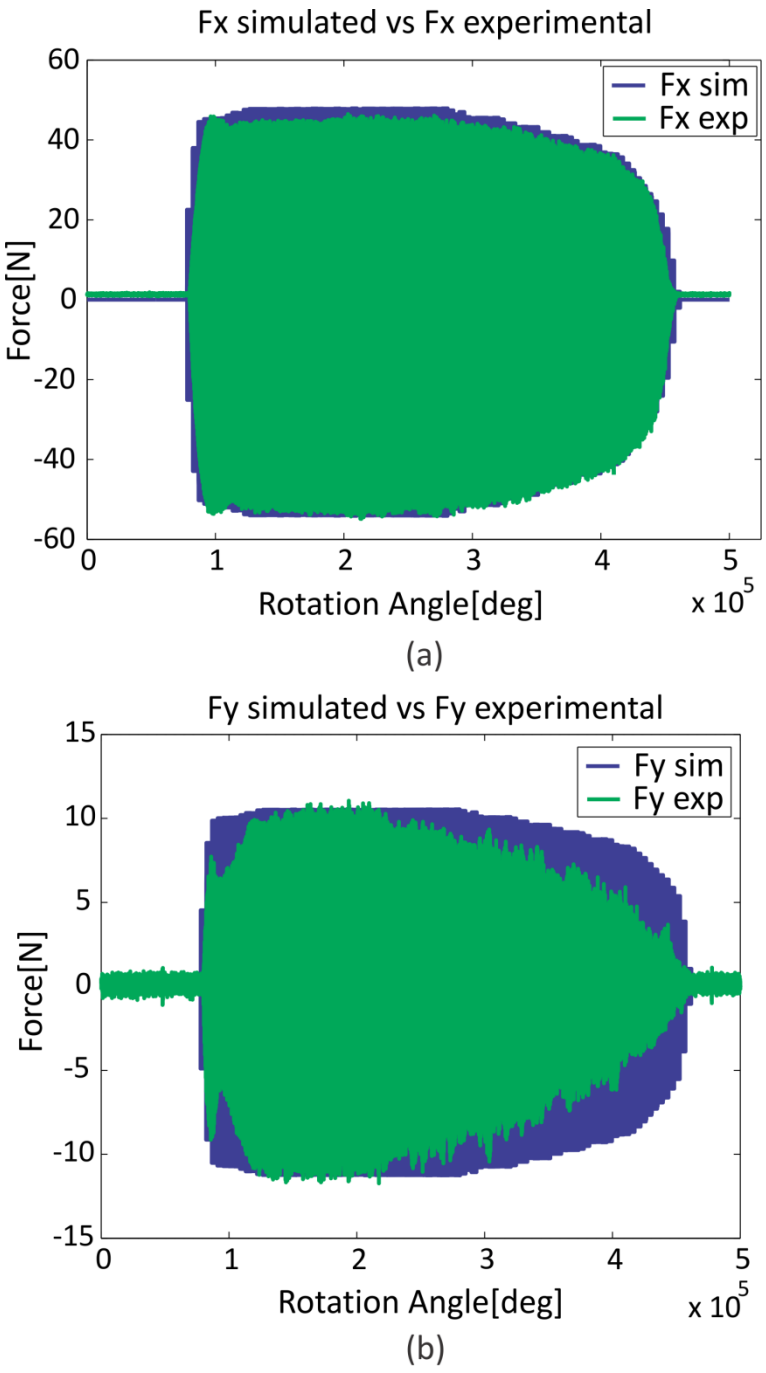

Figure 7.20: Predicted versus experimental data for the toolpath.

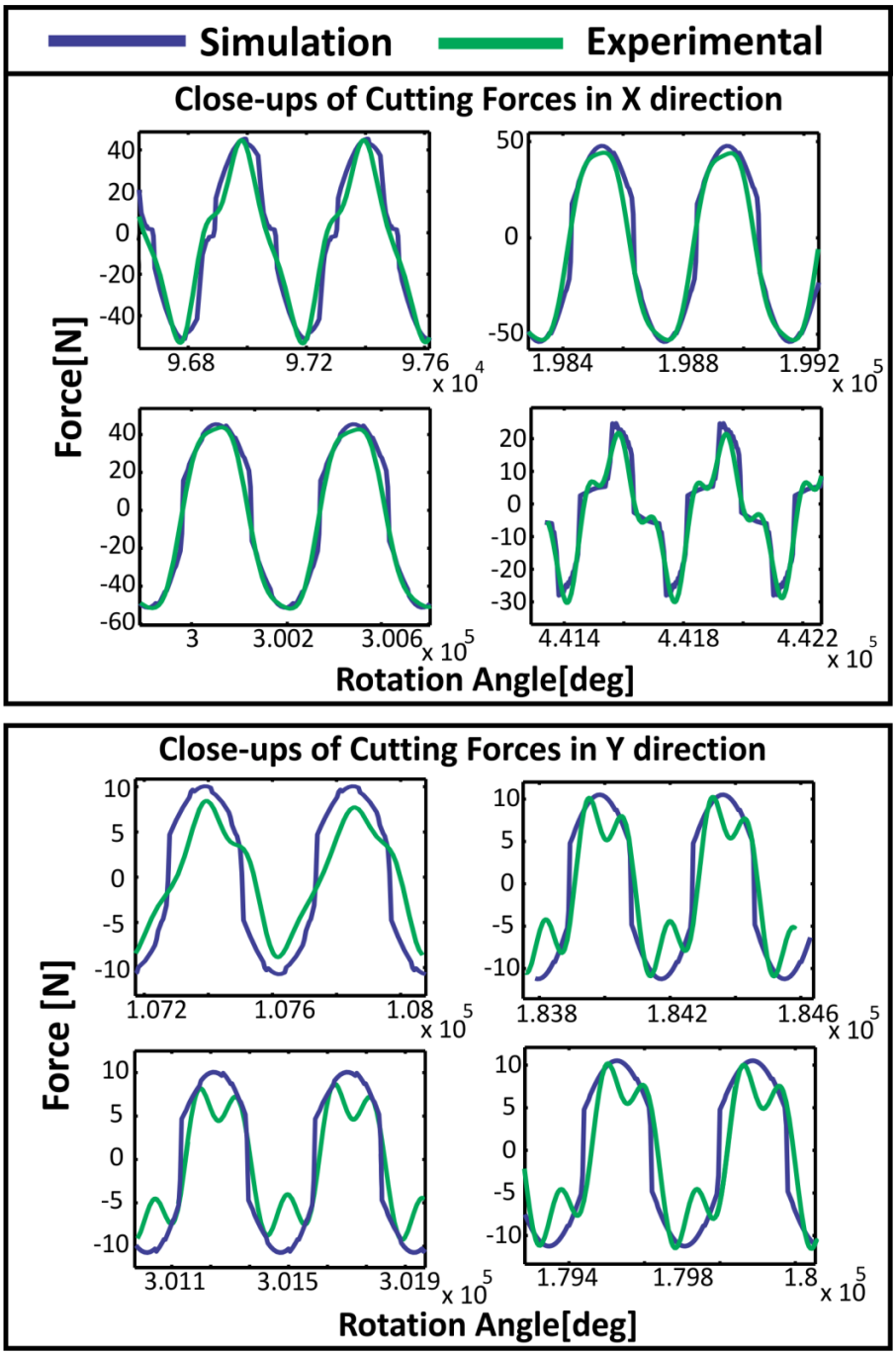

Figure 7.21: Close-ups of cutting forces for X and Y directions

In the test Al7075 workpiece material and a 6 mm diameter carbide cutting tool from Sandvik Plura series are used. Simulated toolpath is generated in NX6 CAM software. In the toolpath, impeller hub surface is used as the drive surface and the orientation of the tool axis is set to the normals of the drive surface (normal to drive). Consequently, a simultaneous 5-axis toolpath is obtained.

Spindle speed and the feedrate are selected as 5000 rpm and 250 mm/min respectively. Axial depth of cut varies approximately between 0-1.1 mm. Validation test is performed on Mori Seiki NMV5000 DCG machine tool using the Tool Center Point (TCP) control. In simultaneous 5-axis machining, movement of the translational axes and the rotary axes must be synchronized in order to keep the relative feedrate between the tool and the workpiece constant. Thus, TCP control (G43.4) makes the machining feedrate constant at the tool center point. In TCP control machining feedrate is specified as the constant, programmed feedrate and controller adjusts the feedrate automatically. For the simulated toolpath, in TCP control mode instantaneous feedrate change between 200-1250 mm/min. Conventional method for the constant feedrate implementation Inverse Time Feed (G93) function could also be used.

The results of the predicted cutting forces with the experimental data are shown from Figure 7.19 to Figure 7.21. From figures, it can be concluded that, predicted cutting forces in X direction match well with the experimental data. In Y direction, there are slight differences in the predicted cutting forces with the experimental data; however the agreement is still reasonably well.

Second validation test is performed for the full roughing toolpath of an impeller hub. Simulated toolpath is generated in NX7.5 CAM software using the Multi Blade Rough method. Generated toolpath consists of 1572 CL points employing zig-zag toolpath with lifts. Axial depth of cut varies approximately between 0-3 mm Details of the toolpath are shown in Figure 7.22

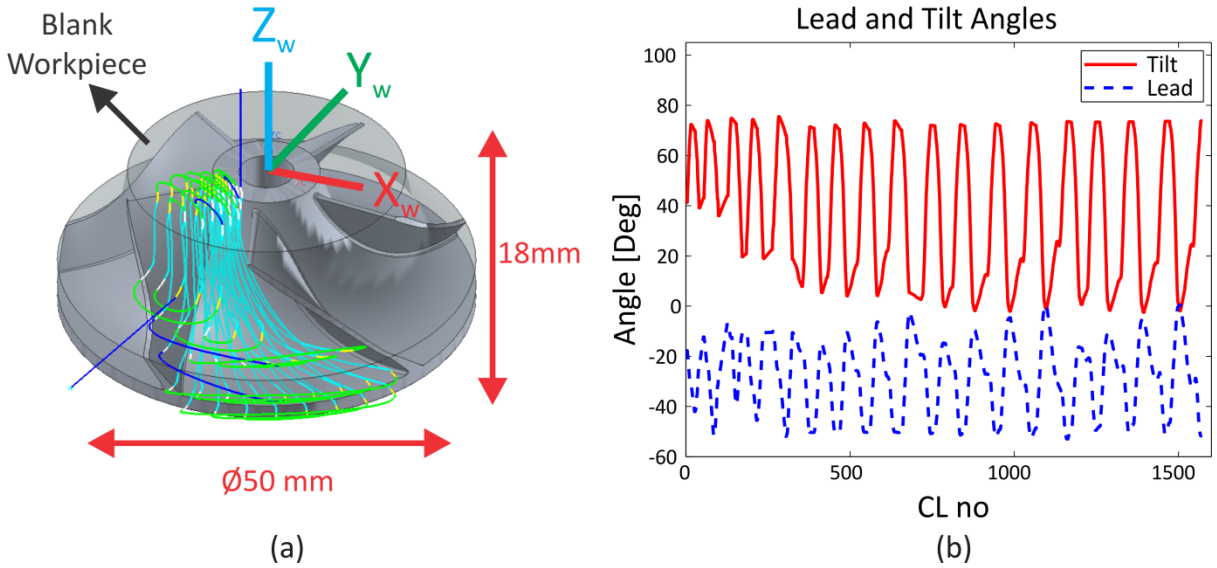

Figure 7.22: (a) Simulated Impeller Roughing (Hub Roughing) toolpath, (b) Lead and tilt angles for the toolpath

In the test Al7075 workpiece material and a 6 mm diameter carbide cutting tool are used. Spindle speed and the feedrate are selected as 5000 rpm and 500 mm/min respectively. Cutting tests are performed in TCP control mode and instantaneous feedrate changes approximately between 500 and 6600 mm/min. Forces are collected for every 4° during the machining operation. Output of the simulated machined workpiece and the experimental machined workpiece are shown in Figure 7.23 and Figure 7.24 respectively.

Cutter-Workpiece engagements are extracted using the three-orthogonal dexelfield engagement model. In the simulation disk height is set to 0.1 mm and the element spacing between individual depth buffers is set to 0.05 mm. Computation of the engagement result took 56 minutes and 25 seconds on a Windows 7 64-bit, Core2Duo 3.16 GHz / 8GB ram desktop PC.

Results of the validation tests are presented through Figure 7.25 to Figure 7.28. Figure 7.25 and Figure 7.26 shows the comparison of the cutting forces for full toolpath and

comparison of the cutting force close-ups are illustrated in Figure 7.27 and Figure 7.28. Close-ups are shown for 6 regions for better illustration of the simulated data with the measured data. According to the results of the validation tests, it can be stated that simulated and measured cutting forces match reasonably well although there are minor discrepancy in the predictions.

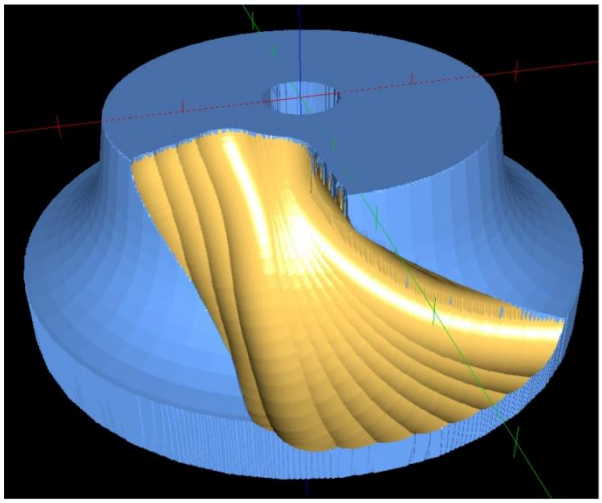

Figure 7.23: Simulated machined workpiece using three-orthogonal dexelfield engagement model

Figure 7.24: Experimental machined workpiece

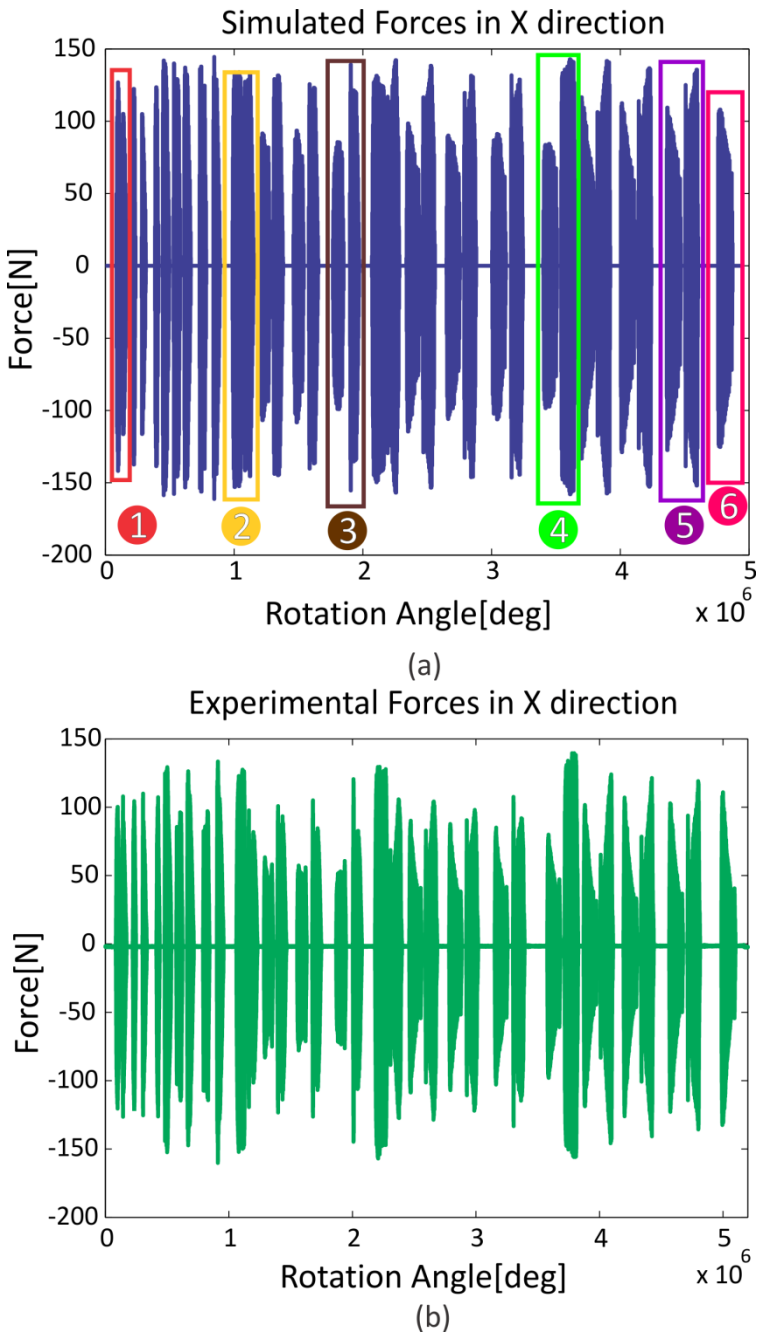

Figure 7.25 Comparison of simulated and experimental cutting forces for the impeller roughing toolpath in X direction

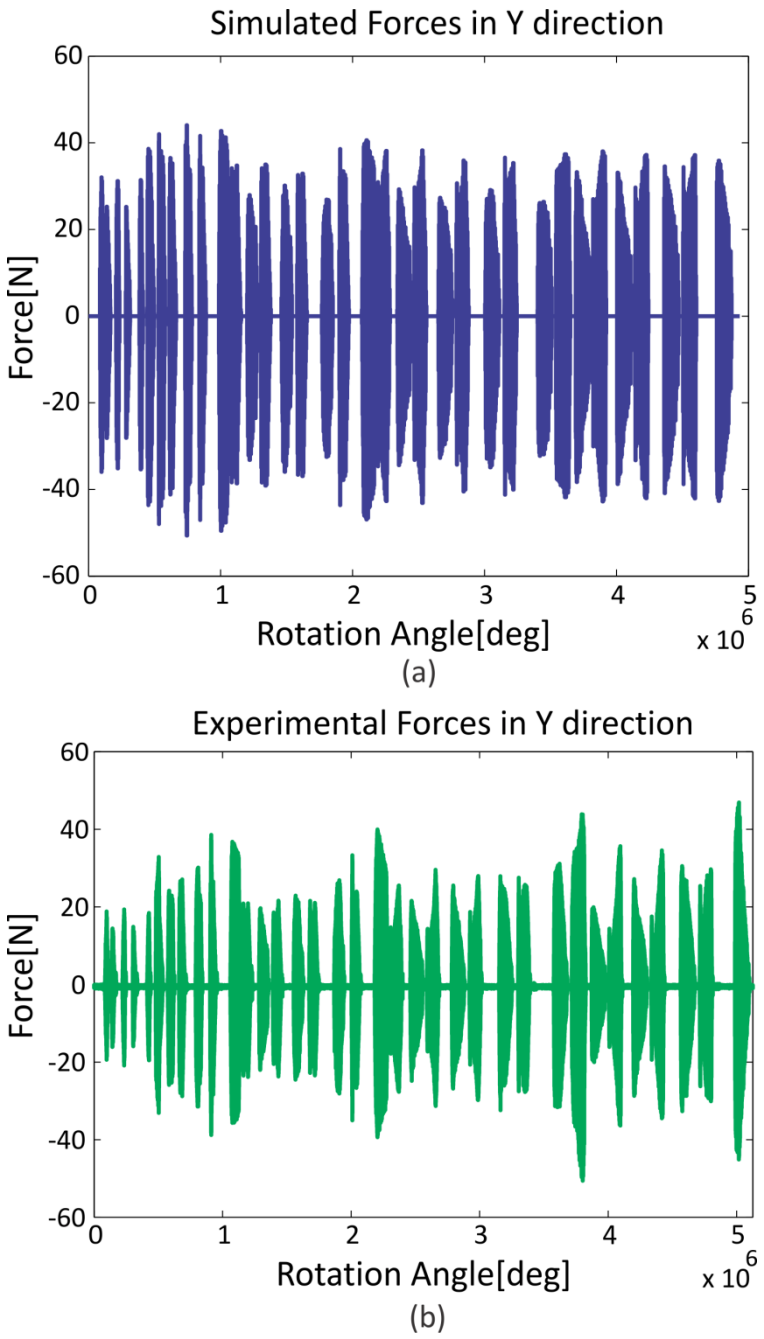

Figure 7.26: Comparison of simulated and experimental cutting forces for the impeller roughing toolpath in Y direction

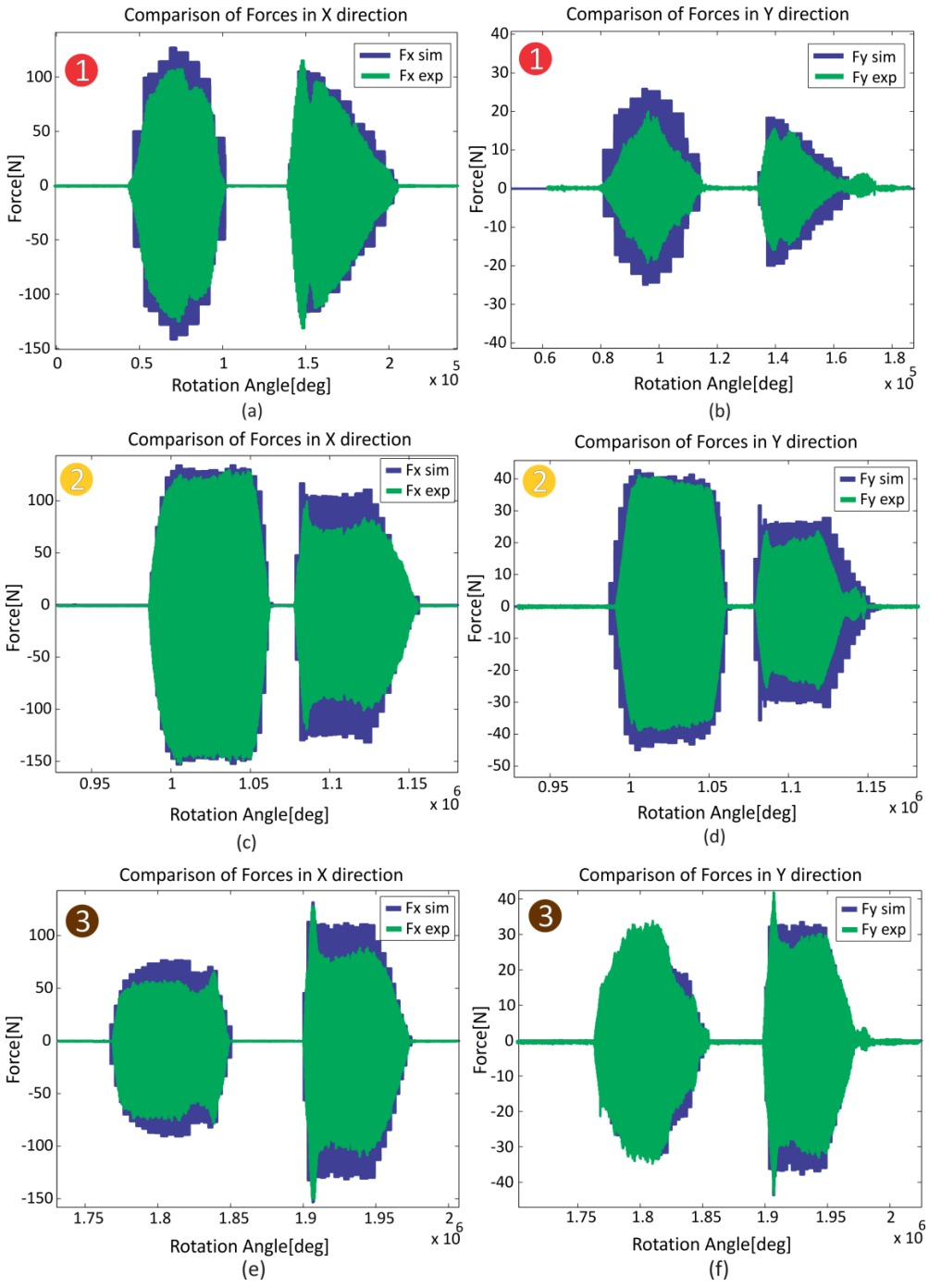

Figure 7.27: Comparison of cutting forces for regions 1-3

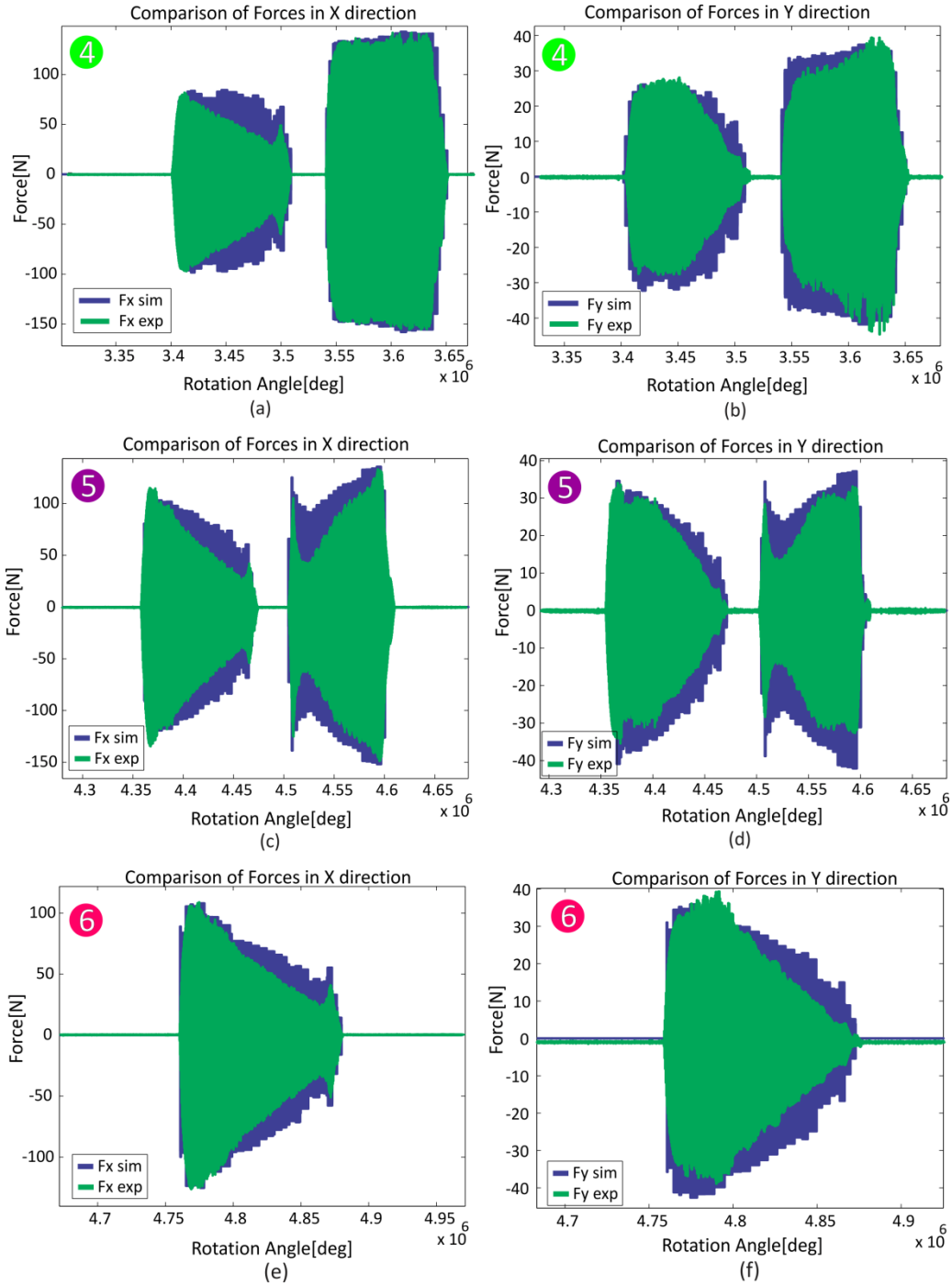

Figure 7.28: Comparison of cutting forces for regions 4-6

Trend of the predicted forces are in good agreement with the measured data. Discrepancy of the cutting forces is observed especially in the low axial immersion regions; however this is likely due to low resolution at smaller depth of cuts. The change in chip thickness is high due to the geometry of the ball-end cutter. Hence, increasing the simulation resolution from 100 microns to higher resolutions may increase the simulation accuracy which also causes an increase in the computation time. Another reason for the discrepancies may be attributed to high feedrates during the toolpath that exhibits an aggressive machining. This may also degrade the prediction accuracy since in high feedrates dynamic effects may alter the static forces and proposed model is a static force model.

Chapter 8

CONCLUSION

The primary goal of this research is the development of a cutting force prediction system based on mechanistic modeling technique for 5-axis free-form surface machining.

Cutting forces in machining is determined by extracting the Cutter-Workpiece Engagement (CWE) from the in-process workpiece in the form of start and exit angles as a function of axial height along the tool axis. A novel discrete method, called Three-Orthogonal Dexelfield, of obtaining CWE maps for 5-axis ball-end milling is developed. Three-orthogonal dexelfield uses the depth buffer in three orthogonal directions. In other words, three-orthogonal dexelfield approach utilizes Z-map, Y-map and X-map simultaneously for improved accuracy. As a result, computation time is relatively long compared to conventional Z-map method. The simulation results of the CWE model showed that developed model can extract the CWE maps accurately but it takes longer time for simulation than the solid-modeler based CWE method.

Mechanistic cutting coefficient calibration method is implemented for different cutting speeds, feedrates and tool geometry on Al7039 and Al7075 workpiece materials. Besides, cutting force calibration methodology in rotating coordinate frame is developed and implemented for the identification of cutting coefficients.

A mechanistic cutting force prediction model for 5-axis ball-end milling is developed. Cutting force modeling is performed in the fixed coordinate frame (for table type dynamometer) and in the rotating coordinate frame (rotating coordinate dynamometer). Several validation tests for complex free-form surfaces are presented in the study. These validation tests are performed on Al7039 and Al7075 workpiece materials with carbide

cutting tools. These validation tests demonstrate that presented model is computationally efficient and force predictions are in good agreement with the measured data.

Next generation CAM technologies such as force based feedrate scheduling and toolpath generation demand the use of variable feedrate implementation along the toolpath. For this reason, 5-axis machine tool kinematics is investigated and a generic post-processor with variable feedrate is developed. A virtual machine simulation model, which is capable of simulating machine tool movements from the NC code, is also presented.

As a future work, force based feedrate scheduling strategy for improving productivity for 5-axis ball-end milling of free-form surfaces may be developed. Thus, with this strategy cycle times can be reduced significantly.

BIBLIOGRAPHY

[1] Available: http://www.tectaero.com/products/strut-and-nacelle/

[2] Available: http://www.sciencemuseum.org.uk

[3] Available: http://www.starragheckert.com/sh

[4] Available: http://neutra.web.psi.ch/images/gallery/blade.jpg

[5] Available: https://www.bsl.unsw.edu.au/research.html

[6] Available: http://www.datrondynamics.com

[7] Available: http://www.kneereplacement.com/DePuy/DePuy_technology/DePuy_knees/

[8] Available: http://www.ulrichmedical.com/index.php5?346

[9] H. Erdim, "Improving Productivity in Free-form Surface Machining," Master's Thesis, Koç University, 2005.

[10] H. B. Voelcker and W. A. Hunt, "Role of Solid Modelling in Machining-Process Modelling and NC Verification " *SAE Preprints*, 1981.

[11] W. P. Wang, "Solid modeling for optimizing metal removal of three-dimensional NC end milling," *Journal of Manufacturing Systems*, vol. 7, pp. 57-65, 1988.

[12] R. B. Jerard, *et al.*, "Approximate methods for simulation and verification of numerically controlled machining programs," *The Visual Computer*, vol. 5, pp. 329-348, 1989.

[13] B. K. Fussell, *et al.*, "Modeling of cutting geometry and forces for 5-axis sculptured surface machining," *Computer-Aided Design*, vol. 35, pp. 333-346, 2003.

[14] S. K. Gupta, *et al.*, "Geometric algorithms for computing cutter engagement functions in 2.5D milling operations," *Computer-Aided Design*, vol. 37, pp. 1469-1480, 2005.

[15] B. Ozturk, "Chip Load, Calibration Analysis and Dynamics of Ball-End Milling for Free-form Surface Machining," Master's thesis, Koc University, 2005.

[16] Z. Yao, "Finding Cutter Engagement for Ball End Milling of Tessellated Free-Form Surfaces," *ASME Conference Proceedings*, vol. 2005, pp. 121-127, 2005.

[17] D. Jang, *et al.*, "Voxel-Based Virtual Multi-Axis Machining," *The International Journal of Advanced Manufacturing Technology*, vol. 16, pp. 709-713, 2000.

[18] E. Ozturk and E. Budak, "Modeling of 5-Axis Milling Processes," *Machining Science and Technology: An International Journal*, vol. 11, pp. 287-311, 2007.

[19] W. Wang and K. Wang, "Real-time verification of multiaxis NC programs with raster graphics," in *Robotics and Automation. Proceedings. 1986 IEEE International Conference on*, 1986, pp. 166-171.

[20] A. D. Spence and Y. Altintas, "A Solid Modeller Based Milling Process Simulation and Planning System," *Journal of Engineering for Industry*, vol. 116, pp. 61-69, 1994.

[21] A. D. Spence, *et al.*, "Integrated solid modeler based solutions for machining," presented at the Proceedings of the fifth ACM symposium on Solid modeling and applications, Ann Arbor, Michigan, United States, 1999.

[22] B. M. Imani, *et al.*, "An improved process simulation system for ball-end milling of sculptured surfaces," *International Journal of Machine Tools and Manufacture*, vol. 38, pp. 1089-1107, 1998.

[23] B. M. Imani and M. A. Elbestawi, "Geometric Simulation of Ball-End Milling Operations," *Journal of Manufacturing Science and Engineering*, vol. 123, pp. 177-184, 2001.

[24] W. Ferry and D. Yip-Hoi, "Cutter-Workpiece Engagement Calculations by Parallel Slicing for Five-Axis Flank Milling of Jet Engine Impellers," *Journal of Manufacturing Science and Engineering*, vol. 130, pp. 051011-12, 2008.

[25] I. T. Chappel, "The use of vectors to simulate material removed by numerically controlled milling," *Computer-Aided Design*, vol. 15, pp. 156-158, 1983.

[26] T. V. Hook, "Real-time shaded NC milling display," *SIGGRAPH Comput. Graph.*, vol. 20, pp. 15-20, 1986.

[27] R. Drysdale, *et al.*, "Discrete simulation of NC machining," *Algorithmica,* vol. 4, pp. 33-60, 1989.

[28] R. B. Jerard, *et al.*, "Methods for detecting errors in numerically controlled machining of sculptured surfaces," *Computer Graphics and Applications, IEEE,* vol. 9, pp. 26-39, 1989.

[29] B. K. Fussell, *et al.*, "Robust Feedrate Selection for 3-Axis NC Machining Using Discrete Models," *Journal of Manufacturing Science and Engineering,* vol. 123, pp. 214-224, 2001.

[30] D. Roth, *et al.*, "Mechanistic modelling of the milling process using an adaptive depth buffer," *Computer-Aided Design,* vol. 35, pp. 1287-1303, 2003.

[31] D. Roth, *et al.*, "Mechanistic modelling of the milling process using complex tool geometry," *The International Journal of Advanced Manufacturing Technology,* vol. 25, pp. 140-144, 2005.

[32] D. Roth, *et al.*, "Mechanistic modelling of 5-axis milling using an adaptive and local depth buffer," *Computer-Aided Design,* vol. 39, pp. 302-312, 2007.

[33] S. Takata, *et al.*, "A Cutting Simulation System for Machinability Evaluation Using a Workpiece Model," *CIRP Annals - Manufacturing Technology,* vol. 38, pp. 417-420, 1989.

[34] W. A. Kline, *et al.*, "The prediction of cutting forces in end milling with application to cornering cuts," *International Journal of Machine Tool Design and Research,* vol. 22, pp. 7-22, 1982.

[35] T. E. Bailey, *et al.*, "Integrated modeling for metal removal operations," in *Proceedings of the ASME Dynamic Systems and Control Division,* 1996, pp. 191-198.

[36] G. Yucesan and Y. Altintas, "Prediction of Ball End Milling Forces," *Journal of Engineering for Industry,* vol. 118, pp. 95-103, 1996.

[37] R. Zhu, *et al.*, "Mechanistic Modeling of the Ball End Milling Process for Multi-Axis Machining of Free-Form Surfaces," *Journal of Manufacturing Science and Engineering*, vol. 123, pp. 369-379, 2001.

[38] R. Zhu, "A Process Model-Based Monitoring and Fault Diagnosis Methodology for Free-Form Surface Machining Process," PhD Thesis, University of Illinois at Urbana-Champaign, 2001.

[39] T. Bailey, *et al.*, "Generic Simulation Approach for Multi-Axis Machining, Part 1: Modeling Methodology," *Journal of Manufacturing Science and Engineering*, vol. 124, pp. 624-633, 2002.

[40] T. Bailey, *et al.*, "Generic Simulation Approach for Multi-Axis Machining, Part 2: Model Calibration and Feed Rate Scheduling," *Journal of Manufacturing Science and Engineering*, vol. 124, pp. 634-642, 2002.

[41] C. E. Becze, *et al.*, "High-speed five-axis milling of hardened tool steel," *International Journal of Machine Tools and Manufacture*, vol. 40, pp. 869-885, 2000.

[42] L. Tunc and E. Budak, "Extraction of 5-axis milling conditions from CAM data for process simulation," *The International Journal of Advanced Manufacturing Technology*, vol. 43, pp. 538-550, 2009.

[43] W. B. Ferry and Y. Altintas, "Virtual Five-Axis Flank Milling of Jet Engine Impellers—Part I: Mechanics of Five-Axis Flank Milling," *Journal of Manufacturing Science & Engineering*, vol. 130, pp. 51-51, 2008.

[44] W. B. Ferry and Y. Altintas, "Virtual Five-Axis Flank Milling of Jet Engine Impellers Part II: Feed Rate Optimization of Five-Axis Flank Milling," *Journal of Manufacturing Science & Engineering*, vol. 130, pp. 131-1313, 2008.

[45] C.-H. She and Z.-T. Huang, "Postprocessor development of a five-axis machine tool with nutating head and table configuration," *The International Journal of Advanced Manufacturing Technology*, vol. 38, pp. 728-740, 2008.

[46] K. Sørby, "Inverse kinematics of five-axis machines near singular configurations," *International Journal of Machine Tools and Manufacture,* vol. 47, pp. 299-306, 2007.

[47] H. Erdim, *et al.*, "Feedrate scheduling strategies for free-form surfaces," *International Journal of Machine Tools and Manufacture,* vol. 46, pp. 747-757, 2006.

[48] G. M. Kim, *et al.*, "Cutting force prediction of sculptured surface ball-end milling using Z-map," *International Journal of Machine Tools and Manufacture,* vol. 40, pp. 277-291, 2000.

[49] Available: http://www.moduleworks.com/

[50] W. p. Wang and K. k. Wang, "Geometric Modeling for Swept Volume of Moving Solids," *IEEE Comput. Graph. Appl.,* vol. 6, pp. 8-17, 1986.

[51] S. Du, *et al.*, "Formulating swept profiles for five-axis tool motions," *International Journal of Machine Tools and Manufacture,* vol. 45, pp. 849-861, 2005.

[52] Y. Altintas, *Manufacturing Automation: Metal Cutting Mechanics, Machine Tool Vibrations, and CNC Design*: Cambridge University Press, 2000.

[53] Available: http://www.sandvik.coromant.com/

[54] S. D. Merdol and Y. Altintas, "Virtual Simulation and Optimization of Milling Operations---Part I: Process Simulation," *Journal of Manufacturing Science and Engineering,* vol. 130, pp. 051004-12, 2008.

[55] H. Erdim, *et al.*, "Free-Form Surface Machining and Comparing Feedrate Scheduling Strategies " *Machining Science and Technology: An International Journal,* vol. 11, pp. 117 - 133, 2007.

[56] J. J. J. Wang and S. Y. Liang, "Chip load kinematics in milling with radial cutter runout," *Journal of Engineering for Industry,* vol. 118, p. 111(6), 1996.

APPENDIX

Pseudocode for Cutting Force Model in Rotating Coordinate Frame

Inputs:

$Cutting\ conditions$: $w\ (spindle\ speed), f\ (feedrate)$

$Tool\ geometry$: $D\ (diameter), \beta\ (lag\ angle),$ $N_f\ (number\ of\ flutes)$

$Reference\ rotation\ angle$: Ω_R

$Angular\ Integration\ angle$: $d\theta$

$Axial\ Integration\ height$: dz

$Tool\ path\ CLSF\ file$: $CL\ (number\ of\ cutter\ location)$

Outputs:

$Cutting\ forces$: $Fx, Fy, Fz, Fres$

Variables:

$K = \frac{D}{2 \cdot z}$: $Number\ of\ axial\ integration\ steps$

$M = \frac{2\pi}{d\theta}$: $Number\ of\ angular\ integration\ steps$

For $j = 1{:}\,CL$: $Integrate\ along\ the\ toolpath$

For $i = 1{:}\,M$: $Integrate\ along\ rotation\ angle$

For $p = 1{:}\,N_f$: $Integrate\ along\ number\ of\ flutes$

For $k = 1{:}\,K$: $Integrate\ along\ axial\ height$

$\theta = \Omega + 2\pi(n-1)/N_f - \beta_k$: $Immersion\ angle\ for\ tooth\ p$

$z(k) = k \cdot dz$: $Axial\ position$

If $\theta_{st} < \theta < \theta_{ex}$: $\theta st{:}\ entry\ angle \quad \theta ex{:}\ exit\ angle$

$(t_c)_k = t_x \times \sin(\theta) \times \sin(\psi) \times \cos(\alpha) \pm t_x \times \cos(\psi) \times \sin(\alpha)$

: $Chip\ thickness\ (\alpha{:}\ inclination\ angle\ i^{th}\ for\ CL\ point)$

$dA_c = tc_k \cdot dz$: $Differential\ chip\ load$

$dF_r = K_{rc} \times dA_c + K_{re} \times dz$

$dF_\psi = K_{\psi c} \times dA_c + K_{\psi e} \times dz$: $Differential\ forces$

$dF_t = K_{tc} \times dA_c + K_{te} \times dz$

$$\begin{bmatrix} dF_X \\ dF_Y \\ dF_Z \end{bmatrix}_{\text{RCD}} = [B][A] \times \begin{bmatrix} dF_r \\ dF_\psi \\ dF_t \end{bmatrix}$$: $Differantial\ cutting\ forces$ $in\ Rotating\ Coordinate\ Frame$

Else If : $\theta < \theta_{st}\ or\ \theta_{ex} < \theta\ (No\ Engagement)$

$dF_r = dF_\psi = dF_t = 0$

$dFx = dFy = dFz = 0$

End $(Engagement\ condition)$

$Fx(i) = Fx(i) + dFx$

$Fy(i) = Fy(i) + dFy$: $Sum\ the\ cutting\ forces$

$Fz(i) = Fz(i) + dFz$

End $(Toolpath\ integration\ loop)$

End $(Rotation\ angle\ integration\ loop)$

End $(Flute\ integration\ loop)$

End $(Toolpath\ integration\ loop)$

VITA

Yaman Boz completed his high school in Akhisar Anatolian High School, Manisa, in 2004. He entered Istanbul Technical University Mechanical Engineering Department in 2004 and graduated with a bachelor of engineering degree in Mechanical Engineering in 2008. Upon receiving his Bachelor's degree, he started pursuing M.Sc. program in Mechanical Engineering at Koc University as a teaching/research assistant. Currently, his work has led to three international and one national conference papers on the modeling of kinematics and mechanics of 5-axis machining. For the completion of the program he has involved in a mechanical engineering thesis study with the title 'Modeling of Cutting Forces for 5-axis Ball-end Milling of Free-form Surfaces'.